

6.4 Synthesis of Hydrophilic Endohedral ^{133}Xe -fullerenol with High Yield

S. Watanabe^{*}, N. S. Ishioka^{*}, H. Shimomura^{**}, H. Muramatsu^{**} and T. Kume^{*}

Department of Ion-Beam-Applied Biology, JAERI^{*},
Faculty of Education, Shinshu University^{**}

1. Introduction

Endohedral radioisotopic-fullerenes, which encapsulate a radioisotope within a fullerene cage, have a possibility of being new radiopharmaceuticals. Cagle *et al.*⁽¹⁾ reported the method of synthesizing ^{166}Ho -fullerenol ($^{166}\text{Ho}@\text{C}_{82}(\text{OH})_x$) and found the concentration of the $^{166}\text{Ho}@\text{C}_{82}(\text{OH})_x$ into bone tissue as a result of animal experiments. Since ^{166}Ho emits a β -ray with the maximum energy of 1.8 MeV, it seems that $^{166}\text{Ho}@\text{C}_{82}(\text{OH})_x$ can be applied to the therapy of bone cancer.

We have recently reported a method of synthesizing endohedral ^{133}Xe -fullerenol ($^{133}\text{Xe}@\text{C}_{60}(\text{OH})_x$),⁽²⁾ which would be also applied to the therapy of bone cancer, because ^{133}Xe emits a β -ray with the maximum energy of 0.346 MeV. The $^{133}\text{Xe}@\text{C}_{60}(\text{OH})_x$ was synthesized by stirring the *o*-dichlorobenzene solution containing $^{133}\text{Xe}@\text{C}_{60}$, 14 M KOH solution and tetrabutylammonium hydroxide (TBAH, 40% in water) in a rotary evaporator for 12 h. However, the recovery of the $^{133}\text{Xe}@\text{C}_{60}(\text{OH})_x$ was only 2%. Since the recovery was very low for medical application, other methods with the yield more than ten times were desired. Therefore, a novel method with a sufficient yield was designed.

In the present paper, we describe the novel method of synthesizing $^{133}\text{Xe}@\text{C}_{60}(\text{OH})_x$ with a higher yield and the stability of that in 0.9 % NaCl solution.

2. Experimental

Fullerene targets for ion implantation were

made by vacuum evaporation of fullerene (C_{60}) on Ni foils. Implantation of ^{133}Xe ions into the targets was carried out with an isotope separator at an acceleration energy of 30 keV. After ion implantation, the fullerene on the target was dissolved in *o*-dichlorobenzene. The solution was filtered through a membrane filter with 0.2 μm pore size (Millipore, JGWP) to remove insoluble materials.

One milliliter of the filtrate of *o*-dichlorobenzene solution containing endohedral ^{133}Xe -fullerene ($^{133}\text{Xe}@\text{C}_{60}$) and C_{60} was shaken for 1 min with 50 μL of tetrabutylammonium hydroxide (TBAH, 40% in water) and 1 mL of 14 M KOH solution in a polypropylene centrifuge tube of 2 mL capacity. On this shaking, $^{133}\text{Xe}@\text{C}_{60}(\text{OH})_x$ and $\text{C}_{60}(\text{OH})_x$ formed in *o*-dichlorobenzene phase. After the shaking, *o*-dichlorobenzene phase was collected in a new polypropylene centrifuge tube by a micropipette, and pure water was added to the *o*-dichlorobenzene phase. The mixture was shaken for 1 min to extract $^{133}\text{Xe}@\text{C}_{60}(\text{OH})_x$ and $\text{C}_{60}(\text{OH})_x$ into pure water phase.

The ^{133}Xe radioactivity of $^{133}\text{Xe}@\text{C}_{60}(\text{OH})_x$ and ultraviolet-visible absorption of $\text{C}_{60}(\text{OH})_x$ in the pure water phase were measured by γ -ray spectrometry and ultraviolet-visible spectroscopy, respectively, to determine the recovery defined as a percentage of the amount of $^{133}\text{Xe}@\text{C}_{60}(\text{OH})_x$ to that of original $^{133}\text{Xe}@\text{C}_{60}$ or as a percentage of the amount of $\text{C}_{60}(\text{OH})$ to that of original C_{60} .

The stability of the $^{133}\text{Xe}@\text{C}_{60}(\text{OH})_x$ in

0.9 % NaCl solution was examined to evaluate the stability in a human body for medical application. The 0.9 % NaCl solution containing $^{133}\text{Xe}@C_{60}(\text{OH})_x$ was allowed to stand at room temperature for 5 days. The ^{133}Xe radioactivity in the 0.9 % NaCl solution was measured by γ -ray spectrometry once a day until 5 days.

3. Results and Discussion

The recovery of the $^{133}\text{Xe}@C_{60}(\text{OH})_x$ synthesized by using the method described in this study was 40%, which was 20 times as large as that by using the previous method. The recovery of the $C_{60}(\text{OH})_x$ was also about 40%. Therefore, the chemical behavior of $C_{60}(\text{OH})_x$ seems to be similar to that of $^{133}\text{Xe}@C_{60}(\text{OH})_x$. The leaving time dependence of the relative intensity of the $^{133}\text{Xe}@C_{60}(\text{OH})_x$ in 0.9 % NaCl solution at room temperature is shown in Fig. 1. For the results of the stability in 0.9 % NaCl solution, the $^{133}\text{Xe}@C_{60}(\text{OH})_x$ was found to be sufficiently stable for 5 days.

The stability of $^{133}\text{Xe}@C_{60}(\text{OH})_x$ revealed that the endohedral radioisotopic -fullerenol

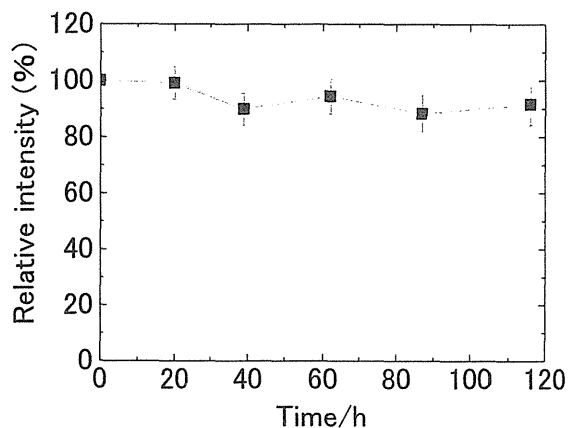


Fig.1. The leaving time dependence of the stability of $^{133}\text{Xe}@C_{60}(\text{OH})_x$ in 0.9 % NaCl solution.

would favorably be radiopharmaceuticals to be used for cancer therapy in nuclear medicine.

References

- 1) D. W. Cagle, S. J. Kennel, S. Mirzadeh, J. M. Alford, L. J. Wilson, *Proc. Natl. Acad. Sci.*, **96** (1999) 5182.
- 2) S. Watanabe N. S. Ishioka, H. Shimomura, H. Muramatsu, T. Kume, TIARA Annual Report 2002, JAERI-Review 2003 (2003) 262.

This is a blank page.

7. Microbeam Application

7.1	Test Operation of Focusing High-energy Heavy Ion Microbeam System	253
	T. Satoh, M. Oikawa, T. Sakai, M. Fukuda, S. Okumura, S. Kurashima, N. Miyawaki and T. Kamiya	
7.2	Micro-PIXE Technique for the Study of Asian Dust Sources	256
	M. Kasahara, C.-J. Ma, M. Okumura, T. Kojima, T. Hakoda, M. Taguchi, T. Sakai and Y. Ohara	
7.3	Research Activities using Micro-PIXE on the Study of Elements Accumulation by Microorganisms in The Fiscal Year 2003	259
	T. Ohnuki, F. Sakamoto, N. Kozai, T. Sakai, M. Oikawa and T. Satoh	
7.4	Detection of a Single Ion using the Luminescence from $\text{CaF}_2(\text{Eu})$ and $\text{ZnS}(\text{Ag})$	261
	T. Ohshima, T. Satoh, M. Oikawa and T. Kamiya	
7.5	Multiple X-Ray Detectors for High Efficiency Micro-PIXE Analysis	264
	T. Sakai, M. Oikawa, T. Satoh and S. Nomiya	
7.6	Fluorine Distribution around the Sound and Carious Fissures of Human Teeth	267
	H. Yamamoto, M. Nomachi, K. Yasuda, T. Sakai, Y. Iwami, S. Ebisu, Y. Sugaya, M. Oikawa, T. Satoh and M. Fukuda	
7.7	Modulation of Tissue Samples for Measurement of Cadmium using In-air Micro-PIXE	270
	T. Nagamine, K. Suzuki, K. Nakazato, H.D. Moon, T. Satoh, M. Oikawa, T. Sakai and K. Arakawa	
7.8	Fundamental Research of Grazing-exit PIXE	272
	K. Tsuji, T. Sakai and S. Yamamoto	
7.9	Analysis of Intracellular Distribution of Boron and Gadolinium in 9L Sarcoma Cells using a Single-ended Accelerator (Micro-PIXE)	274
	K. Endo, Y. Shibata, H. Yoshida, K. Nakai, T. Yamamoto, A. Matsumura, K. Ishii, K. Mizuma, T. Sakai, T. Satoh, M. Oikawa, K. Arakawa, H. Kumada and K. Yamamoto	
7.10	A Second Devise for the Target Preparation of the Micro-PIXE Camera for the Floating Cells	276
	S. Harada, S. Ehara, K. Ishii, S. Matsuyama, H. Yamazaki, S. Obara, T. Sakai, T. Satoh, M. Oikawa, K. Mizuma, K. Hotta, T. Izukawa and S. Anbe	
7.11	Development of Standard Reference Material for PIXE Analysis	278
	Y. Iwata, K. Ishizawa, T. Sakai, T. Satoh and M. Oikawa	

- 7.12 The Elemental Analysis of IGE-sensitized RBL-2H3 Cells using in Air Micro-PIXE ... 280
K. Mizuma, K. Ishii, Y. Barbotteau, S. Abe, H. Yamazaki, S. Matsuyama, E. Sakurai,
K. Yanai, T. Kamiya, T. Sakai, T. Satoh, M. Oikawa and K. Arakawa
- 7.13 Imaging of Biological Samples using Proton-induced Characteristic X-ray Emission ... 283
Y. Oguri, S. Iwatani, J. Kaneko, J. Hasegawa, H. Fukuda, M. Ogawa, Y. Saitoh
and T. Sakai

7.1 Test Operation of Focusing High-energy Heavy Ion Microbeam System

T. Satoh*, M. Oikawa*, T. Sakai*, M. Fukuda*, S. Okumura*, S. Kurashima*,
N. Miyawaki* and T. Kamiya**

Advanced Radiation Technology Center, JAERI*

Department of Material development, JAERI**

1. Introduction

A focused high-energy heavy ion scanning microbeam system with a special resolution of about $1\mu\text{m}$ is being developed at the AVF cyclotron of the TIARA facility. It will provide microbeams to applications in biomedical science such as radio microsurgery and mutagenesis with single ion hit technique which will permit single cell irradiation in the atmosphere. The details of the system design are described in Ref. 1. The major devices of the system listed following are installed on the vertical beam line of HX in 2002:

- micro slits to define the micron-sized object of the beams;
- divergence defining slits;
- an X-Y scanner to scan and position the beams two-dimensionally;
- a quadruplet quadrupole magnet to focus the beams to $1\mu\text{m}$.

The spread of the beam energy $\Delta E/E$ less than 10^{-4} (generally the energy spread of cyclotron beams is larger than 10^{-3}) is necessary in order to reduce the contribution of chromatic aberration to the beam spot size. Therefore, the flat top acceleration technique²⁾ was introduced to reduce the energy spread of the cyclotron beams and was used in the test operations reported here.

2. Measurement of Microbeam Diameter

Figure 1 shows the close-up view of the target point. A $\text{CaF}_2(\text{Eu})$ scintillator of 1mm in thickness was set at the target point to observe the size and the shape of the beams. The scintillation was magnified by a long distance microscope, enhanced by an image intensifier and detected by a CCD camera. We carried out beam focusing tests with 260 MeV $^{20}\text{Ne}^{7+}$ beams. A sample of the observed scintillation image is shown in fig. 2 and its diameter was

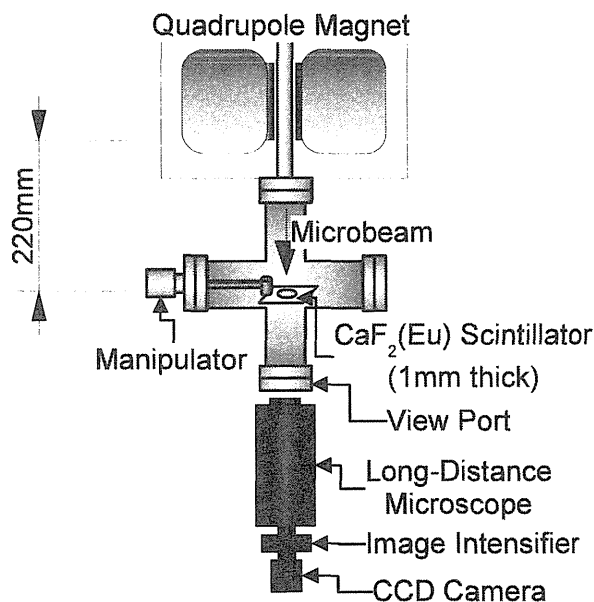


Fig. 1 Close-up view of the target point of the focused high-energy heavy ion scanning microbeam system.

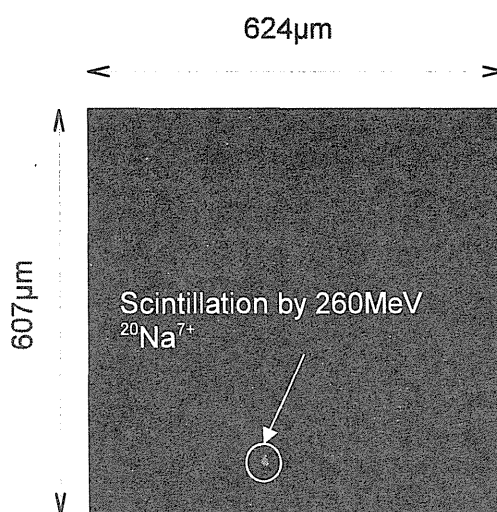


Fig. 2 Scintillation observed with a CCD camera.

about 30 μm . The actual beam diameter is smaller since the scintillation broadened in the scintillator.

3. Acquisition of a Mesh Image

A titanium mesh with $\phi 110\ \mu\text{m}$ holes spaced at 200 μm , a $\text{CaF}_2(\text{Eu})$ scintillator and a photo multiplier (PMT) shown in fig. 3 were set at the end of the manipulator. The beams were scanned by the X-Y scanner and scintillation induced by beams passing through the holes were detected. Values of the scanning coil currents were used as beam position data because displacement of the beams is proportional to the currents. The system of beam scanning control and measurement is schematically described in fig. 4. The mesh pattern is clearly seen in an example of

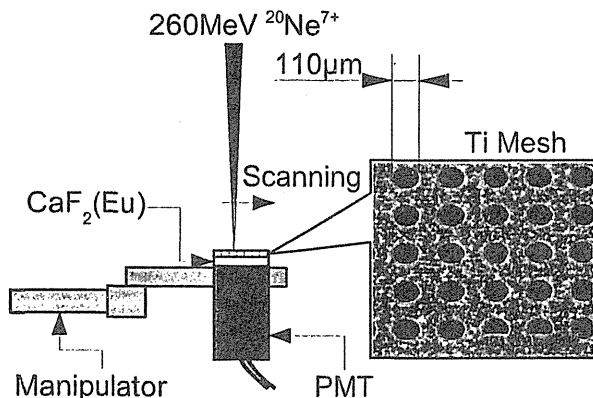


Fig. 3 Ti mesh, $\text{CaF}_2(\text{Eu})$ scintillator and photo multiplier (PMT).

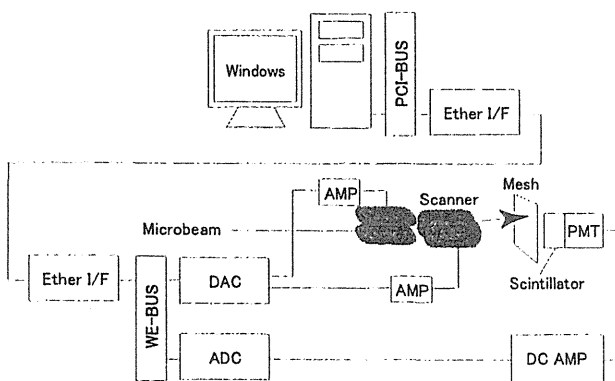


Fig. 4 Scanning control and measurement system.

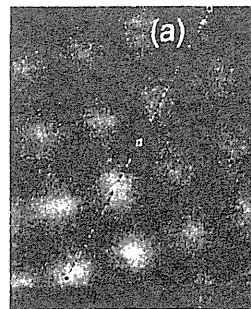


Fig. 5 Scintillation intensity image of a Ti mesh obtained by using a scanned microbeam.

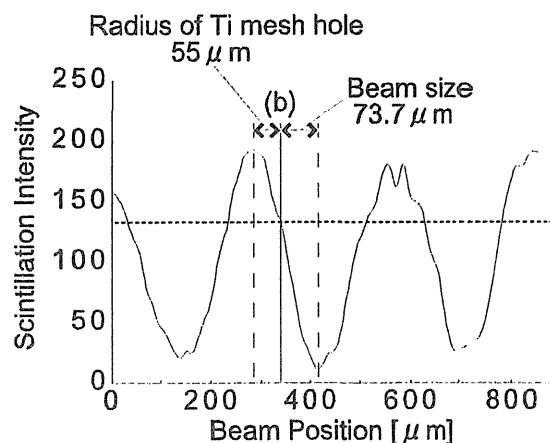


Fig. 6 Scintillation intensity along the line (a) in fig. 5.

scintillation intensity image in fig. 5. Intensity distribution along the line indicated in the figure is graphed in Fig. 6. The beam spot size was estimated from the intensity distribution and is about 70 μm , which is two times as large as that obtained from the CCD image.

4. Summary

The test formation of microbeam of 260 MeV $^{20}\text{Ne}^{7+}$ was carried out with the focused high-energy heavy ion microbeam system. The beam diameter measured on the scintillation image taken with the CCD camera was less than 30 μm . However, that estimated from the mesh pattern measured by use of the X-Y scanner was about 70 μm . The cause of this disagreement may be in the scanning system, which we will verify in the following year.

After completion of the system development,

a vacuum window of a thin titanium film will be installed at 3 mm upstream the target point to extract the beams into the atmosphere. The scanning control and measurement system will be built in the single-ion hit system.

References

- 1) M. Oikawa, T. Kamiya, M. Fukuda, S. Okumura, H. Inoue, S. Masuno, S. Umemiya, Y. Oshiyama and Y. Taira, Nucl. Instr. and Meth., B210 (2003) 54.
- 2) M. Fukuda, S. Kurashima, N. Miyawaki, S. Okumura, T. Kamiya, M. Oikawa, Y. Nakamura, T. Nara, T. Agematsu, I. Ishibori, K. Yoshida, W. Yokota, K. Arakawa, Y. Kumata, Y. Fukumoto, K. Saito, Nucl. Instr. and Meth., B210 (2003) 33.

7.2 Micro-PIXE Technique for the Study of Asian Dust Sources

M. Kasahara^{*}, C.-J. Ma^{*}, M. Okumura^{*}, T. Kojima^{**}, T. Hakoda^{**},
M. Taguchi^{**}, T. Sakai^{***} and Y. Ohara^{***}

Graduate School of Energy Science, Kyoto University^{*}

Department of Material Development, JAERI^{**}

Advanced Radiation Technology Center, JAERI^{***}

1. Introduction

The Asian dust storm is a well-known springtime meteorological phenomenon throughout East Asia as well as Pacific Ocean. A large number of studies on the Asian dust particles have been reported¹⁻³⁾. It is presumed that Asian dust particles can be altered by several aging processes such as absorption and oxidation during their long-range transport. There remains the need to more fully understand how man-made pollutants and sea-salt aerosol are incorporated into natural Asian dust storm particles¹⁾. In order to understand these variations of Asian dust storm particles, it is desirable to investigate the nature of original sands collected at source areas in China. However, unfortunately, the thorough study including the analysis of individual sands of various source regions, which can provide detailed information about the nature and composition of Asian dust sources, was not reported.

The primary goal of this study is to report the comparative characteristics of bulk sands collected at four different desert regions in China. In addition, chemical composition and its visual distribution on individual sands were newly determined.

2. Experimental procedure

In order to obtain more detailed information such as chemical structure and mixing state of surface and inner individual sands, micro-particle induced x-ray emission (PIXE) analytical measurement was performed with the

facilities of the Takasaki ion accelerators for advanced radiation application, Japan. Micro-PIXE measurement was performed with a scanning 2.6 MeV H⁺ micro beam accelerated by 3 MV single-ended accelerator. Beam diameter and beam current were 1-2 μm and more than 100 pA, respectively. The more detailed analytical procedures and experimental set-up of PIXE and micro-PIXE were described elsewhere³⁾. In addition, four kinds of bulk original ground-sands in desert areas of China were analyzed by PIXE. Also the water-soluble fraction extracted from the surface of sand was determined using PIXE. PIXE analysis was performed with a proton beam of 6 mm diameter and 2.0 MeV energy from a Tandem Cockcroft accelerator. Beam intensities from 10 to 60 nA were employed and the total dose was about 20 μC .

3. Results and Discussion

Fig. 1 represents the PIXE spectra of bulk sands at four desert regions in China and an example of micro-PIXE spectrum for a single sand collected at Yinchuan desert region. From the PIXE analysis we calculated the elemental mass concentrations of bulk and water-soluble fraction of each sand collected at four different desert regions in China. Unfortunately, Al could not be quantified by our PIXE method. As expected Si and other crustal elements showed overwhelmingly high mass concentration. From four kinds of samples, 20-30 individual sands were randomly selected for single sand analysis using micro-PIXE. Fig. 2 shows the example of

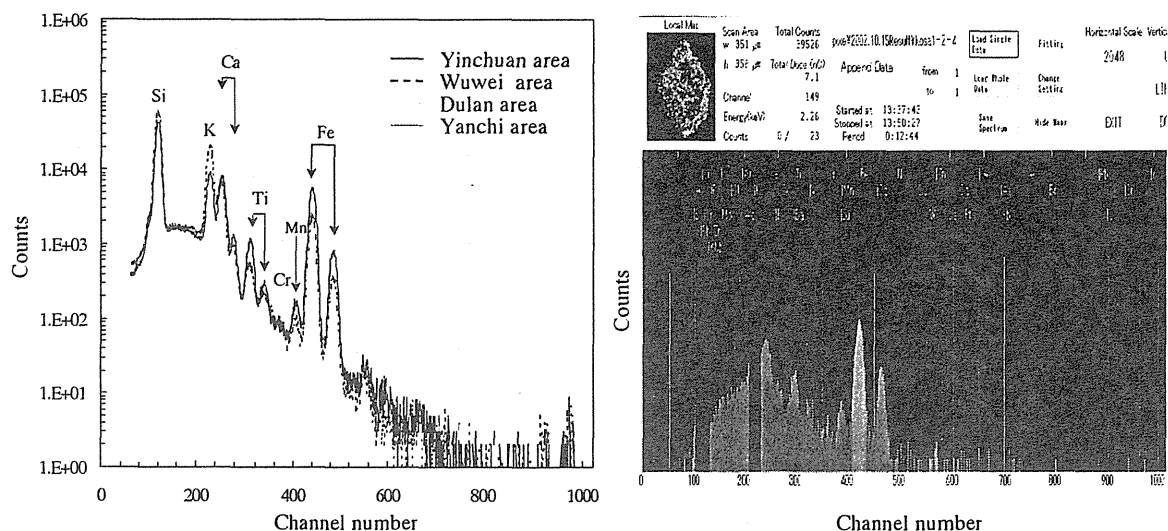


Fig. 1 PIXE spectra of bulk sands in four different deserts (lef t) and the example of micro -PIXE spectrum for a single sand collected in Yinchuan desert area in China (ri ght).

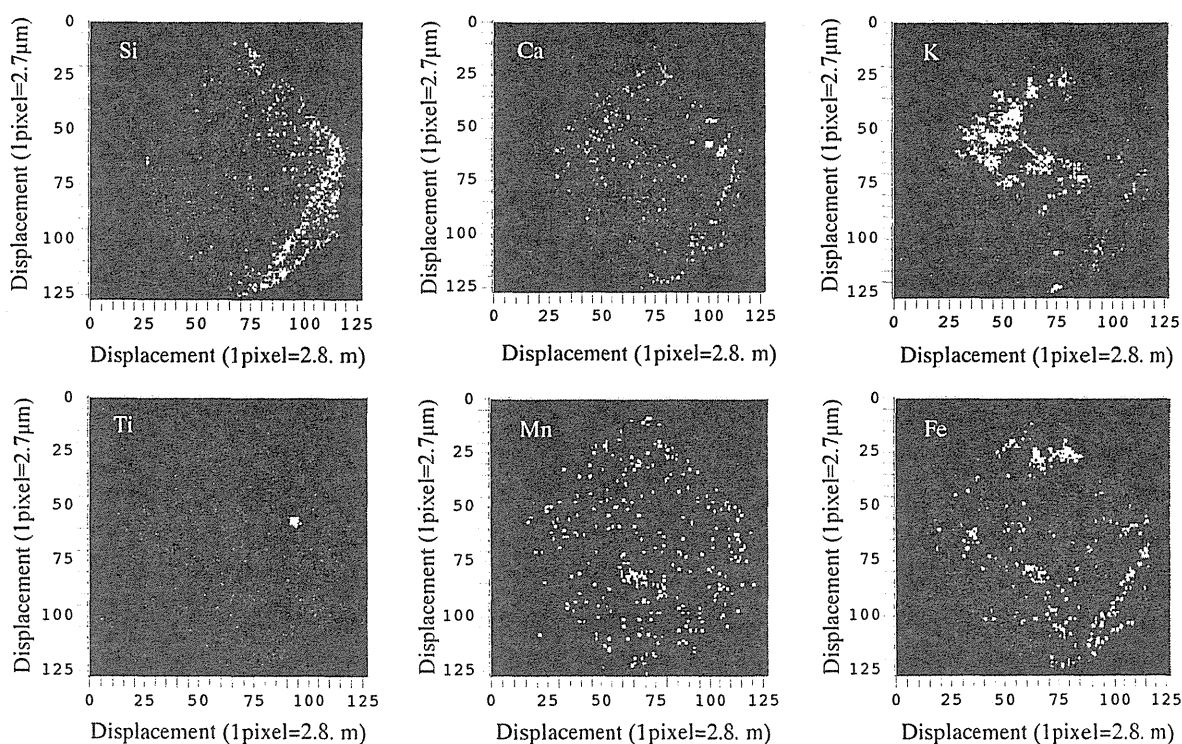


Fig. 2 The example of the micro -PIXE elemental maps taken on a single sand collected in Yinchuan desert area in China. Full scan size is 351 $\mu\text{m} \times 356 \mu\text{m}$ and the total accumulated charge is 7.1 nC.

micro-PIXE elemental maps taken on a single sand collected in Yinchuan area. As shown in Fig. 2, by means of this micro-PIXE it was possible to draw the distribution of components in and/or on individual sands. Sands were

generally sharp/round-edged irregular shape and mainly contained crustal components.

Fig. 3 illustrates the size distribution of original sands collected at four desert areas in China. The size of individual sands was

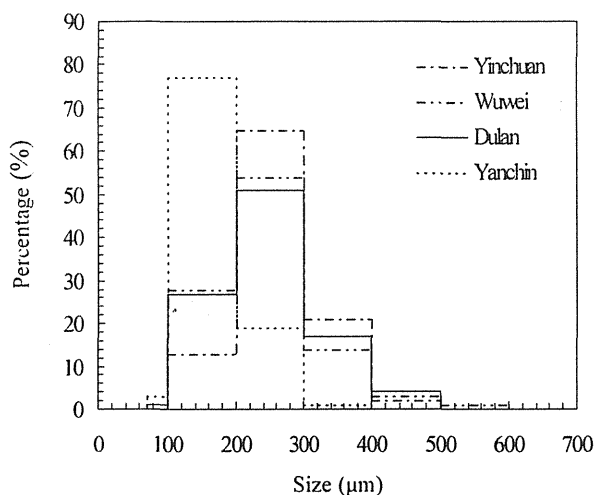


Fig. 3 Relative size distribution of original sands collected at four desert areas in China.

calculated with the mean of apse line and minor line of each sand by using digital microscope (KEYENCE, VH-7000). For each sample, 500 sands were randomly selected for their sizing. The shape of size distribution is monomodal showing the maximum level between 200 μm and 300 μm for sands collected at Yinchuan, Wuwei, and Dulan sites. Whereas, the maximum level for Yanchin desert sands is displayed between 100 μm and 200 μm. The size of sands at Wuwei desert area is relatively wide spread in the range up to 600 μm. The size of original sands collected at Yanchin desert site is relatively smaller than those collected at other three sites.

Fig. 4 shows pH of the extracted water from four kinds original desert sands. pH of water soluble fraction in every desert sands shows slightly basic. Also a little bit different pH level was measured among desert area (pH 7.2 at Yinchuan, pH 7.2 at Wuwei, pH 7.3 at Dulan, and pH 7.2 at Yanchin). It can be suggested that pH of water soluble fraction in desert sands is influenced by initial composition of dust sands such as Ca^{2+} and CO_3^{2-} .

4. Summary

As the source of Asian dust particles, the

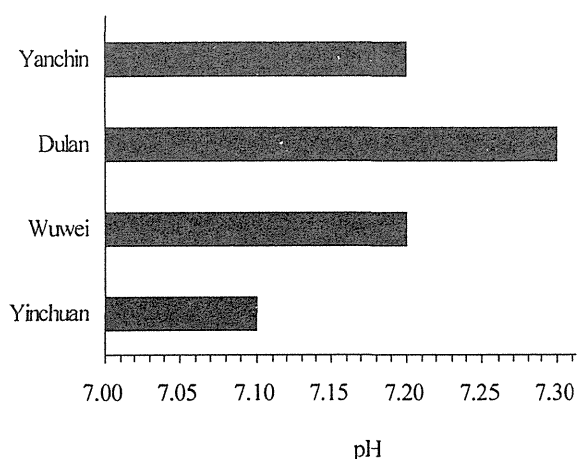


Fig. 4 pH of extracted water from four kinds of desert sands.

sands at four different desert areas were to be the target of bulk and single analyses by means of PIXE and micro-PIXE analyses, respectively. The physical properties of desert sands like morphology, color, and size were basically determined. Also the chemical characteristics of bulk sands of each desert were specified as the relative elemental mass. The elemental maps and spectra for individual sands allow us to understand the nature of individual sands. Consequently, the physicochemical properties of desert sands obtained from this study can be helpful to understand what kinds of man-made pollutants and sea-salts are incorporated into natural Asian dust particles.

References

- 1) C.H. Song and G.R. Carmichael, *Atmospheric Environment* 33 (1999) 2203-2218.
- 2) C.-J. Ma, M. Kasahara, S. Tohno and K.C. Hwang, *Atmospheric Environment* 35 (2001a) 747-752.
- 3) C.-J. Ma, M. Kasahara, R. Höller and T. Kamiya, *Atmospheric Environment* 35 (2001b) 2707-2714.

7.3 Research Activities using Micro-PIXE on the Study of Elements Accumulation by Microorganisms in The Fiscal Year 2003

T. Ohnuki*, F. Sakamoto*, N. Kozai**, T. Sakai***, M. Oikawa*** and T. Satoh***

Advanced Science Research Center, JAERI*

Department of Environmental Science, JAERI**

Advanced Radiation Technology Center, JAERI***

1. Introduction

The presence of radionuclides in nuclear reactors and radioactive wastes is a major environmental concern due to their radiation emissions. In order to estimate the potential impact of radionuclides to human being, we must elucidate the migration behavior of the elements involving radionuclides in geological and terrestrial environment. Abiotic and biotic reactions of the elements should be considered to estimate the impact. In last three decades, many researchers have studied the interactions between the elements and inorganic materials. However, the biotic reactions of the elements have received less attention.

Some microorganisms can accumulate the elements on cell surface and inside cell. Great amounts of elements accumulation have been reported and have been expected to apply remediation methods for the contaminated area. Fundamental understanding of the interaction between the elements and microbes is needed to develop appropriate waste treatment and management strategies as well as to predict the microbial impacts on the long-term performance of the waste repositories.

State-of-the-art analytical techniques should be used to determine the interaction of elements with microorganisms at the molecular level to understand the structure function relationship.

Particle induced X-ray emission (PIXE) is one of the possible methods detecting elements in the level of ppm¹⁾. If we use probe beams of μm order or less in diameter, hazardous elements as well as other elements distribution in a lower plant sample can be determined with such spatial resolution. A light ion microbeam system²⁾ with the spatial resolution of less than 1 μm was constructed on a beam line of 3 MV single-ended accelerator in the TIARA facility at Japan Atomic Energy Research Institute (JAERI). And the in-air μ -PIXE analyzing system was developed on the TIARA facility for chemical analysis with a sub-micron level spatial resolution³⁾. Thus, mapping of hazardous elements of ppm level is available by μ -PIXE.

In fiscal year 2003, we have conducted the following experiments using μ -PIXE analysis.

- (i) Accumulation of Cs by *Saccharomyces cerevisiae*.
- (ii) Accumulation of Pb by *S. cerevisiae*.

Here, we report the detail of accumulation of Cs by *S. cerevisiae*.

2. Objective

Cesium exists in low-level radioactive wastes. This indicates that the interaction of Cs with microorganisms should be elucidated to understand the impact of radioactive waste to environment. The yeast *S. cerevisiae* is a

eukaryot that has with a cell size of approximately 10 μm in diameter. The yeast is known to be accumulate metals⁴⁾. Thus, the μ -PIXE technique was used to examine the accumulation and localization of Cs and the essential elements such as, P, K and Fe in yeast.

3. Experimental

The yeast of *S. cerevisiae* X-2180 was obtained from National Research Institute of Brewing, Japan and was grown in on YPD medium containing the following ingredients: yeast extract (Difco), 10 g; peptone (Difco), 20 g; glucose (Difco), 20 g and agar (Difco), 20g in 1 L DDI. The cells were grown in 100 ml of YPD broth in 500 ml flasks for 24 hours at 30 °C on a shaker at 110 rpm.

The yeast cells were added to 100 ml of YPD medium containing 1mM of Cs. Effect of Cs on growth of the yeast was determined by removing an aliquot at 0.1, 21 and 48 h and measuring the optical density at 600 nm (OD_{600}).

The yeast cells grown in the presence of Cs were removed from the growth medium at 0.1, 21 and 48 h, washed twice with DDI and attached on the sample folders, freeze-dried. and analyzed by μ -PIXE. A proton beam with the energy of 2.6 MeV from the single-ended machine was used for in-air μ -PIXE analysis³⁾, so that the proton penetrates into the yeast exciting elements both on the surface and internal region of the yeast. The beam spot was approximately 1 μm in diameter. The maximum scanning area available at the μ -PIXE set-up was of 740 x 850 μm^2 .

The yeast cells were also examined by scanning electron microscopy (SEM) (JEOL-6330F) operating at a voltage of 15 kV equipped with an energy dispersive X-ray analyzer (EDS) (JED-2140).

4. Results and summary

(1) Micro-PIXE analyses show that the yeast *S. cerevisiae* accumulates Cs during growth when exposed to culture medium containing Cs. The peaks for Cs, as well as P, K and Fe were distinguished in the PIXE spectra. In contrast, only the peaks for P and S were distinguished in the SEM-EDS spectrum.

(2) Micro-PIXE analyses also suitable to monitor the accumulation of Cs during growth, as well as the changes in the cellular elements with time.

In conclusion, μ -PIXE is a useful technique to detect lower concentration of elements in microbial cells than by SEM-EDS, even though the yeast cannot directly observed as with SEM. In addition, μ -PIXE analysis is applicable to monitor the change in concentrations of elements in microorganisms during their growth.

References

- 1) Sueno S., Eur. J. Mineral., 7, (1995) 1273-1297.
- 2) T.Kamiya, T.Suda and R.Tanaka, Nuclear Inst. Method B 118 447-450(1996).
- 3) T. Sakai, et al., Biological Trace Element Research 71-72 (1999)77-82.
- 4) B. Volesky, H.A. May-Phillip, Appl Microbiol Biotechnol 42 (1995) 797.

7.4 Detection of a Single Ion using the Luminescence from $\text{CaF}_2(\text{Eu})$ and $\text{ZnS}(\text{Ag})$

T. Ohshima^{*}, T. Satoh^{**}, M. Oikawa^{**}, and T. Kamiya^{*}

Department of Material Development, JAERI^{*}

Advanced Radiation Technology Center, JAERI^{**}

1. Introduction

For the study of single event upset in semiconductor devices and mutation of tissues induced by ion irradiation, it is necessary to develop irradiation techniques with high accuracy. Up to now, TIARA has developed microbeam irradiation techniques in conjunction with a single ion hit system¹⁾. By using the techniques, transient ion beam induced current can be measured at TIARA, and, as a result, charge collected from electronic devices can be evaluated²⁾. Furthermore, for the study of biotechnology, a microbeam-irradiation-system using a collimator, which is connected with a cyclotron, has been developed³⁾, and microbeam-irradiation into cells has been carried out⁴⁾. Recently, to achieve more precise irradiation, a microbeam formation system using focusing lenses for ions from the cyclotron is now under development at TIARA⁵⁾. With decreasing the size of electronic devices or objective area in

tissues, smaller size of ion beams (*i.e.* nano-beams) and more precise control of irradiation points are expected. For these purposes, it is necessary to develop position-sensing techniques with high accuracy, which can detect a point irradiated by an incident ion.

In this study, we measured the luminescence from $\text{CaF}_2(\text{Eu})$ and $\text{ZnS}(\text{Ag})$ scintillators by incident ions.

2. Experimental Details

The heavy-ion microbeam irradiation line (TB line) connected with 3MV-TANDEM accelerator at TIARA was used in this study^{1,2)}. $\text{CaF}_2(\text{Eu})$ and $\text{ZnS}(\text{Ag})$ scintillators were irradiated with oxygen microbeams at an energy of 15 MeV. After the formation of microbeams at a size of 1 μm , ion beam flux was controlled using a beam-attenuator and a beam-chopper. The luminescence from $\text{CaF}_2(\text{Eu})$ and $\text{ZnS}(\text{Ag})$

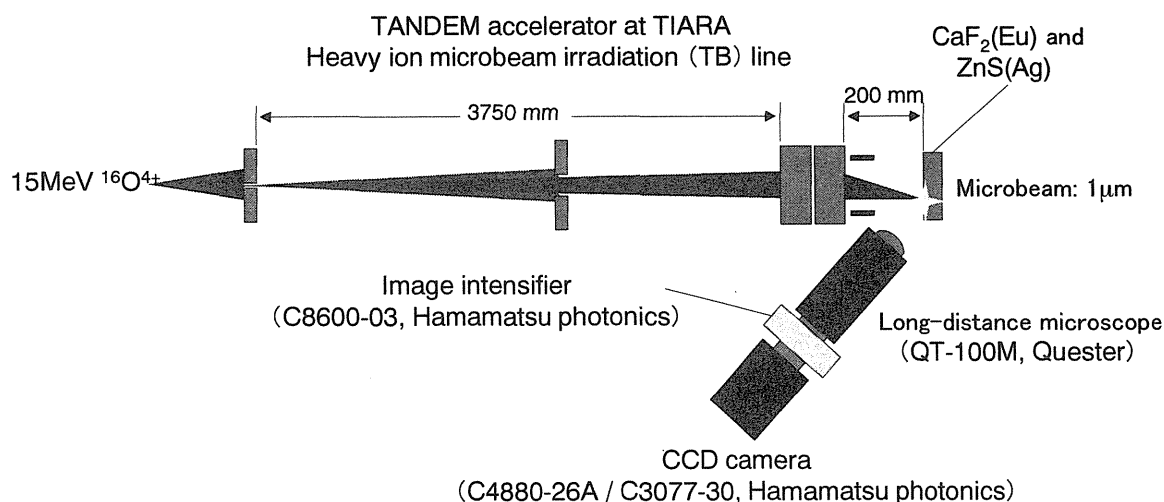


Fig. 1 Incident ion detection system used in this study.

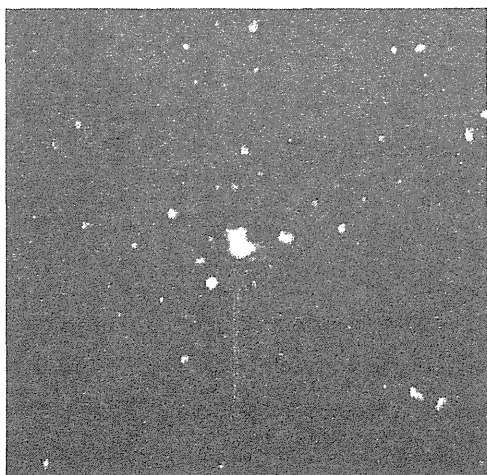


Fig. 2 Luminescence from ZnS(Ag) by an incident 15 MeV-O ion.

scintillators by irradiation was detected by a CCD camera (Model: C3077-70 or C4880-26A, HAMAMATSU Photonics K.K) in conjunction with an image intensifier (Model: C8600-03, HAMAMATSU Photonics K.K) and a long-distance microscope (Model: QT-100, Quester). The luminescence collected by the CCD cameras was analysed, and its profile (position, intensity and distribution) was evaluated. The detection system was illustrated in Fig.1.

3. Results and discussion

Figure 2 shows the luminescence from ZnS(Ag) by an incident 15 MeV-O ion. The beam flux was reduced to be 0.6 cps using the beam-attenuator and the beam-chopper. In our knowledge, the detection of an incident single ion using photo-image has not been reported. Therefore, this article might be the world's first report on real time observation of an incident single ion using CCD cameras.

Figure 3 is the luminescence from CaF₂(Eu) by 15MeV-O microbeams at a diameter of 1 μ m. The image was collected by a sampling system using consecutive microbeams (not single ion

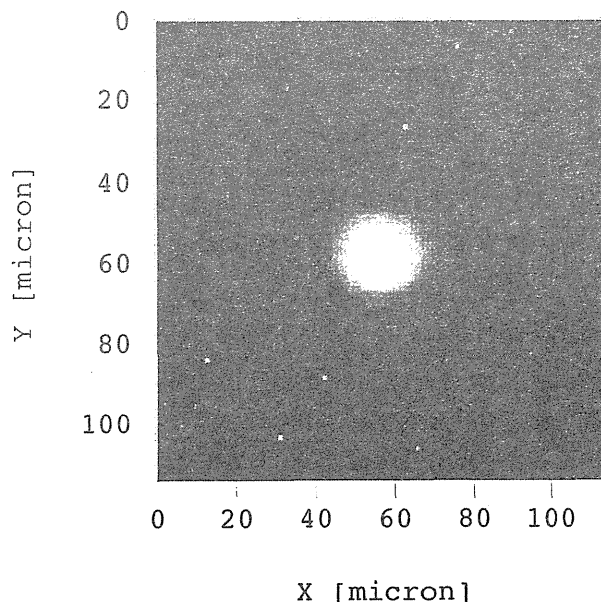


Fig. 3 Luminescence from CaF₂(Eu) by 15MeV-O microbeams at a diameter of 1 μ m.

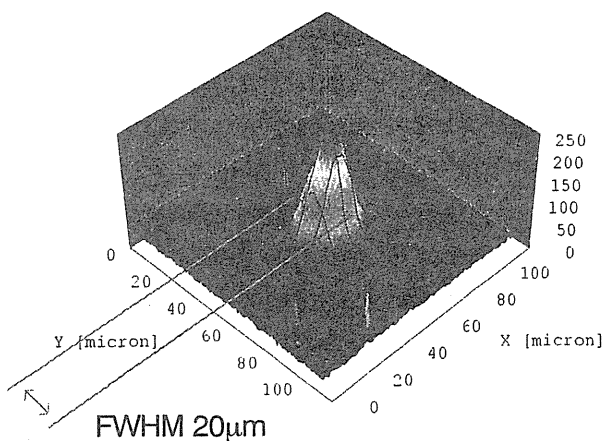


Fig. 4 Contour map of the luminescence obtained from CaF₂(Eu) by 15 MeV-O microbeam irradiation.

hit). The highest intensity of luminescence was observed at the center, and the intensity decreases with increasing distance from the center. To evaluate the luminescence profile, the image was analyzed. The contour map of the luminescence is depicted in Fig. 4. The symmetric spread of the luminescence from the peak at the center is

observed. From the analysis of the contour map, the full width of half maximum (FWHM) is estimated to be 20 μm , as shown in Fig. 4. Since the beam size is 1 μm , the FWHM value obtained in this study indicates that the scintillation by irradiation is about 20 times larger than the beam size.

4. Summary

The luminescence from $\text{CaF}_2(\text{Eu})$ and $\text{ZnS}(\text{Ag})$ scintillators by 15MeV-O ions was evaluated. The luminescence from $\text{ZnS}(\text{Ag})$ by an incident ion can be detected using the CCD camera in conjunction with the image intensifier and the long-distance microscope. The luminescence profile of $\text{CaF}_2(\text{Eu})$ due to microbeam irradiation was analyzed. As the result, the symmetric spread of the luminescence with a FWHM of 20 μm was observed whereas

the size of irradiated beams is 1 μm .

References

- 1) T. Kamiya, T. Hirao, Y. Kobayashi, Nucl. Instr. and Meth. B **219-220** (2004) 1010.
- 2) J. S. Laird, T. Hirao, H. Mori, S. Onoda, T. Kamiya, H. Itoh, Nucl. Instr. and Meth. B **181** (2001) 87.
- 3) T. Kamiya, W. Yokota, Y. Kobayashi, M. Cholewa, M. S. Krochmal, G. Laken, I. D. Larsen, L. Fiddes, G. Parkhill, K. Dowsey, Nucl. Instr. and Meth. B **181** (2001) 27.
- 4) Y. Kobayashi, T. Funayama, S. Wada, M. Taguchi and H. Watanabe, Nucl. Instr. and Meth. B **210** (2003) 54.
- 5) M. Oikawa, T. Kamiya, M. Fukuda, S. Okumura, H. Inoue, S. Masuno, S. Umemiya, Y. Oshiyama, Y. Taira, Nucl. Instr. and Meth. B **210** (2003) 308.

7.5 Multiple X-Ray Detectors for High Efficiency Micro-PIXE Analysis

T. Sakai*, M. Oikawa*, T. Satoh* and S. Nomiya**
Advanced Radiation Technology Center, JAERI*
Raytech Corporation**

1. Introduction

In TIARA facility, in-air micro-PIXE system has been developed ^{1), 2)} and widely used for various applications. Although micro-PIXE is powerful technique for two-dimensional elemental analysis, it takes lots of time to get a clear image of elemental distribution especially in trace elemental mapping. So the improvement of the X-ray detection efficiency is required to reduce the measurement time by micro-PIXE users, because their beam-time is not enough due to the tight TIARA facility schedule.

We have installed two new X-ray detectors in addition to previously served hp-Ge X-ray detector to increase X-ray detection efficiency. One of the new detectors is high energy resolution type for better sensitivity below 2 keV and another detector has large crystal size to improve the detection efficiency above 6 keV X-rays, as described below.

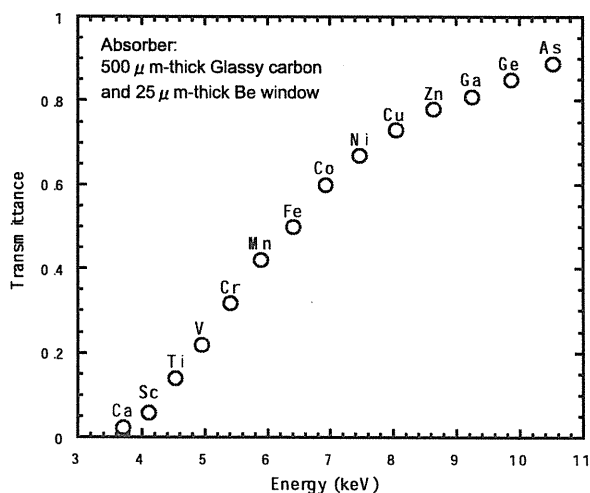


Fig. 1 Calculated transmittance plot with elemental symbols those correspond to their characteristic X-ray energy

2. Instruments

2.1 X-ray detectors

The previously installed hp-Ge X-ray detector (Ortec IGLET-X, 100 mm²) has moderate energy resolution of 160 eV at 5.9 keV Mn K α X-ray and poor detection efficiency below 2 keV because of Ge L-absorption edge and backscattering proton absorber (60 μ m-thick polypropylene) which is attached in front of the detector endcap. New high energy resolution Si(Li) X-ray detector (PGT LS30135, 30 mm²) is set at symmetry position of the hp-Ge X-ray detector respect to the beam axis. Energy resolution of the Si(Li) detector is 135 eV, and the higher energy resolution brings better signal to background ratio and smaller peak overlapping especially in lower energy region. The detector window is 8 μ m-thick Be and attached with an annular type absorber (100 μ m-thick mylar) which has center hole size of 3 mm in diameter, so that the detection efficiency below 2 keV is fairly good.

On the other hand, another new detector is designed to improve the detection efficiency above 6 keV X-rays. An out-of-date hp-Ge gamma ray detector (Aptec PS-305-D7.5C), that has 250 mm² active area with 260 eV energy resolution, is remodeled by Raytech corporation. The endcap of the detector is converted to L-shape to set the detector crystal just behind the sample. Although the configuration provides very large solid angle, a proton beam dumper must be attached in front of the detector window for thin sample analysis. Ultra high purity

glassy carbon (Tokai Carbon co. ltd.) is ideal material for the dumper. Most of X-rays generated by a few MeV proton bombardment onto the glassy carbon are secondary electron bremsstrahlung and carbon characteristic X-rays (280 eV). The main component of the former continuous X-rays is below 6 keV. It is necessary to absorb these low energy X-rays, because they cause pulse pile-up in the detector electric circuit. So we have adopted 500 μm -thick glassy carbon disk as the beam dump that also plays a role of low energy X-ray absorber. Figures 1 and 2 present calculated transmittance with X-ray energy and schematic of these three X-ray detectors configuration, respectively.

2.2 Data acquisition system

PC-based multi-parameter data acquisition (DAQ) system has been used for microPIXE measurement^{2), 3)}. The DAQ software is updated and the PC is replaced to the latest

one to be capable of simultaneous processing the signals from these multiple detectors. The improved DAQ system can manage up to four independent detectors with total count rate of 30 kHz. Beam scanning control is also combined with the system, so that the scan frequency and resolution can be change easily.

3. Performance

The multiple X-ray detection system has advantages of not only for enlarging the active area of detectors but also sharing effective X-ray energy regions between the different detectors. Figure 3 shows an example of X-ray spectra taken by these three detectors. The efficiency below 2 keV is greatly improved by the Si(Li) detector so that the peaks from Na, Mg, Al and Si are clearly observed. This improvement is especially useful for clay-sorption behavior analysis .⁴⁾ On the other hand, the spectrum, that is taken by

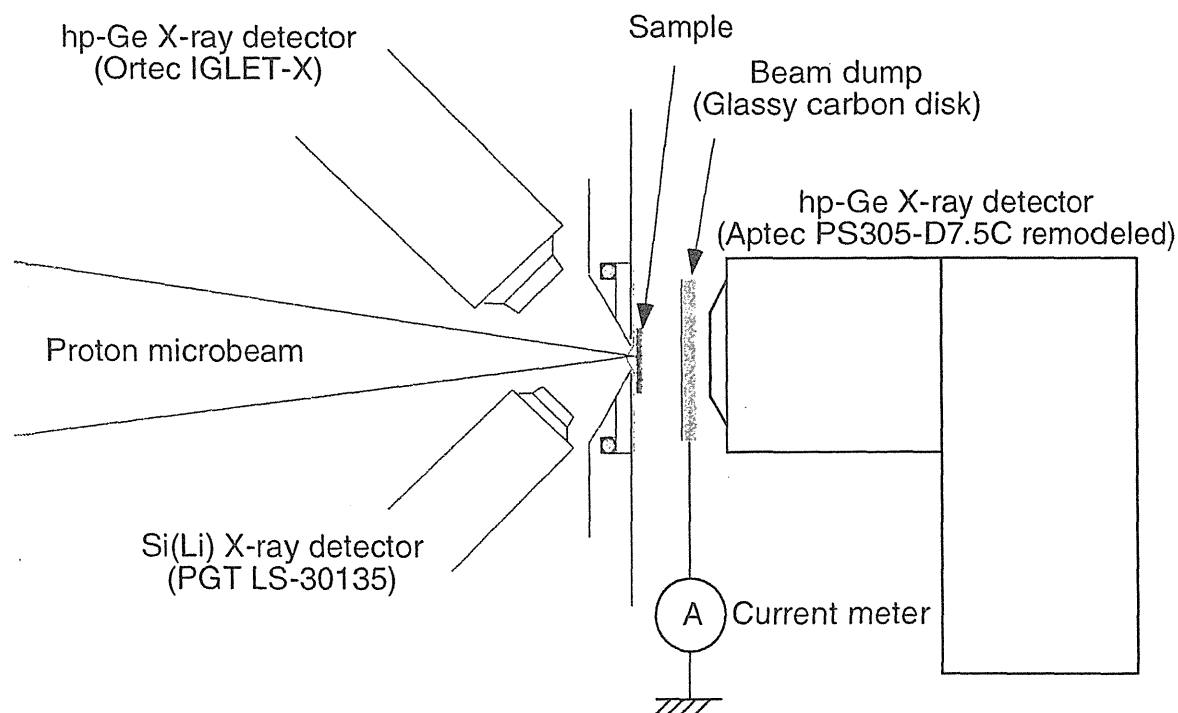


Fig. 2 Schematic of the three X-ray detectors arrangement with the sample

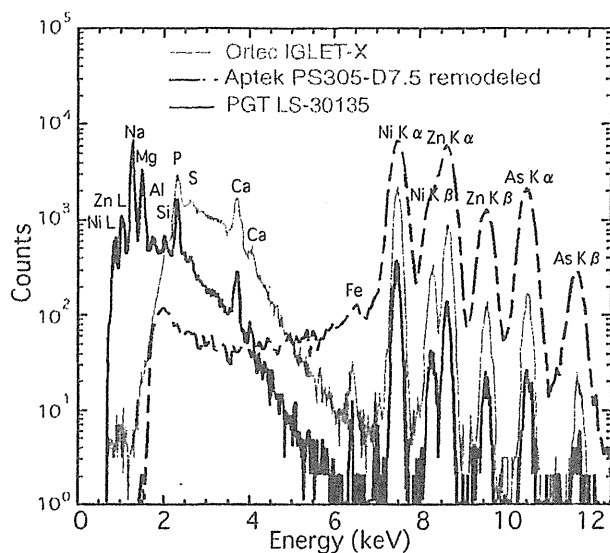


Fig. 3 An example of X-ray spectra taken by three X-ray detectors. The X-rays are generated by 2.6 MeV proton beam bombardment to a clay sample.

the backward X-ray detector, shows almost ten times higher statistics of X-ray counts from heavy elements, such as Ni, Zn and As. The result proved that the new multiple X-ray detection system is succeeded in improving X-ray detection efficiency drastically.

Acknowledgement

The authors would like to thank Drs. M. Fukuda, K. Arakawa, Y. Ohara and the staffs of Raytech Corporation. They also acknowledge Dr. H. Naramoto for providing original detectors and Dr. N. Kozai for permitting to present the X-ray spectra.

References

- 1) T. Sakai et al., Biol. Trace Element Res. 71-72 (1999) 77.
- 2) T. Sakai et al., Nucl. Instr. and Meth. B190 (2002) 271.
- 3) T. Sakai et al., Nucl. Instr. and Meth. B136-138 (1998) 390.
- 4) N. Kozai et al, JAERI-Review 2003-033 (TIARA Annual Report 2002) 212.

7.6 Fluorine Distribution around the Sound and Carious Fissures of Human Teeth

H. Yamamoto*, M. Nomachi**, K. Yasuda***, T. Sakai****Y. Iwami*,
S. Ebisu*, Y. Sugaya**, M. Oikawa****, T. Satoh**** and M. Fukuda****
Graduate school of Dentistry, Osaka University*,
Graduate school of Science, Osaka University**,
Wakasa wan Energy Research Center***,
Advanced Radiation Technology Center, JAERI****

1. Introduction

It has been reported that the fluorine (F) concentration in the carious tooth is higher than that in the sound tooth^{1,2)}. The F distribution around the carious fissure of human teeth has been little known³⁾, though the occlusal fissures have the high caries susceptibility. Because of the narrow and complex structure of occlusal fissures, the application of conventional methods for F measurement, such as the acid etching or abrasion technique, has lacked the accuracy. The estimation of F concentration in the sound and carious fissures, therefore, would become one step for clarifying quantitatively the preventive effect of F on the carious formation.

In this study, we report the F distribution around the narrow fissures of human teeth, using the PIGE methods which we have established at TIARA.

2. Experimental procedure

2.1 Experimental set-up

The experimental facility of the 1.7 MeV proton beam accelerated by the TIARA single-ended accelerator at JAERI-Takasaki, was used for this work. Precise conditions of the measurement were already published in the previous report^{4,5)}.

2.2 Specimens

Human teeth, extracted for the reason of the caries, periodontitis and orthodontics at the Osaka University dental hospital in the six months, were used as the specimens. The teeth

embedded in the epoxy resin were cut through the fissure and grouped visually to three categories by the texture of fissure; Group A: sound fissure, Group B: incipient carious fissure, Group C: medium carious fissure. The width of fissures ranged from about 10 μ m to 50 μ m. The number of each group was 5.

The precise pre-treatment of the specimens was the same as previous experiments and precisely described in the previous reports^{4,5)}.

2.3 Measurement

The measurement areas were about 140 μ m x 140 through 1000 μ m. F concentration at the around the fissure was measured. The obtained raw data were converted to the quantitative values by the reference materials Ca₁₀(PO₄)₆(OH)_{2-2x}F_{2x} (x=0, 0.1, 0.5, 1.0). The maximum values of the F concentration around the surface area of fissures were compared among the groups.

The texture and width of fissures of specimens were observed by photomicrograph.

3. Results and Discussion

Fig.1 (a)-(d) through Fig.3 (a)-(d) show the obtained results as the photos and the 2D mapping form. In all specimens, the F distribution was recognized at the surfaces of fissures. The F concentration at the fissures varied depending on the locations and decreased towards the inner of the tooth. The F distribution at the sound fissure with width of 10 μ m was observed along the fissure (Fig.1c), whereas

those at the carious fissure were irregular.

Fig.1 (e) through Fig.3 (e) shows the F and Ca concentration through the fissures about at the middle of measurement area indicated by the arrows shown in (c) and (d) of the corresponding figures. Fig. 4 shows the maximum values of F concentration around the surface area of the

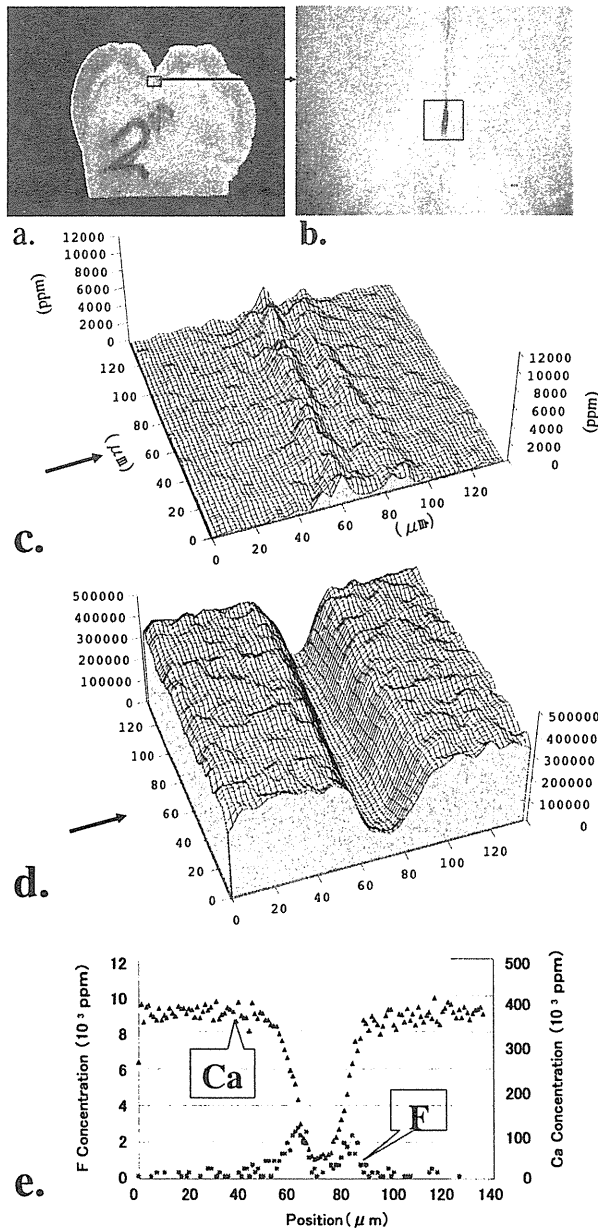


Fig.1. Distribution of F and Ca in Group A (Sound fissure).

(a) Photomicrograph of cut surface of tooth (x4).
 (b) Magnification of square area in (a) (x500).
 Square area shows measurement area. (c) F 2D distribution map. (d) Ca 2D distribution map. (e) Concentration of F and Ca at the cut face along the arrow in (c) and (d).

fissures of measurement area in each group. The values ranged as follows; Group A: 3500~11700ppm (mean=6000ppm), Group B: 2400~10700ppm (mean=6300ppm), Group C: 5200~16900ppm (mean=9300ppm). These concentration showed no significant difference in Mann-Whitney statistical analysis ($p>0.05$).

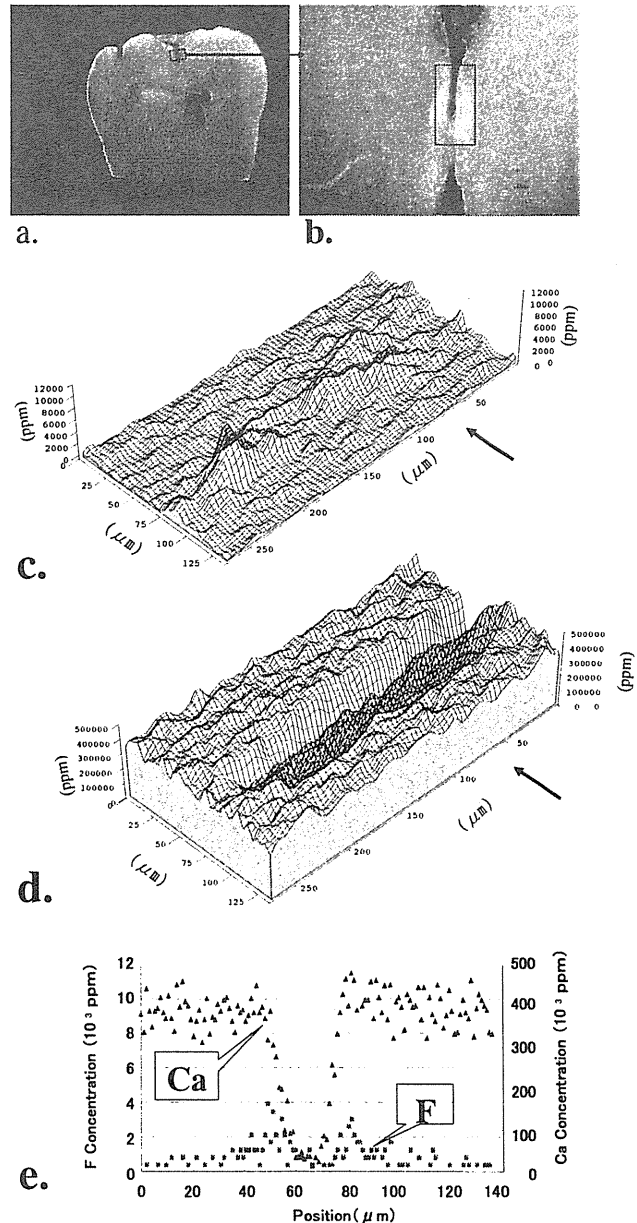


Fig.2. Distribution of F and Ca in Group B (Incipient carious fissure).

(a) Photomicrograph of cut surface of tooth (x4).
 (b) Magnification of square area in (a) (x500).
 Square area shows measurement area. (c) F 2D distribution map. (d) Ca 2D distribution map. (e) Concentration of F and Ca at the cut face along the arrow in (c) and (d).

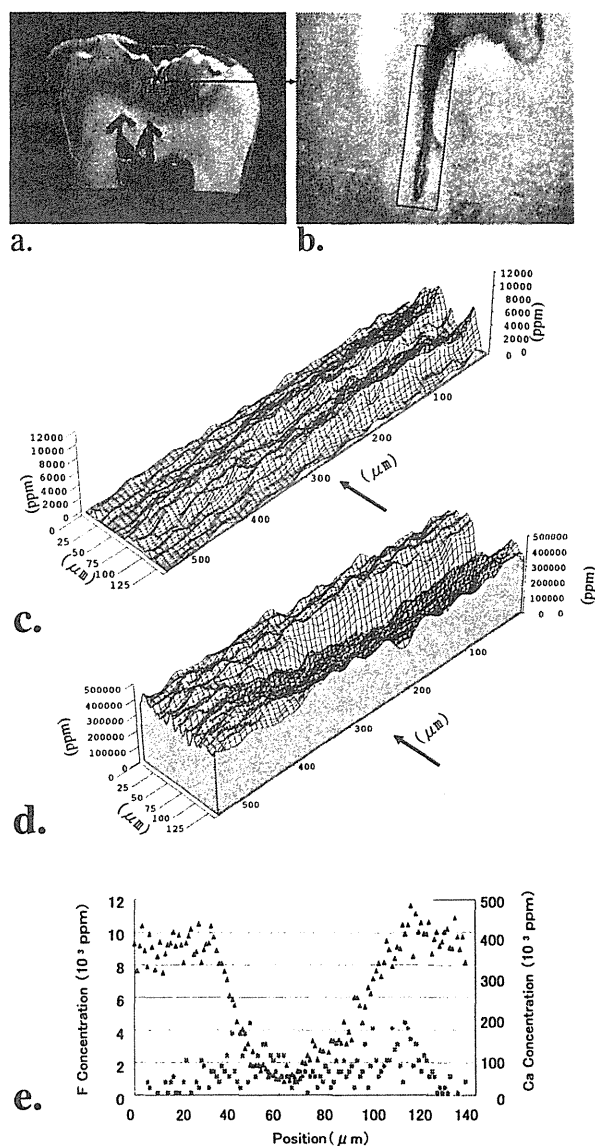


Fig.3. Distribution of F and Ca in Group C (Medium carious fissure).

(a) Photomicrograph of cut surface of tooth (x4). (b) Magnification of squared area in (a) (x500). Square area shows measurement area. (c) F 2D distribution map. (d) Ca 2D distribution map. (e) Concentration of F and Ca at the cut surface along the arrow in the (c) and (d).

The F concentration on the both sides of the fissures with about 10μm width or in the debris contained in the fissure was firstly measured. The high F concentration was recognized in the debris (Fig. 2c). Although the fluoride histories of all the specimens are not known, the F measured at the fissure surfaces was seemed to be not only the original F in the tooth but the acquired F from the outside, compared with the

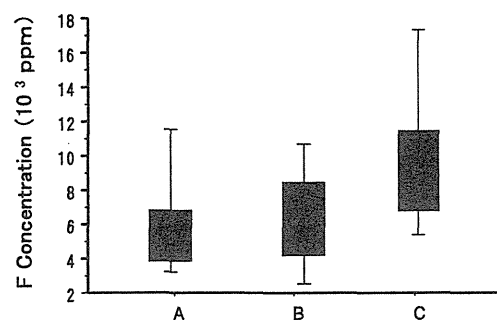


Fig.4 Maximum concentration of F around the surface of fissures

A: Group A (Sound fissure). B: Group B (Incipient carious fissure). C: Group C (Medium carious fissure)

F values reported^{2,6)}. The high F concentration tended to be observed at the carious fissures. But it was not always, since the high value was recognized also at the sound fissures. These phenomena are seemed to relate to the structure of the fissures or the texture of the carious teeth.

In conclusion, F distribution on the both sides of the fissure with width about 10μm could be separately measured. F concentration at the carious fissure was not always higher than the normal tooth.

4. Acknowledgements

We would like to thank members of TIARA, JAERI TAKASAKI for operating the accelerator facility.

References

- 1) A.S. Hallsworth et al., *Analyt. Chem.* 48 (1976) 1660-1664.
- 2) J.A. Weatherell et al., *Caries Res.* 11(Suppl.1) (1977) 85-115.
- 3) E.L.F. Pearce et al., *Caries Res.* 33 (1999) 196-205
- 4) M. Nomachi et al., *TIARA Ann. Rep.* 2000, *AERI-Review* 2001-039 (2001) 244-246.
- 5) H. Yamamoto et al., *Nucl. Instr. And Meth.* B210 (2003) 388-394.
- 6) F. Brudevold et al., *J. Dent. Res.* 35 (1956)

7.7 Modulation of Tissue Samples for Measurement of Cadmium using In-air Micro-PIXE

T. Nagamine*, K. Suzuki*, K. Nakazato*, H.D. Moon*, T. Satoh**,
M. Oikawa**, T. Sakai** and K. Arakawa***

School of health Science, Gunma University *

Advanced Radiation Technology Center, JAERI**

Department of Ion-Beam-applied Biology, JAERI***

1. Introduction

Cadmium (Cd) is considered one of the most toxic substances in the environment due to its wide range of organ toxicity and long elimination half-life of 10-30 years¹⁾. The majority of Cd accumulation occurs in the liver and kidney. The main pathologic changes related to chronic Cd toxicity, renal disease and bone loss, are reflective of Cd concentration in the kidney and the alteration of renal function that ultimately causes osteoporosis and osteomalacia. The mechanism of Cd toxicity are not completely understood; therefore it is necessary to develop the measurement system applicable to Cd accumulated in the organ tissues. By focusing the beam spot within 1 μm (micro-beam) and scanning the samples, the elemental distributions in the sample are observed. In-air micro-PIXE is a convenient and useful apparatus for examining metabolic mechanism in the organ tissues and cell cultures²⁾. Since modulation of the sample measurement is very important for an accurate evaluation, we determine the optimum condition of tissue sample for measurement of Cd using In-air micro-PIXE.

2. Experimental procedure

2.1 Animal and treatment

ICR female mice were kept in the animal facility of Gunma University, with 12-h light/12-h dark regime and at constant temperature (25 °C). The mice were allowed free access to

food and water to which Cd (CdCl_2) was added at levels of 100 mg/litter and 300 mg/litter. The amount of water consumed by each mouse was carefully recorded every day throughout the entire experiment, and the life time Cd uptake for each mouse was up to 230 mg and 540 mg, respectively. Two years after, mice were sacrificed and liver and kidney were removed immediately and stored frozen at -80 °C until further use.

2.2 Procedure for tissue fixation and measurement of Cd

To cut 10 μm and 20 μm frozen sections, the tissue samples were sectioned in a Leica CM 1850 cryostat. Sections were placed onto the 20 μm thick of Mylar film. One sample specimen was immediately fixed to a sample holder with a bonding agent (the frozen sample), the other was infiltrated with 95 % ethanol for 30 seconds then fixed to a sample holder (the ethanol sample).

The 2.6 MeV proton beam, 1 μm of beam spot size, accelerated by the TIARA single-ended accelerator at JAERI-Takasaki was used for measurement of Cd in the tissue samples. Precise conditions of measurement were reported previously³⁾.

3 Results and discussion

The element distribution images of liver and kidney sample obtained from the mouse dosed with 300 mg/litter of Cd was shown in Fig.1 and 2. The X-ray yield of Cd was distinctly

determined in the 20 μm frozen sample; the peak value of Cd is higher in the liver than in the kidney. The yields of P, S and K were also demonstrated (Fig.1). The yield of Cd in the 10 μm frozen sample was reduced by half of the 20 μm frozen one. The Peak of Cd in both 10 and 20 μm the frozen samples disappeared in the ethanol samples. In addition, the X-ray yield of K decreased in the ethanol samples, whereas the yield of P and S were unchanged (Fig.2). In the mice treated with 100 mg/litter of Cd, the X-ray yield of Cd was slightly determined in the 20 μm frozen samples, but not in the 10 μm frozen ones. We failed to determine the distribution of Cd in the ethanol samples. The yield of P, S, and K were demonstrated in the frozen samples, but the yield of K decreased in the ethanol ones.

Distributions of Cd in the kidney and liver cells almost coincided with those of other elements such as P, S, K, Fe and Zn. Present data suggest that the 20 μm frozen section of tissue sample is desirable for measurement of Cd using In-air micro-PIXE and is essential to dry naturally. If the frozen tissue is infiltrated with ethanol, Cd may diffuse concomitant with loss of K.

References

- 1) L.Jarup, M.Berglund, CG Elinder, et al. Scand J Work Environ Health 24(1998)1-51.
- 2) Y.Komori, K.Ishii, Y.Barbotteau, et al. TIARA Ann Rep.2002 JAERI-Review 2003 -033, 279-281
- 3) T.Sakai, T.Kamiya, M.Oikawa, et al. Nucl Instr Meth B190(2002) 271

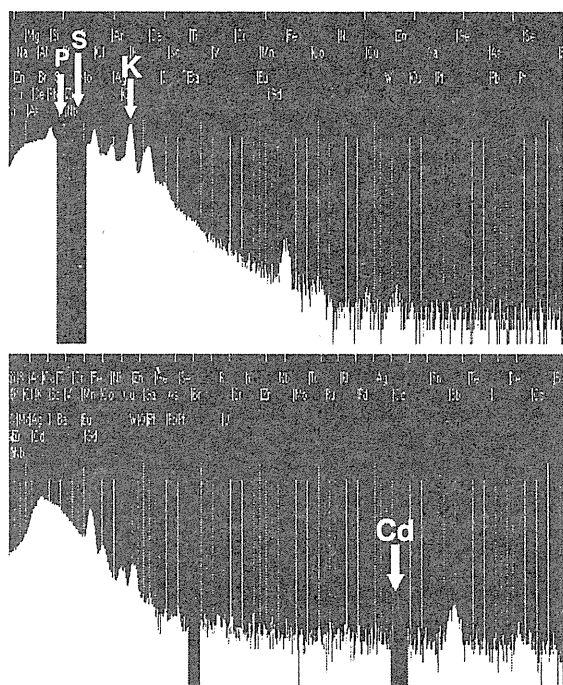


Fig.1 Spectrum of mouse liver dosed with 300mg/L of cadmium for 2 years

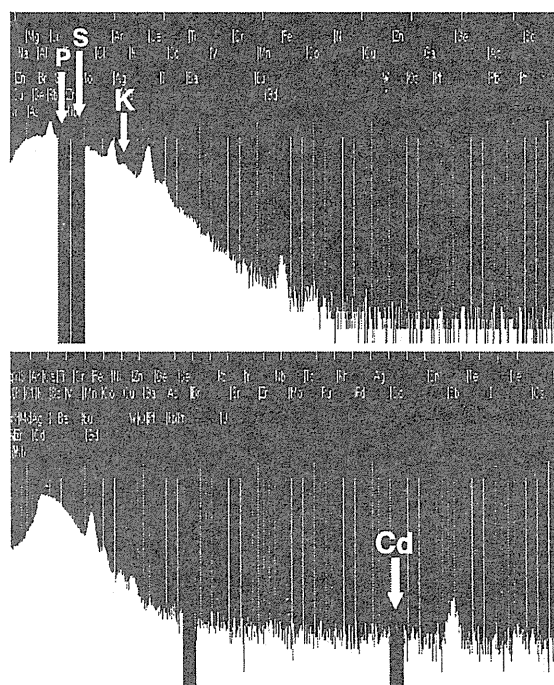


Fig.2 Spectrum of mouse liver dosed with 300mg/L of cadmium after infiltrated with ethanol

7.8 Fundamental Research of Grazing-exit PIXE

K. Tsuji*, T. Sakai** and S. Yamamoto***

Department of Applied Chemistry, Osaka City University*

Advanced Radiation Technology Center, JAERI**

Department of Material Development, JAERI***

1. Introduction

In particle-induced x-ray emission (PIXE), usually, a proton beam of several MeV energy bombards solid samples, and excites the electrons of the inner shells of the atoms. In the process of deexcitation, x-rays are emitted from the sample. Proton-induced x-rays are normally measured by an energy-dispersive x-ray (EDX) detector. PIXE makes non-destructive analysis possible with high sensitivity. Furthermore, in microbeam-PIXE (micro-PIXE), the analysis with excellent spatial resolution of the order of 1 μm is possible. Therefore, PIXE is well recognized as a micro- and trace-analytical method. It has been applied in various fields such as: biology, environmental chemistry, earth science and archaeology. In the case of excitation with an electron beam, *e.g.* electron probe microanalysis (EPMA), a very large background, which is caused by Bremsstrahlung induced by the primary electrons, is a serious drawback which limits the detection power. In contrast to this, a low background is observed in PIXE spectra. Therefore, the detection limit in PIXE is about 100 times lower than in EPMA. However, the detection limits for light elements in PIXE analysis are not so low, because the background in the low energy region is rather high because of secondary electrons. This limits the applications of PIXE, because light elements such as Al, Si, Na and Ca, which have characteristic x-ray peaks at lower energies, are important components of aerosols or biological samples. Thus, we have studied on the reduction of the background in PIXE spectrum by applying a grazing-exit measurement technique.

The grazing exit technique has been applied to x-ray fluorescence analysis and EPMA, which are named as grazing exit (or emission) XRF (GE-XRF) and grazing exit EPMA (GE-EPMA), respectively. This method is closely related to grazing incidence measurement. In the grazing exit measurements, x-rays emitted from the sample are detected under very small exit angles, normally several mrad. Since the x-rays produced in the depth of the sample can not be observed at grazing-takeoff angles, due to reflection and refraction effects at the interface, grazing exit methods make a surface analysis (nano-meter order) possible.¹⁾ The background is reduced under grazing exit conditions; therefore, GE-EPMA measurement is useful to improve the signal-to-background ratio. In addition to the reduction of the background, enhancement of the characteristic x-ray intensity has also been reported for GE-XRF and GE-EPMA. The preliminary research of GE-PIXE has been reported elsewhere^{1,2)}.

2. Experimental procedure

The experimental setup for GE-PIXE measurement was newly constructed. The most important point is how to control the exit angle of characteristic x-rays. In this time, we introduced a rotating stage, where the sample was attached. This rotating stage was controlled by a PC using a stepping motor. A slit was also attached between the sample and the detector in order to restrict the solid angle for detection. The experimental setup is shown in Fig. 1.

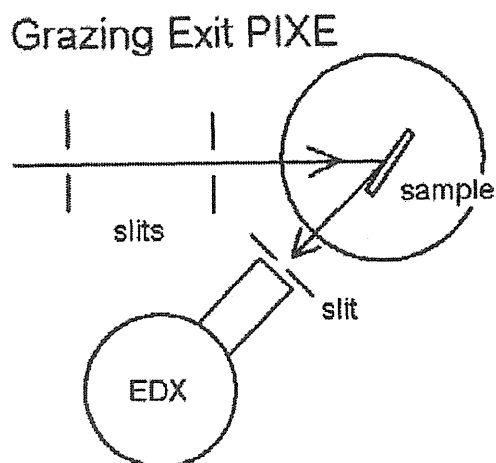


Fig. 1 Experimental setup for GE-PIXE

The sample was Ti/Cr thin film (10 nm in thickness) deposited on Au film (100 nm) on Si wafer.

The sample was irradiated with a 2.0 MeV proton beam at an incident angle of about 45 degrees. The exit angle was changed by rotating the sample, while an EDX detector was fixed.

3. Results and Discussion

The result is shown in Fig. 2. At the large exit angles, Si Ka was dominant, because Si Ka was emitted from the thick sample substrate. The intensities of Ti Ka and Cr Ka, emitted from the top layer, were almost constant in the angle range from 1 to 12 degrees, while Si Ka intensity decreased as the exit angle decreased. The intensities of Ti Ka and Cr Ka drastically increased two times at grazing-exit angle of about 0.5 degrees, and then decreased. The exit angle where the intensity increased corresponds to the angle for total reflection when we consider the Ti Ka or Cr Ka impinge on the Ti-Cr thin film.

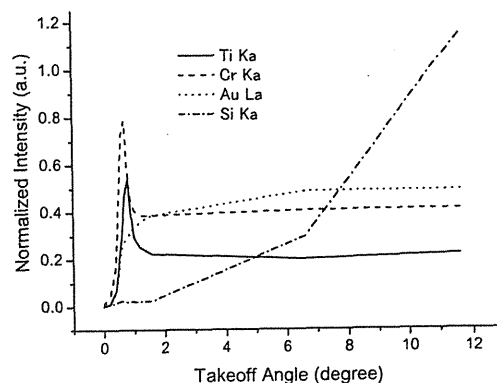


Fig. 2 Exit angle dependence of Ti Ka, Cr Ka, Au La and Si Ka emitted from the Ti-Cr thin layer on Au layer on Si wafer.

Of course, such total reflection does not occur. However, we can understand this situation from reciprocity theorem. It is well known that the total reflection angle depends on energy of x-rays. Actually, the exit angles at maximum peaks for Ti and Cr in the angle dependent curves changed each other, as shown in Fig. 2. The increase of the intensity at these angles is caused by interference of characteristic x-rays in the thin film. Therefore, the shape of the curves should change depending on the thickness of thin films.

As the PIXE spectra are shown elsewhere¹⁾, the background intensity decreases at grazing-exit angles. This indicates that the GE-PIXE is useful for improvement of S/B ratio, leading to micro-trace analytical method.

References

- 1) K. Tsuji, Z. Spolnik, K. Wagatsuma, R. E. Van Grieken, R. D. Vis, *Anal. Chem.* **71**, 5033-5036 (1999).
- 2) K. Tsuji, M. Huisman, Z. Spolnik, K. Wagatsuma, Y. Mori, R. E. Van Grieken, R. D. Vis, *Spectrochim. Acta B*, **55**, 1009-1016 (2000).

7.9 Analysis of Intracellular Distribution of Boron and Gadolinium in 9L Sarcoma Cells using a Single-ended Accelerator (Micro-PIXE)

K. Endo*, Y. Shibata*, H. Yoshida*, K. Nakai*, T. Yamamoto*,
A. Matsumura*, K. Ishii**, K. Mizuma**, T. Sakai***, T. Satoh***,
M. Oikawa***, K. Arakawa***, H. Kumada**** and K. Yamamoto****

Department of neurosurgery Institute of clinical medicine University of Tsukuba*

Department of Engineering, University of Tohoku**

Advanced Radiation Technology Center, JAERI***

Department of Research Reactor, JAERI****

1. Introduction

In patients with a malignant brain tumor, we usually first excise as much of the tumor mass as possible and then prepare the patient for radiation therapy and / or Chemotherapy for tumor cells that might remain diffusely distributed in normal brain tissue. This therapeutic strategy has not proved completely effective so far, thus we have been investigating usefulness of Boron Neutron Capture Therapy (BNCT). And we have been investigating effectiveness of boron and Gadolinium as elements to capture neutrons. The objective of this study was to investigate the movement and distribution of these two elements in the cells. We also discuss the possibility of using gadolinium for clinical medical therapy.

2. Experimental procedure We used the JAERI Single-Ended Accelerator for Micro PIXE to quantify intracellular boron and gadolinium. This machine produces a micro beam of 1 micrometer in diameter and allow us to analyze the distribution of these elements directly. As for the procedure, first we fix the Mylar membrane with a glass ring and a bite

ring of 2 cm in diameter. After washing well, we put 9L sarcoma cells on this membrane and culture these cells in minimum essential medium (MEM) at 37°C until they form a monolayer. Next we add the Gd-BOPTA to the culture and incubate the cells for 24~72 hours at 37°C. Then we wash the membrane in THAM liquid and place it immediately above liquid nitrogen for few minutes. After that the membrane is vacuum-dried for 24 hours to fix these cells on the holder. In this phase, the most important thing is to fix the cells evenly to analyze the distribution of elements in the cells with Micro PIXE.

3. Results and discussion

According to the results of the latest experiment, we were able to analyze the distribution of P, S, Gd, etc. And we could see them in the cells themselves (Fig.1). But we observed the distribution of K and Gd around the cells which are in the cells originally (Fig.2). This indicated the cells wall had been destroyed or just damaged, and the things of intracellular were flown out to the outside of cells by some reasons. Or gadolinium had not been uptaken by

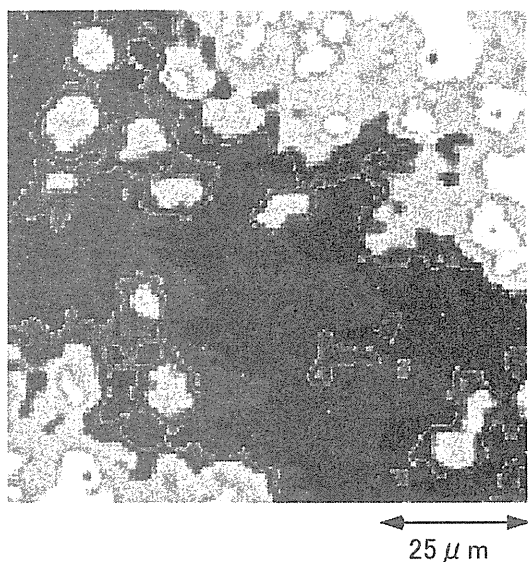


Fig.1
Distribution of P in 9L sarcoma cells.

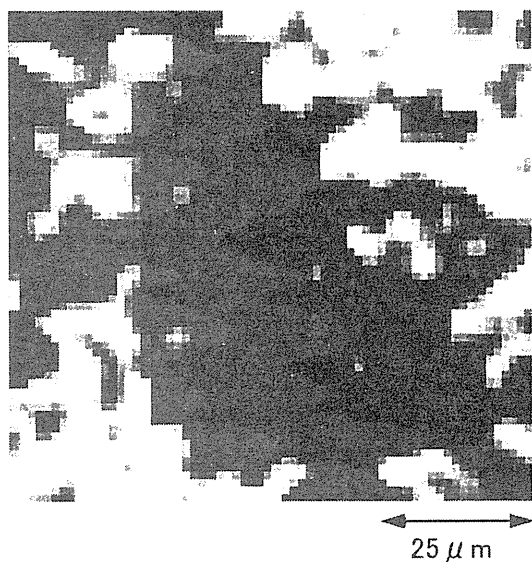


Fig.2
Distribution of Gd around or intra 9L sarcoma cells.

the cells, or that washing was insufficient. Another reason is the way of cells fixation, we think. Now we are trying to solve some problems regarding analysis, fixation method, technical problems, etc.

References

- 1) Matsumura A, et al., Monduzzi Editore, Bologna, 1073-1078, 2002.
- 2) Tian Zhang, et al., AJNR 23:15-18, January 2002.
- 3) Gelsomina De Stasio, et al., CANCER RESEARCH 61, 4272-4277, May 15, 2001.

7.10 A Second Devise for the Target Preparation of the Micro-PIXE Camera for the Floating cells

S. Harada*, S. Ehara*, K. Ishii**, S. Matsuyama**, H. Yamazaki**,
S. Obara***, T. Sakai***, T. Satoh***, M. Oikawa***, K. Mizuma**,
K. Hotta**, T. Izukawa** and S. Anbe**

Iwate Medical University, Department of Radiology*

Department of Quantum Science and Energy Engineering Tohoku University**

Advanced Radiation Technology Center, JAERI***

1. Introduction

Micro Particle Induced X-ray Emission (PIXE) camera has enormous potential for evaluating the biomedical samples. For the preparation of the target, the biomedical samples must be stucked on the mylar film. However, this method is not well established. Several investigators informed that the adhesion of cells brought about the cell deformity, which results in the injury of cell membrane¹⁾. The injury of cell membrane brought about the elution of the trace-elements of the cell, which lead to the inaccurate analytical results of the micro PIXE camera¹⁾. We have evaluated the trace elements in human leukemic cells, using micro PIXE camera. In our previous study, the two kinds of preparation of samples was tested: (1) the cells were adhered to the mylar film by culturing the cells on the mylar film²⁾; and (2) cell suspension was dropped on the mylar film that was cooled through the isopentane, spread out using the glass stick³⁾. The former method brought about the cell deformity and the loss of P in the cell, which suggests that the cell deformity brought about the injury of the cell membrane; and resulted in the elution of elements in the cell²⁾. The latter has less deformity of cells and made a prominent PIXE spectrum; however, the destroyed cells by spreading out procedure were observed on the mylar film²⁾. In this study, a new target preparation was developed in order to prevent the cell deformity and elution of the trace elements from the cell.

2. Experimental procedure

2.1 Preparation of the cell suspension:

The human leukemic cells (OCI/AML-2) cultured in RPMI 1640 medium in 9 cm dish were used in this study. The cell was harvested by centrifuge at 1000 rpm for 5 min, and then washed by the same centrifuge with THAM buffer for three times (Fig.1A). After washing the cells, the number of cells was counted and its concentration was adjusted to $1.0 \times 10^7/\text{ml}$.

2.2 Preparation of the mylar film:

The mylar film was mounted by putting the mylar between the rubber and glass ring, and wiped using the Bencott soaked with acetone. On the other hand, the 1ml of isopentane was poured in the stainless beaker, and the mounted mylar film was placed in the bottom of the beaker(Fig.1B). The plastic ring was placed on the mylar film inside the rubber and glass ring. Then the beaker was placed in the vat filled with liquid nitrogen more than 5 minutes (Fig.1C). With this method, the mounted mylar film was cooled through isopentane.

2.3 Making the targets:

The cell suspension was poured onto the cooled mylar film inside the plastic ring(Fig.1D). The dropped suspension was immediately frozen. After this procedure, the mylar film was frozen dried at 1×10^{-4} Torr for 96 hours. Then, used as targets.

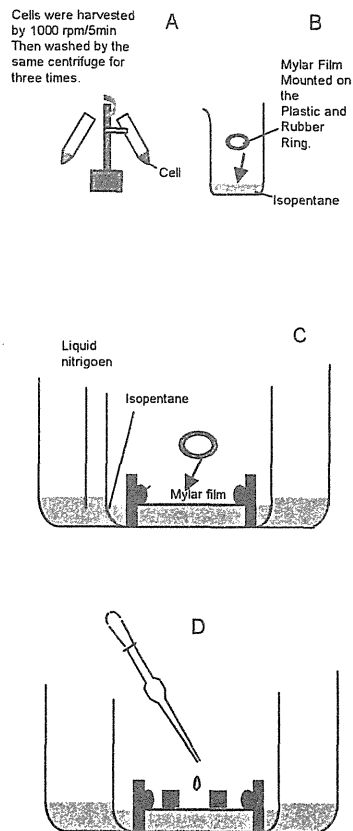


Fig 1. The target preparation of the floating cells. A) Cell harvest and washing cells by 1000 rpm/min; B) the preparation of the mylar ring and placing on the isopentane; C) Cooling of mylar film by liquid nitrogen through isopentane with small ring placed on it; D) Dropping the cell suspension inside of the small ring of cooled mylar film

3. Results and Discussion

The spectrum of PIXE and the microscopic view of the cells are shown Fig. 2A and -B, and -C respectively. Fig. 2A shows the spectrum and cell by the primitive method that the cells were adhered to the mylar film by culturing the cells on it. Fig. 2B shows those by the method of the first device, that is, cells were adhered on the mylar film by dropping and spreading out the cell suspension on mylar film. Fig. 2C represents those by the method of final device, that is, the cells were dropped inside of the small ring of mylar film and frozen dried. With the target preparation used in Fig. 2A, there were deformity of cells; however, in the method used in Fig. 2B, the extent of the cell deformity was

small. In the PIXE spectrum, there was a considerable improvement when compared with Fig. 2-A. With the latest method used in C, the cell deformity was smaller and spectrum was more prominent, when compared with B.

We developed the target preparation for the floating cell for two times. The devised method resulted in a lesser degree of deformity of the cells and the prominent spectrum of PIXE. This method will lead to the accurate analysis of micro PIXE camera for studying the floating cell.

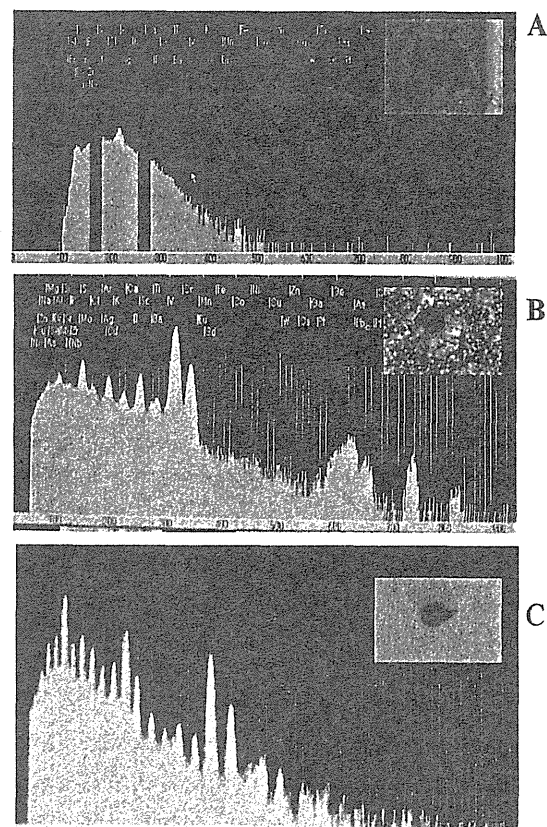


Fig. 2. The PIXE spectrum of the cells after the target preparation. A: Previous method. B: Method of the first improvement. C: The current method. The level of deformity of the cells was remarkably decreased by the current improved method.

References.

- 1) DeMali, KA.; Burrige, K; J. of Cell Sci. 116(Pt 12), (2003) 2389-97.
- 2) Satoshi Harada et. al. Nucl. Instr. Meth. Phys Res. 210 (2003) 383-387
- 3) Satoshi Harada, et. al. Proceedings of the PIXE 2004 IN PRESS.

7.11 Development of Standard Reference Material for PIXE Analysis

Y. Iwata*, K. Ishizawa*, T. Sakai**, T. Satoh**, M. Oikawa**

Department of Chemistry, Faculty of Education and Human Studies,
Akita University*

Advanced Radiation Technology Center, JAERI**

1. Introduction

Standard Reference Material (SRM) is indispensable to the calibration of apparatus and the evaluation of the accuracy and precision of analytical technique. A lot of SRMs have been prepared and issued. Conventional SRMs are suitable for bulky samples in liquid or solid form and they are applied to many kinds of analytical technique such as spectrophotometric analysis, mass spectrometric analysis and activation analysis¹⁾.

Particle Induced X-ray Emission (PIXE) is a powerful tool for multi-element analysis to biological and environmental samples²⁻⁵⁾. The highest sensitivity is obtained by 2-3 MeV proton bombardment, and the sensitivities for most essential and toxic elements of organisms are 0.1 - 4 ng / cm². PIXE is well suited for trace analysis of a small, <0.5 mg or thin, <1 mg/cm² target on a thin film target with organic specimens. PIXE has so unique and particular suitability to properties of analytical sample. New SRMs are necessary for PIXE analysis.

In this study we prepared three types of SRM for PIXE.

- 1) Spot Sample made by dropping several kinds of standard solution on an organic film
- 2) Particle Sample made by adsorption of metal ions on ion-exchange resin,
- 3) Vapor Coating Sample prepared by electron beam evaporation of metal and salt to an organic film

Utilities of these samples are investigated by 3 MeV proton bombardment by Micro Beam

System of TIARA.

2. Experimental

2.1 Preparation of Spot Sample

5 µl Portion of multi-element standard solution containing 10-1000ng of Mg, S, Ca, Cu, Zn and Sr was dropped on polypropylene film (4 µm) and dried by air.

2.2 Preparation of Particle Sample

Ion-exchange resin (Chelex-100, 100-200 mesh, BioRad) was shaken with standard solution of Cu²⁺ for 15 h and dried by vacuum drying under 2 mmHg for 6h. Concentration of Cu on ion-exchange resin was 2, 5 and 20ppm based on dry weight.

2.3 Vapor Coating Sample

Vapor Coating Samples were made by Micro-Matter Co. USA. A 2.5 µm thick Mylar film was coated with 48-54 µg/cm² Ag, RbI, GaP, CaF and NaCl by electron beam evaporation.

3. Results and Discussion

3.1 Properties of Spot Sample

Spot samples were subjected to 2.9 MeV proton bombardment by a cyclotron of Nishina Memorial Cyclotron Center (NMCC) and a Si (Li) detector measured X-rays. Metal salt on Spot Sample was heated by proton bombardment and a part of salt was evaporated to vacuum chamber. Self-shielding of X-rays from light elements such as Mg and S was observed in a spectrum. During target preparation, metal salt often removed from

polypropylene film. By this experiment, simple Spot Sample is not suitable for standard reference material for PIXE.

3.2 Properties of Particle Sample

Particle Samples were subjected to 3 MeV proton bombardment by Micro Beam System of TIARA. STIM image (left) and micro PIXE image (right) of 20 ppm Cu sample were shown in Fig. 1. Micro PIXE image was made by X-ray intensity of Cu K α X-ray region. Image for ion-exchange resin and distribution of Cu in the resin were clearly observed by Micro Beam System of TIARA. Minimum concentration of Cu for imaging was estimated as 5 ppm by proton bombardment.

Particle Sample is similar to biological cell because it is round and matrix elements are

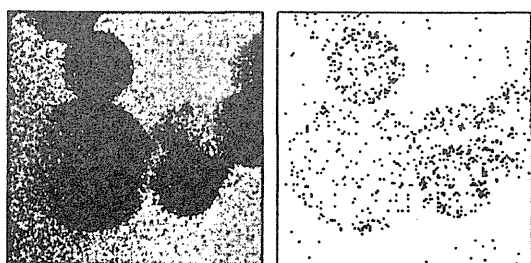


Fig. 1 STIM image (left) and micro PIXE image (right) of ion-exchange resin by Micro Beam System of TIARA

Cu: 20 ppm, Scan area: 350 μm x 350 μm
Charge: 350 nC, Irradiation time: 64 min.

carbon, oxygen and hydrogen. Particle Sample has a possibility for use as pseudo-biological SRM.

3.3 Properties of Vapor Coating Sample

Vapor Coating Samples were subjected to proton bombardment by Micro Beam System of TIARA and NMCC cyclotron. Images for deposit elements obtained by micro beam bombardment (ca. 1 μm x 1 μm) shows homogeneous distribution of elements on the Vapor Coating Samples.

Concentration levels for coated element on the sample are several dozen times higher than biological levels, so proportion of X-ray spectrum for each Vapor Coating Sample are different from biological samples.

References

- 1) Y. Iwata and N. Suzuki, J. Radioanal. Nucl. Chem., 233 (1998) 49-53
- 2) K. Saitoh, Y. Iwata, K. Hirano, Intern. J. PIXE, 8 (1998) 147-153
- 3) Y. Iwata and M. Suzuki, Intern. J. PIXE, 10 (2000) 27-35
- 4) Y. Iwata, J. Radioanal. Nucl. Chem., 249 (2001) 343-348
- 5) K. Saitoh, Y. Iwata, K. Sera, K. Hirano Intern. J. PIXE, 13 (2003) 51-64

7.12 The Elemental Analysis of IGE-sensitized RBL-2H3 Cells using in Air Micro-PIXE

K.Mizuma*, K.Ishii*, Y.Barbotteau*, S.Abe*, H.Yamazaki*, S.Matsuyama*, E.Sakurai**, K.Yanai**, T.Kamiya***, T.Sakai***, T.Satoh***, M.Oikawa*** and K.Arakawa****

Department of Quantum Science and Energy Engineering, Tohoku University *

Department of Pharmacology, Tohoku University School of Medicine **

Advanced Radiation Technology Center, JEARI***

Department of Ion-beam-applied Biology, JAERI****

1. Introduction

Particle induced X-ray emission (PIXE) using micro-beam enables the measurement of the distribution about trace elements at the micron level. The In Air micro-PIXE to reduce the irradiation damage of biological sample has been developed at the division of Takasaki ion accelerator for advanced radiation application (TIARA) in Japan Atomic Energy Research Institute (JAERI).^{1,2)} So far, we have developed the sample preparation for In Air micro-PIXE analysis about cultured cell and tissue.^{3,4)}

Here, we applied In Air micro-PIXE analysis to investigate the relationship between the physiological functions and the role of elements concerning Rat basophilic leukaemia cells (RBL-2H3). This cell has many granules in the cytoplasm. The granules contain chemical mediators, histamine and heparin, which contain sulfur. This cell has high-affinity receptors (FcεRI) for the Fc region of IgE on the cell-surface membrane. The Fc region is the antibody tail which is formed with two heavy chains including 440 amino-acids. Cross-linking of two adjacent IgE antibodies bound to the FcεRI receptors with an antigen is a critical step for increasing the Ca^{2+} level in cytoplasm and triggering the degranulation or the release of mediators in

granules⁵⁾. For that reason, the distribution of sulfur and calcium are considered to change in the cells which induced the degranulation.

2. Experiment

2.1. Sample preparation

RBL-2H3 cells were cultured in Eagle's minimum essential medium (MEM) with 15% fetal bovine serum in a flask in a humidified atmosphere of 5% of CO_2 in air. RBL-2H3 were incubated overnight on the 5 μm Polycarbonate film and sensitized with 0.5 $\mu\text{l/ml}$ of monoclonal IgE for 30 min. After sensitizing RBL-2H3 cells with IgE, the MEM was replaced with PIPES buffer (25mM PIPES (piperazine-N,N'-bis(2-ethanesulfonic acid)), 119mM NaCl, 5mM KCl, 5.6mM glucose, 0.4mM MgCl_2 , 1mM CaCl_2 , 40mM NaOH₂, 0.1% BSA (albumin from Bovine Serum), pH 7.2), and the cells were pre-incubated at 37°C for 20 min. RBL-2H3 cells were stimulated with 10 ng/ml of vitamin D-binding protein (DBP)- human serum albumin (HAS) as an antigen for the indicated periods. The released histamine in the supernatants was measured by high performance liquid chromatography fluorometry. Then the cells on a 5 μm polycarbonate film for microanalysis were washed with THAM buffer solution (0.12 M tris(hydroxymethyl)aminomethane- HNO_3 ,

H7.4). The specimens were promptly dipped into isopentane (2-methylbutane) and chilled with liquid nitrogen and then freeze-dried overnight in the vacuum stage.

2.2. Analysis

In air analysis, the damage during irradiation can be decreased to suppress the temperature rising with gas flow. A proton micro-beam with 2.6 MeV from single-ended machine, 1.0 μm diameter and about 100 pA intensity, was scanned over the sample in order to determine the elemental distribution of the sample. The beam passes through a 5 μm polycarbonate film and irradiates the sample in the air. X-ray was detected with Si(Li) detector (PGT LS30135, 30 mm^2) and HP-Ge detector (ORTEC IGLET-X, 100 mm^2) placed at 140° with respect to the beam axis. Data taking is made by PC-based systems. Data analysis is made by micro-PIXE analysis software developed at TIARA.

3. Results

Micro-PIXE analysis of control RBL-2H3 cells and IgE-sensitized RBL-2H3 cells were shown in Fig.1 and 2.

Figures show the change of cellular shape before and after sensitization.

After the stimulation, the endo-elemental distributions were spread compared to the control samples and the elemental distributions which seem to show the lack of granules were observed.

For a part of stimulated cells, furthermore, the P distribution does not correspond to the S distribution in the cells. At the same place, the concentrations of Na, Ca, Zn, Fe were observed (Fig.2). Three of 80 cells showed these phenomena. And with same sample preparation, 4 of 107 cells had the same kind

of elemental distributions. These phenomena were not observed in any control samples.

4. Discussion and Conclusion

It has been reported that granule matrices accumulate not only Ca, but also Na, Cl from the surrounding saline when they are exposed to extracellular milieu⁶⁾. Therefore, the characteristic distribution of S and the localizations of Na, Ca, Fe and Zn were considered to indicate the elemental distribution at the moment when cells carried out the exocytosis. Thus, In Air micro-PIXE analysis can be used to reveal the dynamic role of elements relevant to the exocytosis of cells.

References

- 1) T. Kamiya, T. Suda, R. Tanaka, "Sub-micron microbeam apparatus for high resolution materials analyses" Nucl. Instr. and Meth. B118 (1996) 447-450
- 2) T. Sakai, Y. Naitoh, "An External Ion Microbeam for Studies of Biological Samples" Biol. Trace Element Res. Vol.71 -72 (1999) 77
- 3) A. Sugimoto, K. Ishii "Elemental analysis of cellular samples by in-air micro-PIXE" Nucl. Instr. and Meth. B181 (2001) 448-453
- 4) A. Tanaka, K. Ishii "In-air micro-PIXE analysis of tissue samples" Int. J. PIXE, 12 (Nos.3&4), (2002) 79-83
- 5) Jouvin, M.H., Numerof, R.P., KINET, J.P. "Signal transduction through the conserved motifs of the high affinity IgE receptor Fc epsilon RI" Semin. Immunol., 7, (1995) 29-35
- 6) S. Raison, I. Gillot, C. Choine "Ca increase in secretory granules of stimulated mast cells" Cell Calcium, 26(3/4), (1999) 111-119

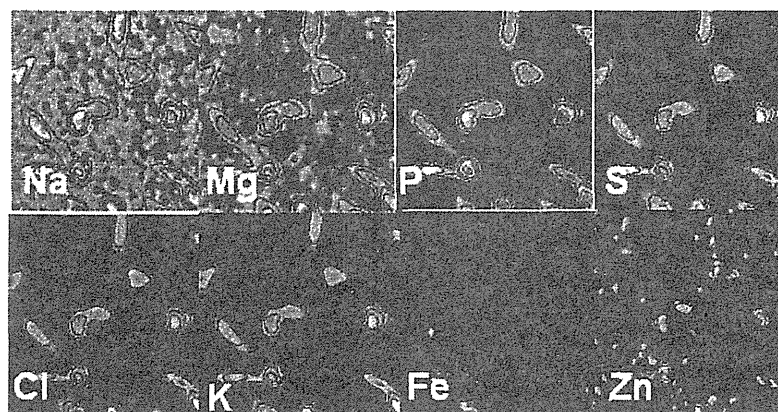


Fig.1 Elemental mapping of control RBL-2H3 cells

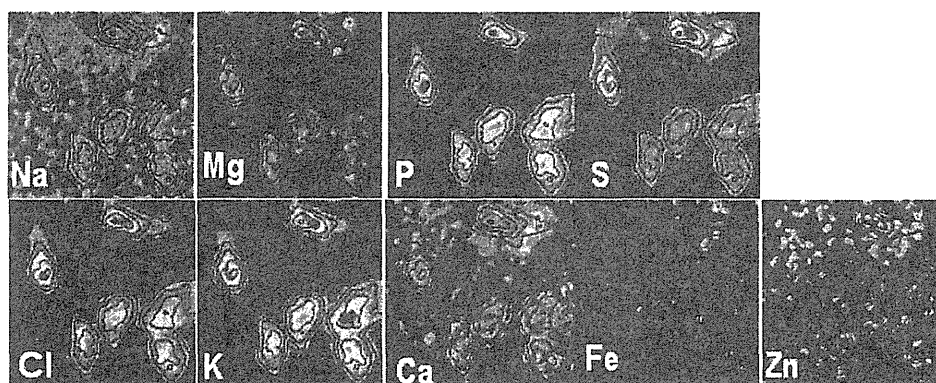


Fig.2 Elemental mapping of stimulated RBL-2H3 cell

7.13 Imaging of Biological Samples using Proton-induced Characteristic X-ray Emission

Y.Oguri*, S.Iwatani*, J.Kaneko*, J.Hasegawa*, H.Fukuda*, M.Ogawa*,
Y.Saitoh** and T.Sakai**

Research Laboratory for Nuclear Reactors, Tokyo Institute of Technology*
Advanced Radiation Technology Center, JAERI**

1. Introduction

In conventional X-ray radiography, the image contrast of a multi-component sample is obtained simply by the difference in absorption properties between the components. To realize a higher contrast, we should optimize the wavelength, or the energy of the X-ray so that the difference in the absorption coefficients can be as large as possible¹⁾.

If the X-ray energy is monochromatic, and slightly above the absorption edge of the element of interest, we obtain very high attenuation by this element, and therefore very high contrast in the transmission image. However, as long as an ordinary X-ray tube is used, the energy spectrum of the X-ray is degraded by a continuum owing to the high Bremsstrahlung background.

On the other hand, when a solid target is bombarded with MeV protons, inner-shell ionization of the target atoms is induced and monochromatic characteristic X-rays are emitted²⁾. In this case, the energy of the secondary electrons produced in the target is much lower than that in electron beams in X-ray tubes. Therefore the background continuum under the characteristic X-ray peaks is dramatically reduced.

In this note, we investigate the scientific feasibility of using these monochromatic emissions to improve the quality of X-ray radiography of small biological samples. Performance of MeV proton microprobes as an excitation source is discussed.

2. Experimental

The experimental setup at the JAERI proton microprobe facility^{3),4)} is illustrated in Fig.1. The sample was a dried small fish (fry of Japanese sand lance, *Ammodytes personatus*). The distance between the X-ray source and the sample was 2 mm. A 100- μm -thick Mylar foil was used to support the sample. To obtain a magnified transmission image, the image plane was put 34 mm behind the sample. The beam energy was 2.6 MeV. The size of the primary proton beam was $\approx 10\ \mu\text{m}$ (horizontal) $\times \approx 5\ \mu\text{m}$ (vertical). The beam intensity was $\approx 10\ \text{nA}$. The energy spectrum and irradiation dose of the X-rays were monitored by a Si(Li) detector. To clearly observe the bones in this thin sample, the attenuation of the X-rays by Ca should be as large as possible. We used ^{22}Ti as the target in this measurement, since the energy of the Ti- K_{α} X-ray (4.51 keV) is just above the K-absorption edge of Ca at 4.04 keV⁵⁾. Also a radiogram was taken using 8.05-keV K_{α} X-rays emitted by a ^{29}Cu target for comparison.

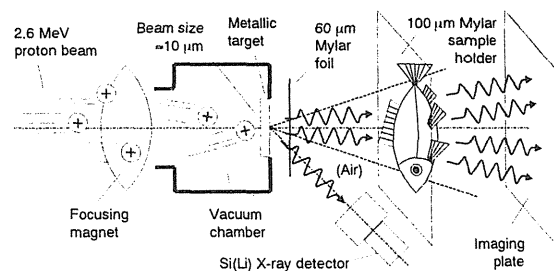


Fig.1 Setup of the experiments. The sample was attached to the imaging plate-side of the sample holder.

In this experimental geometry the metallic targets work not only as an X-ray source but also as a vacuum window. Thanks to this configuration we could put the sample very near to the source although the sample was kept in the atmosphere. To eliminate self-absorption of the X-rays by the target layer we used metallic foils as thin as possible. We used Ti and Cu foils with a thickness of 20 μm . Nevertheless the X-ray intensity was reduced by a factor of 30-50% due to the attenuation in the foil. LX rays from these metallic targets were almost completely attenuated by self-absorption.

In this geometry the sum of the mass thickness of the target (metallic foil, 20 μm), air (2 mm) and the sample holder (Mylar, 100 μm) in front of the sample was not enough to stop the incident protons. To protect the sample from the damage due to the proton irradiation, we put a 60- μm Mylar foil additionally behind the metallic foil.

The radiograms were recorded by an imaging plate with a size of 30 mm \times 50 mm. We used an imaging plate readout system (Combix 2000, Crossfield corp.) dedicated to dental use. Exposure time was $\approx 10^2$ - 10^3 sec, depending on the X-ray yield and the sensitivity of the imaging plate.

3. Results and discussion

Figure 2 shows an example of X-ray spectra obtained by proton irradiation onto the Ti and Cu targets. We see that the Ti- K_{α} peak is located at the energy where the difference in the absorption between bones and soft tissues is very large. On the other hand, peaks of Cu-KX-rays are far away from the K-absorption edge of Ca in bones.

Not only K_{α} emissions but also small peaks of K_{β} lines are observable. Nevertheless we do not see background continua due to Bremsstrahlung.

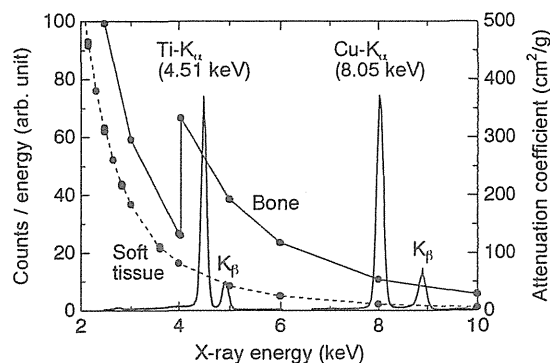


Fig.2 Measured X-ray spectra for Ti and Cu targets. Also attenuation coefficients of bones and soft tissues are plotted.

Figure 3(a) shows a transmission image of the fish sample obtained by 4.51-keV photons emitted from the Ti target. Figure 3(b) shows a picture taken by 8.05-keV photons from the Cu target. The exposure time was 3000 sec for each sample. The radiation dose was 0.36 mSv for the Ti target and 0.18 mSv for the Cu target. As expected, the fine structure of the very thin caudal fin ($< 100 \mu\text{m}$) is more highly contrasted by 4.51-keV photons than by 8.05-keV photons. This result is due to the strong absorption at 4.51-keV by Ca in the bones. The spatial resolution of the picture in this case was $\approx 20 \mu\text{m}$.

In the present experimental geometry, unsharpness of the radiographs is determined mainly by the size of the penumbra due to the finite source size. The penumbra size P on the imaging plate is given by

$$P = (M - 1)r_s. \quad (1)$$

In the formula above, r_s denotes the source size which is roughly equal to the size of the primary proton beam. The parameter M is the magnification defined by

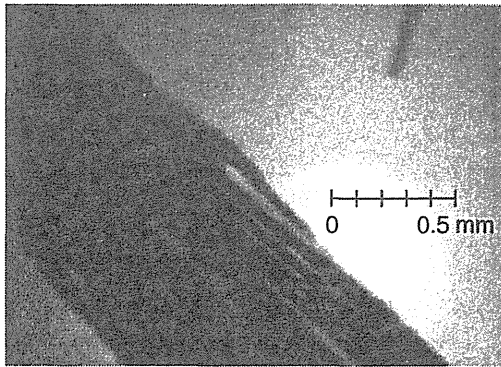
$$M \equiv \frac{l_1 + l_2}{l_1}, \quad (2)$$

where l_1 and l_2 denote the source-object and the object-image distance, respectively. Using these parameters, the resolution of the image in actual

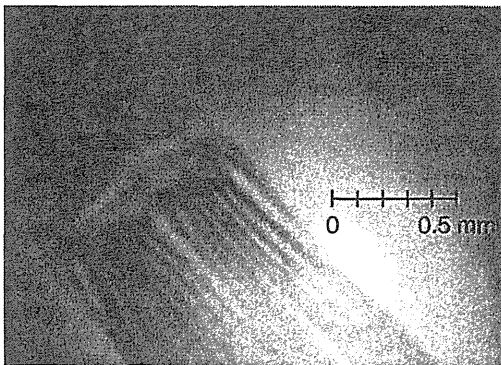
size δx is evaluated by

$$\delta x = \frac{P}{M} = \left(\frac{M-1}{M} \right) r_s. \quad (3)$$

From the equation above, the theoretical resolution of the images obtained by the microbeam was calculated to be $\approx 10 \mu\text{m}$. This expectation is consistent with the image qualities seen in Fig.3.



(a)



(b)

Fig.3 Radiograph of the fish sample taken by (a) 4.51-keV (Ti- K_α) and (b) 8.05-keV (Cu- K_α) photons.

4. Conclusions

We have experimentally demonstrated the application of monochromatic X-rays produced by MeV protons to high-contrast X-ray imaging. Adjustment of the photon energy by changing the metallic target enabled us to use strong

attenuation slightly above the K-absorption edge of the element of interest.

We have found that a metallic target bombarded by a proton microbeam is potentially a useful point-like monochromatic X-ray source, which has sizes as small as those of recent sources with cold cathodes⁶⁾. Ti- K_α X-rays produced by a proton microprobe might be a powerful tool for observation of bones in small biological samples thinner than $100 \mu\text{m}$.

Owing to the low intensity of the proton-induced X-ray emission, however, one needs so far $\approx 10^2$ - 10^3 seconds to take a picture with an acceptable quality. Despite such problems, the performance of the method presented in this paper is already enough for many kinds of high-resolution, high-contrast radiography of thin biological samples, if long exposure time is permitted.

References

- 1) M.Skarpathiotakis, M.J.Jaffe, A.K.Bloomquist, D.Rico, S.Muller, A.Rick and F.Jeunehomme, *Med. Phys.* 29 (2002) 2419-2426.
- 2) S.A.E.Johansson and T.B.Johansson, *Nucl. Instr. and Meth.* 137 (1976) 473-516.
- 3) T.Sakai, T.Kamiya, M.Oikawa, T.Sato, A.Tanaka and K.Ishii, *Nucl. Instr. and Meth. B* 190 (2002) 271-275.
- 4) H.Watanabe and Y.Sudo, *Nucl. Instr. and Meth. B* 210 (2003) 1-5.
- 5) J.H.Hubbell and S.M.Seltzer, Technical Report NISTIR 5632, NIST, Gaithersburg, MD 20899 (1995).
- 6) T.Matsumoto and H.Mimura, *Appl Phys. Lett.* 82 (2003) 1637-1639.

This is a blank page.

8. Radiation Shielding for Accelerator Facilities

8.1	Measurement of G-value for Nitric Acid Production	289
	Y. Kanda, Y. Oki, T. Iida, S. Yokoyama, K. Sato, H. Noguchi and Su. Tanaka	
8.2	Measurements of Absorbed Dose Distributions in Phantoms Irradiated by 40 and 75 MeV Quasi-monoenergetic Neutrons	291
	S. Tsuda, Y. Nakane, Y. Yamaguchi and Su. Tanaka	
8.3	Development of Track Detector Type Personal Dosimeter for High-energy Neutrons	293
	K. Oda, Y. Imasaka, T. Yamauchi, Y. Nakane, A. Endo and Y. Yamaguchi	

This is a blank page.

8.1 Measurement of G-value for Nitric Acid Production

Y. Kanda*, Y. Oki**, T. Iida***, S. Yokoyama****, K. Sato****,
H. Noguchi**** and Su. Tanaka*****

Radiation Science Center, High Energy Accelerator Research Organization*

Research Reactor Institute, Kyoto University**

Graduate School of Engineering, Nagoya University***

Department of Health Physics, JAERI****

Advanced Radiation Technology Center, JAERI*****

1. Introduction

A broad range of frontier sciences is requesting high power proton accelerators. The Japan Hadron Facility project,¹⁾ referred to as the "J-PARC" (Japan Proton Accelerator Research Complex) project, is progressing, with an anticipated first beam from the Linac in 2006, aiming to further the frontier in accelerator science. The project is a complex of very high-intensity proton machines, providing various secondary particle beams of more than one order higher intensity compared with those at any existing accelerator. The machine can provide Mega watt-class high-power proton beams at both 3 GeV and 50 GeV. Such a high-intensity proton accelerator gives rise to very strong radiation environments, leading to an abundant production of radiolytic gases and radioactive gases from the atmospheric air as well as the intense activation of accelerator components. Therefore, from the viewpoint of machine maintenance, damages of various components, not only by strong radiation, but also by the corrosion with nitric acid is becoming an important problem, because nitric acid is a principal radiolytic nitrogen compound produced in a large quantity,²⁻⁴⁾ and is a strong acid that acts as an oxidizing agent. Hence, with an increase of the power and energy of accelerators, information concerning the production of nitric acid becomes more significant for the protection of machine parts. Corrosion caused by nitric acid was observed on the lead shielding around magnets and

aluminum bellows at a high-energy electron positron storage ring.⁵⁾

The formation of radiolytic products can be commonly characterized by the so-called G-values, i.e. the number of molecules formed per 100 eV of radiation energy absorbed. In this work, the G-value for nitric acid formation was measured by the proton irradiation.

2. Experimental

The experiment was carried out at Takasaki Ion Accelerators for Advanced Radiation Application (TIARA) of JAERI. A vacuumed irradiation chamber was installed in the HB beam line of an AVF cyclotron as shown in Fig.1. An atmospheric air closed in a pyrex glass vessel was irradiated with 50 MeV protons. Figure 2 shows the glass vessel. The size of the vessel was 50 mm in diameter and 70 mm in length. The vessel was placed in the irradiation chamber and set on the proton beam axis. The irradiation was done with a proton beam of 2 nA for 5min and 10 min.

After the irradiation, the produced nitric acid was extracted by washing the inside of the vessel with 10 ml of 0.05 M NaOH solution. The determination of nitrate in the extracts was performed by a flow-injection analysis method based on the reduction of nitrate to NO with hydrazine/ascorbic acid and the successive detection of NO by a chemiluminescence NOx monitor.⁶⁾ This method permits a highly sensitive measurement, and the lowest determinable amount was 2×10^{-2} μg .

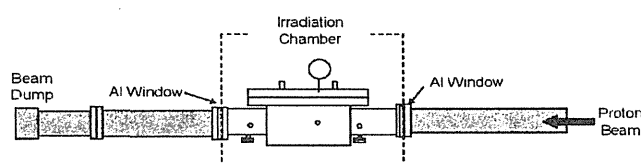


Fig.1 Irradiation chamber

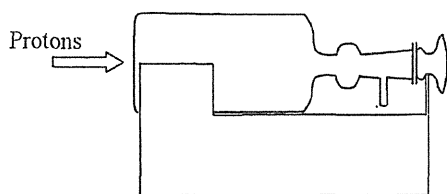


Fig.2 Glass vessel for air irradiation

The beam size was measured with an aluminum activation detector based on measuring the induced radioactivity. An aluminum foil of $100 \times 100 \text{ mm}^2$ size was placed just in front of the irradiation vessel and was exposed for 5 min. The foil was cut concentrically at some intervals from the beam axis and the ^{24}Na yields in the aluminum pieces were measured. The proton incident upon the irradiation vessel were calculated to be 90 % of the protons injected into the irradiation chamber.

3. Results and Discussion

The radiolytic-yield value, G-value, is defined as the number of reaction products per 100 eV of ionizing radiation absorbed by the system. Then, to evaluate the G-value for nitric acid production, it is necessary to know the number of nitric acid molecule produced and the amount of energy deposited in the irradiation vessel.

The number of the produced nitric acid molecule was obtained experimentally. On the other hand, the amount of the deposited energy was obtained by the calculation using the values of stopping power,⁷⁾ because the stopping power of a material is defined as the average energy loss per unit path length which charged particles suffer when traversing the material.

Before the 50 MeV protons from AVF cyclotron irradiate the air in the vessel, they loss their energy through an aluminum window (3 mm thick) and the pyrex glass vessel (2.5 mm thick). The energy losses were calculated as follow:

$$E_{\text{LOSS}} = SP \times \sigma \times L$$

SP: stopping power ($\text{MeV cm}^2/\text{g}$)

σ : density (g/cm^3)

L: thickness (cm)

The total of energy losses was calculated to be 13.6 MeV. Consequently, the air in the vessel was irradiated by 36.4 MeV protons.

The number of the produced nitric acid molecule (N) was calculated by the following

equation.

$$N = n \times f \times SP \times \sigma \times L \times G/100$$

n: number of proton (beam current \times irradiation time, t)

f: fraction of protons incident upon the vessel

SP: stopping power of 36.4 MeV proton in air

σ : density of air

L: length of air irradiated by protons

G: G-value for nitric acid production

In this experiment, the calculated number of nitric acid molecule was $8 \times 10^{14} \times t \times G$. And the measured number of nitric acid molecule was 4.7×10^{15} for the 5 min irradiation and 8.9×10^{15} for the 10 min irradiation. Consequently, the G-value was calculated to be 1.2 and 1.1.

Less and Swallow²⁾ have continuously irradiated air closed in flask for long periods of time with ^{60}Co γ -rays. They reported that the average G-value for nitric acid production is 1.5. We⁸⁾ have reported the G-value for ozone production to be 6.4 by the irradiation of atmospheric air with high-energy protons at the 12 GeV proton synchrotron. And the yield of nitric acid has determined to be 0.19-times smaller than that of ozone.⁴⁾ These results leads to the G-value of 1.2 for nitric acid production.

The G-values for nitric acid production obtained in this experiment are in reasonable agreement with these values.

References

- 1) Y. Yamazaki et al., Proc. 1999 Part. Accel. Conf., THDL1 (1999).
- 2) L. N. Less, A. J. Swallow, Nucleonics, 22 (1964) 58.
- 3) Y. Kanda, M. Taira, K. Kondo, T. Miura, Health Phys., 56 (1989) 953.
- 4) Y. Kanda, T. Momose, M. Taira, Radiat. Phys. Chem., 48 (1996) 49.
- 5) T. Momose, H. Ishimaru, J. Vac. Sci. Technol., A9 (1991) 2149.
- 6) Y. Kanda, M. Taira, Anal. Sci., 19 (2003) 695.
- 7) ICRU report 49 "Stopping Powers and Ranges for Protons and Alpha Particles", Int. Comm. Rad. Units and Measurement.
- 8) Y. Kanda, Y. Oki, A. Endo, M. Numajiri, K. Kondo, J. Radioanal. Nucl. Chem., 247 (2001) 25.

8.2 Measurements of Absorbed Dose Distributions in Phantoms Irradiated by 40 and 75 MeV Quasi-monoenergetic Neutrons

S. Tsuda*, Y. Nakane**, Y. Yamaguchi* and Su. Tanaka***

Department of Health Physics, JAERI*

Center for Proton Accelerator Facilities, JAERI**

Advanced Radiation Technology Center, JAERI ***

1. Introduction

Dose assessments for high energy radiation are mainly performed using Monte Carlo simulation codes. In the calculations of doses, the methods of particle transport and energy deposition are different among the kinds of simulation codes. For this reason, the calculated doses are also different among the simulation codes used.

For the purpose of the verification of absorbed dose calculations by Monte Carlo simulation codes in the neutron energy range of several 10s MeV, measurements of absorbed doses were carried out in slabs made of main elements in human body, using the quasi-monoenergetic neutrons of 40 and 75 MeV in TIARA.

2. Experiments

The experiments were performed using the quasi-monoenergetic neutron sources at the LC beam line. The generated neutrons by the ${}^7\text{Li}(p,n){}^7\text{Be}$ reaction are transported through an iron collimator of 11-cm diameter to the experimental room. Figure 1 shows the spectra of 40 and 75 MeV quasi-monoenergetic neutrons¹⁾. Two kinds of slabs were used for the absorbed dose measurements, a pure graphite slab and a slab made of a soft tissue substitute²⁾. The graphite slab was selected because carbon

atom is one of the main elements in human body. In the measurements, a tissue equivalent ionization chamber and a tissue equivalent proportional counter (TEPC) were used, the both of which are manufactured by Far West Technology, INC. TEPC was also used for the measurement of lineal energy distributions³⁾ in the slabs.

3. Calculations

The latest MCNPX⁴⁾ version 2.4.0 and the PHITS⁵⁾ code version 1.7.2 were selected and used in the absorbed dose calculations. MCNPX is a general purpose Monte Carlo radiation transport code that has been developed at LANL. PHITS is an appropriate Monte Carlo simulation code to calculate doses, since it can simulate the transport of neutrons and all the charged particles generated in slabs.

4. Results and Discussion

In Fig.2 and Fig.3, measured absorbed doses for 40 MeV neutrons are presented in slabs made of graphite and the soft tissue substitute, along with the calculated ones. In the case of measurements in graphite slab, the calculated results by the MCNPX and the PHITS codes agree with the measured ones at least within 15 % uncertainty for neutrons of 40 MeV.

Figure 4 shows the absorbed dose distribution in the slab made of the soft tissue substitute. The calculated absorbed doses agree with the measured ones within 20 % uncertainty in the whole region in the slab, in the both cases of the MCNPX and PHITS calculations. It is found that charged particle transport calculations should be performed in the neutron energy range of several 10s MeV, since absorbed doses can be overestimated in the case of the calculations using kerma approximation⁶⁾.

Figure 5 shows the measured lineal energy distributions in the slab made of graphite for the 75 MeV neutron source. The contribution of heavy ions was presented in the lineal energy range over 100 keV/ μm in the result for the

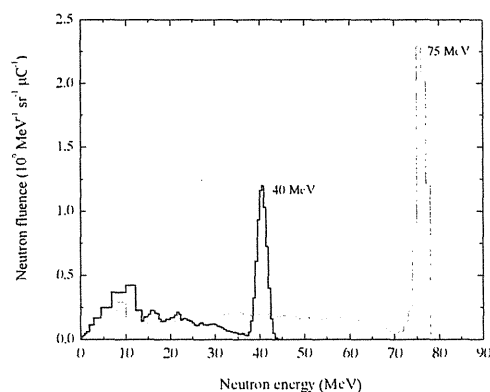


Fig. 1 The spectra of 40 and 75 MeV quasi-monoenergetic neutron sources in TIARA.

2-cm depth case. In the case of the measurement on the surface of the slab, it is found that protons are dominant in the range near 10 keV/ μ m. These data will be available for the verification of the detailed transport calculation of charged particles generated in slabs.

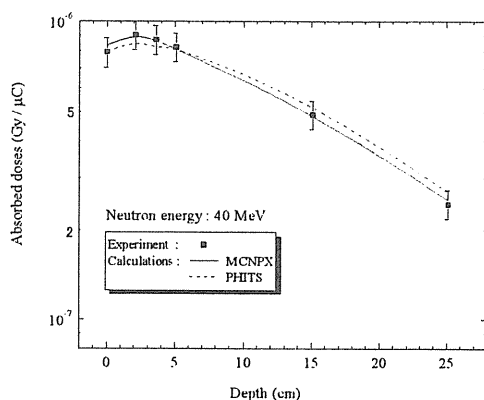


Fig. 2 Absorbed dose distributions for 40 MeV quasi-monoenergetic neutrons in a slab made of graphite.

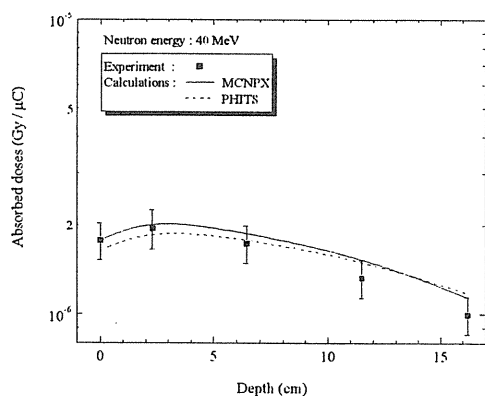


Fig. 3 Absorbed dose distributions for 40 MeV quasi-monoenergetic neutrons in a slab made of a soft tissue substitute.

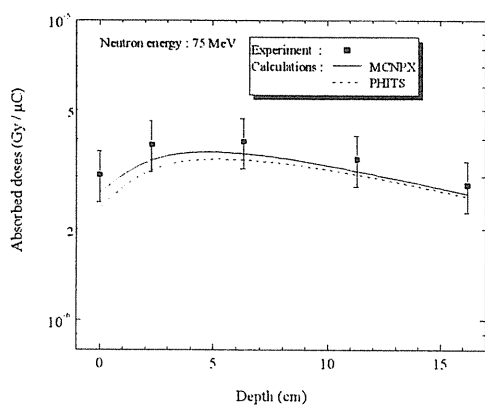


Fig. 4 Absorbed dose distributions for 75 MeV quasi-monoenergetic neutrons in a slab made of a soft tissue substitute.

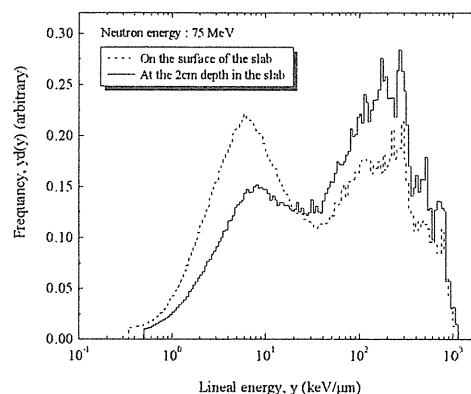


Fig. 5 Lineal energy distributions for 75 MeV quasi-monoenergetic neutrons in the slab made of graphite.

5. Conclusion

Absorbed doses in a graphite slab and a slab made of a soft tissue substitute were measured using the 40 and 75 MeV quasi-monoenergetic neutron sources in TIARA. It is found that the calculated absorbed doses by MCNPX and PHITS agree well with the measured ones, and there is no large difference in the calculated absorbed doses by the Monte Carlo simulation codes. The transport calculation of charged particles is needed in the case of the absorbed dose calculations for neutrons of several 10s MeV.

For more detailed verification of absorbed dose calculations by the Monte Carlo simulation codes, energy spectra of secondary charged particles in slabs will be calculated and compared with the measured ones in the near future.

References

- 1) M. Baba, Y. Nauchi, T. Iwasaki, T. Kiyosumi, M. Yoshioka, S. Matsuyama, N. Hiraoka, T. Nakamura, Su. Tanaka, S. Meigo, H. Nakashima, Sh. Tanaka and N. Nakao, Nucl. Instrum. Methods Phys. Res. A 428 (1999) 454-465.
- 2) S. Tsuda, A. Endo and Y. Yamaguchi, J. Nucl. Sci. Technol., 40 (2003) 1027-1031.
- 3) ICRU, ICRU Report 36 (1983).
- 4) LANL, LA-CP-02-408 (2002).
- 5) H. Iwase, K. Niita and K. Nakamura, J. Nucl. Sci. Technol., 39 (2002) 1142-1151.
- 6) Y. Nakane, JAERI-Research 2003-003 (2000).

8.3 Development of Track Detector Type Personal Dosimeter for High-energy Neutrons

K. Oda*, Y. Imasaka*, T. Yamauchi*, Y. Nakane**, A. Endo** and Y. Yamaguchi***

Department of Environmental Energy Science, Kobe University*,

Center for Neutron Science, JAERI**, Department of Health Physics, JAERI***

1. Introduction

A great number of accelerator facilities for high-energy, intense proton beam have already been in steady operation, and are in construction or planning in many countries. In Japan a collaborative project of JAERI and KEK, called J-PARK is now in progress. Such a proton beam eventually generates high-energy neutrons in slowing down or stopping in a material. These high-energy neutrons are hard to be detected, because the efficiency of existing monitors and dosimeters becomes lower. Hence, it is very important to monitor them correctly, in other words, to establish a countermeasure, for a radiation protection purpose.¹⁾

It has already been pointed out that the prevailing PNTD (Plastic Nuclear Track Detector) such as CR-39 detector has less sensitivity to high-energy neutrons because of a difficulty in registering energetic proton recoils.²⁻⁴⁾ The use of the detector without any corrections would bring about a serious underestimate of the radiation dose and dose rate. Thus, the authors started to develop an advance technique for more efficient detection of high-energy neutrons. The experimental studies require a well-defined and clean neutron source, such as TIARA (Takasaki Ion Accelerators for Advanced Radiation Application) facility, JAERI. In order to increase the detection efficiency, it is necessary to make two major improvements; one is to find a most sensitive PNTD element, and the other to sensitize it with an appropriate radiator supplying charged

particles to PNTD.

In the previous experiments⁵⁻⁸⁾, we checked the performance of three types of PNTDs; "BARYOTRAK" of pure CR-39 plastic, "TD-1" of an improved-type CR-39 and "TNF-1" of a co-polymer based on CR-39, which were made by Fukuvi Chemical Co., Ltd., Japan. From a comparison among them in relative efficiency for 65-MeV neutron detection and in optical property after chemical etching, "TD-1" was chosen as a promising element, which is CR-39 plastic containing a small amount of anti-oxydant. As to the radiator, we investigated the effect of four types of radiator materials; polyethylene (CH₂), deuterized dotriacontane (C₃₂D₆₆), lithium fluoride (LiF) and graphite (C). It was found that the increased sensitivity of the deuterized material exceeded that of CH₂ for a relatively thin radiator of the order of a few hundreds of mg/cm², and that other materials of LiF and C worked unsatisfactorily.

We have proceeded the study on high-energy neutron dosimetry to the next step. It is the purpose of this report to confirm the effect for a radiator thicker than g/cm², comparable with the maximum range of recoil particles. A theoretical approach was also tried to support the experimental results.

2. Experimental Results and Discussion

A neutron irradiation experiment was carried out at TIARA, where quasi-monoenergetic neutrons were generated by bombarding a lithium target with an accelerated proton beam.

These neutrons were guided to an irradiation room through 220-cm thick iron collimator⁹⁾, and then hit TD-1 detectors.

We have searched a deuterized material appropriate for radiator. A dotriacontane, $C_{32}D_{66}$ is one of candidates but too expensive for preparing a thick radiator of the order of g/cm^2 . So, we utilized heavy water in this experiment, which was gelled by adding 1% agarose.

After neutron irradiation, TD-1 detectors were chemically etched in a stirred 7M NaOH solution at 70 °C. The number of etch-pits was counted with a semi-automated system consisting of an optical microscope, image processing system and personal computer.

The results were summarized in Fig. 1, where the incremental etch-pit density was plotted against the radiator thickness. For thinner radiators below 2 g/cm^2 , D_2O radiator dominates H_2O .

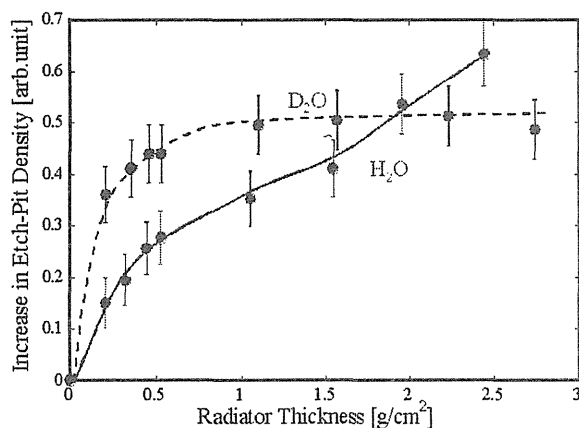


Fig. 1. Measured pit density as a function of the radiator thickness for 65-MeV quasi-monoenergetic neutrons.

3. Numerical Calculations of Radiator Effects

The etch-pit formation in PNTD exposed to fast neutrons takes place in two steps; production of secondary charged particles through neutron interactions with constituent atoms in PNTD and radiator materials, and visualization of their latent tracks by the chemical etching. The overall detection efficiency is the sum of two components of the

intrinsic efficiency and the enhancement by the radiator, which are distinguished by the position of charged particle production, *i.e.* inside or outside the PNTD. It is well known that the latter dominates for neutron energies higher than several hundreds of keV.²⁻⁴⁾ The radiator effect, increase in the efficiency by a radiator, is defined here as the number of charged particles per incident neutron, which are generated in the radiator, reach PNTD and are observed as etch-pits. It is expressed by the following formula of double integral of the interaction yield with respect to the solid angle, Ω and the depth in the radiator, z :

$$\varepsilon = N \iint \frac{d\sigma}{d\Omega} d\Omega dz, \quad (1)$$

where N is the number density of atomic nuclei interacting with neutron and σ is the cross section for the interaction.

The integral range in eq. (1) should be limited by two major conditions characteristic of chemically etched PNTDs. One is so-called critical angle condition, by which inclined latent tracks are eliminated. The other is related with recognition of small etch-pits with an optical microscope and image processing system, which reflects on the reduction of z -integral range.

An example of the results of numerical calculations of eq. (1) is shown in Fig. 2 by a dotted line, where enhancement in detection efficiency is shown as a function of radiator thickness for completely mono-energetic 65 MeV neutrons. The measured dependence on the thickness, however, is a convex shape differently from a concave pattern for monoenergetic neutrons shown in Fig. 1.

4. Discussion

One of major reasons of this discrepancy is considered to be a contamination of lower energy neutrons in a quasi-monoenergetic field. An exact energy spectrum has already been

measured by Baba et al.⁹⁾ The distribution was divided, for simplicity, into several parts, and the contribution of each component was summed up by weighting the fractional portion. A solid line in Fig.2 shows the result obtained in this procedure. It is found that the increase pattern is sensitively affected by lower energy neutrons.

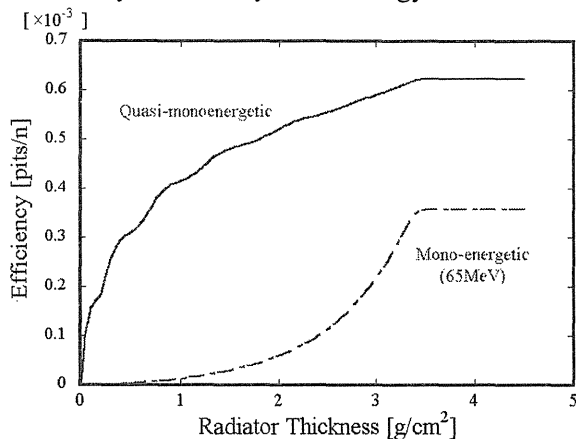


Fig. 2 Radiator effect for monoenergetic and quasi-monoenergetic neutrons.

As was described above, the response of PNTD with a thick radiator to quasi-monoenergetic neutrons has been discussed both theoretically and experimentally. The thickness, however, is one of the critical problems for practical applications to personal dosimetry; namely it is appropriate to reduce the weight of the radiator for convenience. Another important problem still remains to adjust the energy dependence of the overall sensitivity to that of the conversion factor for personal dose equivalent at a depth of 10 mm, $H_p(10)$. We expect a two-layer type radiator²⁾ is one of promising techniques to control the energy dependence.

5. Conclusion

As part of a study on personal dosimetry of high-energy neutrons, a sensitization by

radiators was discussed. The increase in the sensitivity has been obtained experimentally for a thick radiator of the order of a few g/cm^2 . It was confirmed from calculated results that the thickness dependence of the radiator effect was modified sensitively by contamination of lower energy neutrons. A deuterized material or a combination of two materials is expected to be a special radiator for high-energy neutrons.

References

- 1) Y. Yamaguchi and H. Hirayama, *J. Nucl. Sci. Technol.*, Suppl. 4 (2004) 498-501.
- 2) K. Oda, M. Ito, H. Yoneda, H. Miyake, J. Yamamoto and T. Tsuruta, *Nucl. Instrum. Meth. Phys. Res. B* **61** (1991) 302-308.
- 3) D. Hermsdorf, R. Bretschneider, B. Dorschel and J. Henniger, *Radiat. Meas.* **31** (1999) 431-436.
- 4) R. J. Tanner, D. T. Bartlett and L. G. Hager, *Radiat. Meas.* **34** (2001) 457-461.
- 5) K. Oda, H. Ichijo, N. Miyawaki, T. Yamauchi and Y. Nakane, *Radiat. Meas.* **34** (2001) 171-175.
- 6) K. Oda, Y. Saito, N. Miyawaki, T. Yamauchi, A. El-Rahmany, Y. Nakane and Y. Yamaguchi, *Radiat. Prot. Dosim.* **101** (2002) 569-572.
- 7) K. Oda, Y. Imasaka, K. Tsukahara, T. Yamauchi, Y. Nakane and Y. Yamaguchi, *Radiat. Meas.* **36** (2003) 119-124.
- 8) K. Oda, Y. Imasaka, T. Yamauchi, Y. Nakane, A. Endo and Y. Yamaguchi, *J. Nucl. Sci. Technol.*, Suppl.4 (2004) 514-517.
- 9) M. Baba, Y. Nauchi, T. Iwasaki, T. Kiyosumi, S. Yoshioka, N. Hirakawa, T. Nakamura, Su. Tanaka, S. Meigo, H. Nakashoma, Sh. Tanaka, and N. Nakao, *Nucl. Instrum. Meth. Phys. Res. A* **428** (1999) 454-465.

This is a blank page.

9. Accelerator Technology/TIARA General

9.1	Construction of Intense Positron Source Based on AVF Cyclotron for High Brightness Positron Beam(II)	299
	M. Maekawa, A. Kawasuso, F. Kashima and Z. Q. Chen	
9.2	Measurement of Carbon Cluster Ion passing through Carbon Thin Foil	302
	Y. Saitoh, A. Chiba and K. Arakawa	
9.3	TOF Mass Spectrometry of Secondary Ions from HOPG Target Bombarded by Fast Cluster Ion Beams	304
	H. Shibata, A. Itoh, H. Tsuchida, Y. Saitoh, A. Chiba, K. Arakawa, Y. Ohara and K. Narumi	
9.4	The Effect of Ion Doping on Ionic Conduction of Sol-gel Phosphosilicate Glasses(II)	307
	S. Ishiyama, S. Kitazawa, S. Yamamoto and M. Asano	
9.5	Present Status of JAERI AVF Cyclotron System	310
	Y. Nakamura, T. Nara, T. Agematsu, I. Ishibori, S. Kurashima, K. Yoshida, M. Fukuda, S. Okumura, N. Miyawaki, S. Tajima, K. Akaiwa, To. Yoshida, S. Ishiro, Y. Arakawa, Tu. Yoshida, S. Kanou, A. Ihara and K. Takano	
9.6	Beam Development for Flat-top Acceleration in the JAERI AVF Cyclotron (II)	313
	S. Kurashima, M. Fukuda, S. Okumura, N. Miyawaki, T. Nara, T. Agematsu, I. Ishibori, K. Yoshida, Y. Nakamura and K. Arakawa	
9.7	Design of a Small ECR Ion Source with Permanent Magnets for Cyclotron	316
	K. Yoshida, T. Nara, Y. Saitoh and W. Yokota	
9.8	Installation of Cooling Panel for Cyclotron Stabilization	318
	Y. Nakamura, K. Takano, To. Yoshida and Y. Arakawa	
9.9	Inverter Chain Driving System for the 3MV Tandem Accelerator	321
	K. Mizuhashi, A. Chiba, M. Ishii, T. Kitano, S. Kanai and S. Tajima	
9.10	Development of Beam Current Stabilization System using Wire Type Beam Attenuator	324
	K. Ohkoshi, A. Chiba, K. Mizuhashi and S. Tajima	
9.11	Automatic Measurement of Beam Energy Spread for JAERI Single-ended Accelerator II	326
	Y. Ishii, A. Chiba, T. Sakai and I. Takada	
9.12	Renewal of Control System for the 3MV Single-ended Accelerator	328
	S. Uno, A. Chiba, T. Takayama, M. Kouka, I. Takada and S. Tajima	

9.13 Beam Chopping System for Cluster T.O.F. Measurement in 3 MV

Tandem Accelerator 330

Y. Saitoh, A. Chiba and K. Mizuhashi

9.1 Construction of Intense Positron Source Based on AVF Cyclotron for High Brightness Positron Beam(II)

M. Maekawa^{*}, A. Kawasuso^{*}, F. Kashima^{**} and Z. Q. Chen^{*}

Advanced Science Research Center, JAERI^{*}

Takasaki Establishment, JAERI^{**}

1. Introduction

Positron beams are being used with increasing success for the study of defects in near surface region of solids. In our research group, slow positron beam apparatus for the depth profiling of defects are developed and used for evaluation of semi-conductor or inorganic materials¹⁾. Moreover, recently we have been developing reflection high-energy positron diffraction (RHEPD) apparatus for the analysis of surface structure of materials²⁾. With these slow positron beam apparatuses, commercial based sealed positron sources are used as positron sources. The machine geometry can be simplified and excellent beam stability can be achieved, however, the beam brightness is not enough for the observation of the transient phenomena on the surface or the small regions in a micrometer range. To break these limitation, we attempt to construct an intense positron source which used the nuclear reaction $^{27}\text{Al}(p,n)^{27}\text{Si}$ for high brightness positron beam production. Comparison with the other large-scale positron sources, such as based on electron LINAC or the nuclear reactor, this method is inferior in absolute beam intensity. However, it is suitable for a high-brightness positron beam production because of easy beam handling due to simple

and compact structure, and stable beam production. Some other positron beam productions based on ion beam are also developed as shown in Table I. The advantages of ^{27}Si production are (i) easy supply of target, (ii) simple structure because of solid target, (iii) short half-life and high safety and (iv) utilizing of proton beam which has comparatively strong intensity.

2. Design of positron production system

Generally, high-brightness beam production requires beam acceleration and focusing by the high-performance lens system. However, the design of such a lens system is greatly depending on the initial conditions of the generated positrons. In this study, we first attempt to clarify the initial condition of positrons using simple beam line.

Figure 1 shows a schematic drawing of positron source. The proton beam from the TIARA AVF cyclotron is irradiated to the high purity aluminum target (99.999% purity, 8 mm diameter), which mounted on the jacket with 5 mm collimator cooled with running water. In this target, positron emitter ^{27}Si (a half-life of 4.3 sec) are produced due to the nuclear reaction $^{27}\text{Al}(p,n)^{27}\text{Si}$. The branching ratio of β^+ decay

Table I Positron Emitters which can be generated by ion beams.

RI	Atomic Reaction	$T_{1/2}$	Branching ratio[%]	Cross section[mb]	Energy(σ_{max})	Number of Positrons [GBq/mA/h]
^{11}C	$^{11}\text{B}(p,n)^{11}\text{C}$	20.3 min	99.8	100-350	4-10MeV	0.222
^{13}N	$^{12}\text{C}(d,n)^{13}\text{N}$	10 min	100	100-250	$\sim 5\text{MeV}$	0.444
^{18}F	$^{18}\text{O}(p,n)^{18}\text{F}$	110 min	96.9	100-300	2-14MeV	2.22
^{27}Si	$^{27}\text{Al}(p,n)^{27}\text{Si}$	4.2 sec	100	40	14-16MeV	9

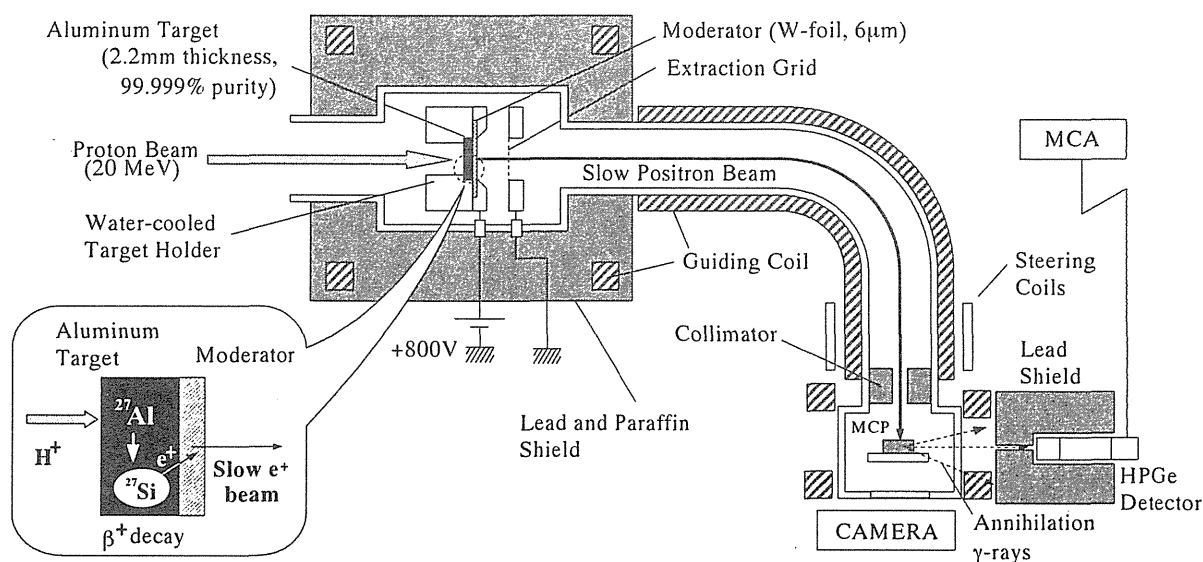


Fig. 1 Schematic of positron production system

of the ^{27}Si is 100 %. The fast positrons emitted from ^{27}Si are thermalized in a polycrystalline tungsten moderator with a thickness of 6 μm . This thickness shows the highest positron re-emission efficiency considering the positron implantation profile emitted from ^{27}Si (~ 3.85 MeV)^{3, 4)}. Slow positrons extracted by a grid electrode are transported to the beam monitor (MCP) by a magnetic guiding field (~ 0.01 T). To suppress fast positrons, secondary electrons, ions and γ -rays coming from the Al target directly, this guiding field is bended to the angle of 90° .

The proton beam energy was set to 20 MeV because the reported maximum cross section of $^{27}\text{Al}(p,n)^{27}\text{Si}$ is 14-16 MeV^{5, 6)}. The maximum range of 20 MeV protons is about 2.2 mm. To avoid direct damage of the moderator by proton irradiation, the thickness of aluminum target is 2.4 mm. The saturated radioactivity of the ^{27}Si for a proton current of 1 μA is evaluated at 9.3 GBq by the IRAC code⁷⁾. This means that the number of generated fast positrons is 9.3×10^9 e^+/s . The expected flux of slow positron beam is $\sim 10^6$ e^+/s if the conversion efficiency of moderator is assumed to be 10^{-4} ⁸⁾. This intensity is still two orders of magnitude higher than that of the conventional positron beam based on sealed positron source.

Above system has been constructed in last year and positron beam production was already confirmed with comparatively good quality¹⁰⁾. However, the estimation of initial conditions of the generated positrons was difficult because the beam was not so focused. In this year the structure of the electrodes around target are improved. To extract more positrons efficiently, the narrow gap distance between the moderator and the extraction grid is adopted (1 mm). In addition, positrons can be extracted from moderator with high perpendicularity. To reduce the beam lost, coils are added for reinforced magnetic guiding field.

3. Results and discussion

The observed positron beam is shown in Fig. 2. The incident proton beam energy and current were 20 MeV and 70 nA, and positron transportation energy was 800 eV. The diameter of incident ion beam was adjusted about 5 mm. The diameter of positron beam was 2.5 mm (FWHM) and 5 mm (tail). This is reflected that the size of the moderator is 5 mm. The beam profile is well-balanced gaussian shape. This means that the beam can be formed without large distortion. With increasing the transportation energy, the position of a beam was shifted due to

the curvature drift without large distortion of beam shape. This means that the slow positron beam generated with this system has the almost same quality as the positron beam from the usual sealed source. Therefore, it is possible to develop existing beam technology into the high brightness positron source.

However, the longer beam transportation is required than that of beam line based on sealed source because of effective elimination of many secondary electrons or ions besides positrons coming from target.

The number of transported positrons was also measured by counting the annihilation gamma rays (511 keV). The proton current dependence of estimated positron beam intensity is shown in

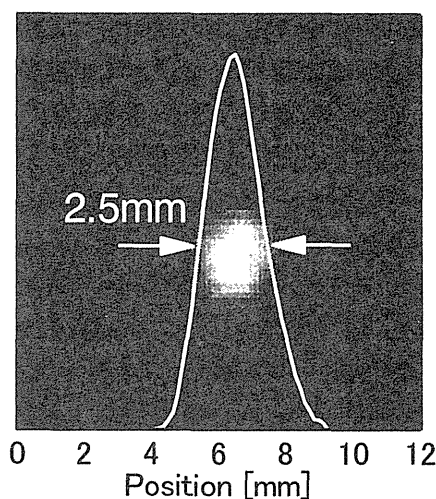


Fig. 2 Positron beam image observed with a MCP with 10mm diameter.

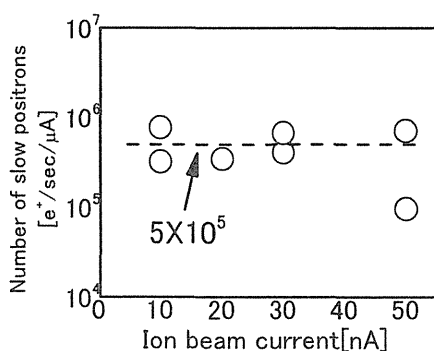


Fig. 3 The number of generated slow positrons per unit proton current.

Fig. 3. The number of positrons per unit proton current showed no changes with incidence ion beam current. Number of slow positron is about 5×10^5 e⁺/s/μA. This is the almost same intensity of the Hirose's report ⁹⁾ and expected from the IRAC simulation. This shows that the positrons can be generated mostly as a design value. The energy end-point of emitted fast positrons from the ²⁷Si (~3.85 MeV) is quite different from that from ²²Na (~0.54 MeV). In that case, however, it is possible that fast positrons can be converted to slow positrons beam with sufficient efficiency using a tungsten moderator with an adequate thickness. This shows that the design method using in this study is a great success for positron beam production based on cyclotron.

This result is promising towards the high-brightness positron beam production using the cyclotron-base intense positron beam.

References

- 1) A. Kawasuso, S. Okada and A. Ichimiya, Nucl. Inst. & Meth. B171 (2000) 219-230.
- 2) M. Maekawa, A. Kawasuso, M. Yoshikawa and H. Itoh, Appl. Surf. Sci. 216 (2003) 365-370.
- 3) A. Vehanen and J. Makinen, Appl. Phys A36 (1985) 97-101.
- 4) W. Brandt and R. Paulin, Phys. Rev. B15 (1977) 2511-2518.
- 5) J. D. Anderson, S. D. Bloom and C. Wong, Phys. Rev. 117 (1966) 177.
- 6) P. M. Racolta, L. Popa-Simil, N. Miron and C.I. Muntele, Nucl. Inst. & Meth. B139 (1998) 461.
- 7) S. Tanaka, M. Hukuda, K. Nishimura, M. Watanabe, N. Yamano, JAERI-Data/Code 97-019 (1997).
- 8) K. G. Lynn et.al., Appl. Phys. Lett. 47 (1985) 239-240.
- 9) M. Hirose, M. Washio and K. Takahashi, Appl. Surf. Sci. 85 (1995) 111.
- 10) M. Maekawa, A. Kawasuso, T. Ishimoto, Z. Q. Chen, TIARA annual report 2003.

9.2 Measurement of Carbon Cluster Ion passing through Carbon Thin Foil

Y. Saitoh*, A. Chiba* and K. Arakawa**

Advanced Radiation Technology Center, JAERI*

Department of Ion-beam-applied Biology, JAERI**

1. Introduction

Recently, interaction of swift cluster ions with solids has gained considerable interest. One expects that the bombarding a material surface simultaneously with constituent atoms of a swift cluster ion result in different phenomena from that individually with a single ion. When cluster ions are injected into a solid, the atomic constituents separate in the first several layers but remain close proximity (preserving the structure) for a certain distance. Therefore the structure of a cluster is the important parameter that governs the physical effects in a surface of a solid.

To investigate a cluster structure, a coulomb explosion imaging¹⁾ (CEI) system was developed and a preliminary

test was carried out using swift carbon clusters passing through a thin foil. And the average charge state of each atom that composed a cluster; which was related with the structure of the cluster²⁾, was also measured.

2. Experiments

Carbon cluster ions (C_n ; $n=1-6$) are accelerated to MeV energy region (1.0 MeV/atom) with the TIARA 3 MV tandem accelerator. The experimental setup is show in Fig.1 and Fig.2. The intensity of cluster beam was reduced to several counts par second by a beam attenuator and a beam chopping system. After passing through the carbon thin foil, the constituent atoms of a cluster explode by coulomb repulsion and are detected with a luminous type MCP,

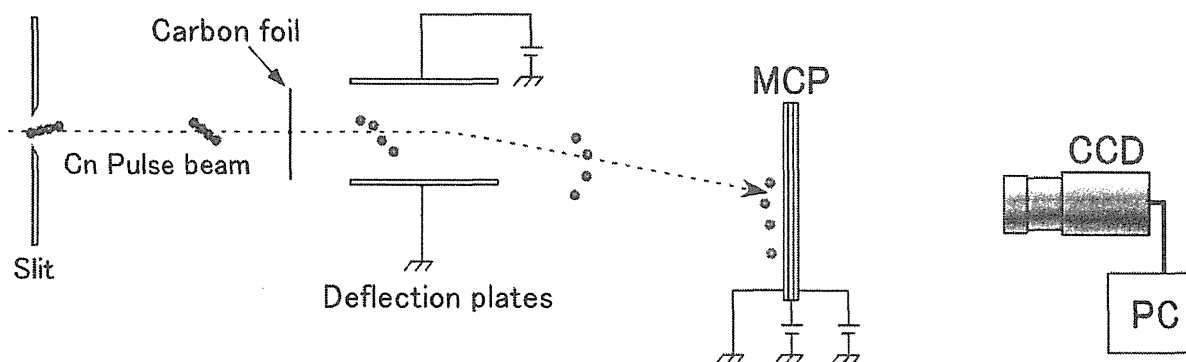


Fig.1. Schematic layout of experimental setup

while the atoms are deflected by the electrostatic deflector placed in front of the MCP. The charge states of the atoms are estimated by the deflected angle. The image data acquired with the CCD camera placed behind the MCP is taken into a PC.

3. Preliminary Results

Figure 2 shows the typical coulomb explosion image of a C_6 cluster observed by a CEI system. In case of a negative carbon cluster ion consisting of less than ten atoms, a chain structure is more stable²⁾. However, both of ring and chain structures are observed.

Figure 3 shows the average charge state of cluster constituents passing through a thin foil normalized by that of a single carbon. The average charge state decreases with increasing of cluster atoms. The result shows the almost same tendency as a calculated theoretical value.³⁾

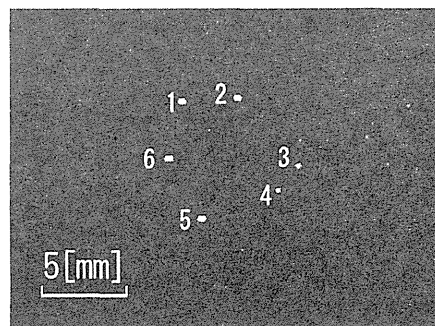


Fig.2 Coulomb explosion image of C_6
(It seems to be a ring structure)

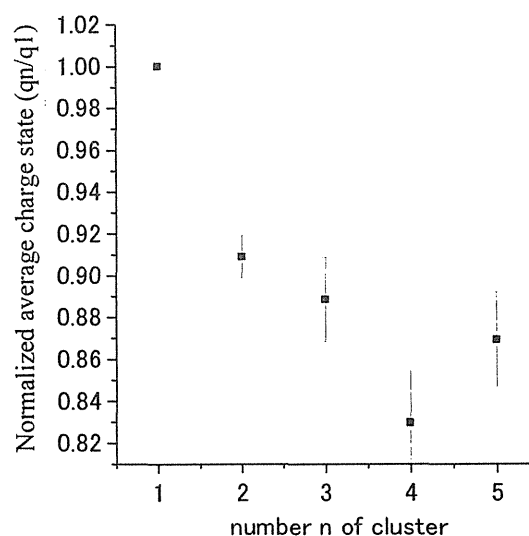


Fig.3 Average charge state of cluster constituents normalized by that of a single carbon (q_n/q_1) vs. number of cluster constituent

References

- 1) Z. Vager, R. Naaman, E. P. Kanter, Science Vol.244, 426 (1989)
- 2) S. Yang, et al. Chem. Phys. Lett. Vol. 144, 431 (1988)
- 3) Toshiaki Kaneko, Phys. Rev. A 66 052901 (2002)

9.3 TOF Mass Spectrometry of Secondary Ions from HOPG Target Bombarded by Fast Cluster Ion Beams

H. Shibata^{*}, A. Itoh^{*}, H. Tsuchida^{*}, Y. Saitoh^{**}, A. Chiba^{**}, K. Arakawa^{***},
Y. Ohara^{**} and K. Narumi^{****}

Graduate School of Engineering, Kyoto University^{*}

Advanced Radiation Technology Center, JAERI^{**}

Department of Ion-beam-applied Biology, JAERI^{***}

Advanced Science Research Center, JAERI^{****}

1. Introduction

Recently the interaction of fast cluster ions with matter has attracted attention in basic physics and application fields¹⁻⁴⁾. As fast cluster ions can bombard a very small area of a solid surface by many atoms simultaneously and release large energy in a very short time (from femto- to pico-second region)⁴⁾. This situation causes non-linear effects or synergetic effects, which is unusual for single atom collision with solid targets.

Fast cluster ion beams used for the study of secondary ion emission processes were produced by the TIARA tandem accelerator. A time of flight (TOF) mass spectrometer combined with a pulsed cluster ion beam was used for a secondary ion measurement.

In this report we present some results of secondary ion emission from a highly oriented pyrolytic graphite (HOPG) target bombarded by carbon cluster ions.

2. Experimental

The experimental system of TOF mass spectrometry was composed of a pulsed ion beam generating system and an ion flight time measurement system.

A chopper and two sets of slits installed in an injector beam line generated pulsed ion beams by chopping continuous cluster ion

beams from an ion source. A square wave from a master pulse generator controlled a high voltage applied to parallel plate electrodes for chopping the beam. In this study pulsed cluster ion beams of 0.5 MeV/atom (~ 42 keV/amu) $C_1^+ \sim C_8^+$ ions were used. The duration and width of the pulsed beam used in this experiment were 125 μ s and ~ 100 ns, respectively. C_4^+ and C_8^+ ions were produced in the ion source and C_1^+ , C_2^+ and C_6^+ ions were fragments of C_8^+ ions after passing through charge stripper gas. As averaged beam currents of pulsed beams could not be measured, continuous beam currents measured before pulsing were several pA for C_8^+ ions. The vacuum in a beam line and a chamber was kept at $\sim 10^{-7}$ Pa to prevent cluster ions from breaking.

A linear type TOF mass spectrometer and a TAC (Time to Amplitude Converter) system for time measurement were adopted as a secondary ion mass spectrometric system. The TOF mass spectrometer composed of an extractor, a drift tube, an acceleration electrode and a multichannel plate (MCP) detector. A TTL output from the pulse generator was used as a start pulse and a secondary ion signal from the MCP was used as a stop pulse of the TAC measurement system. Typical mass spectrum was accumulated for 30 minutes. Sheet

shaped targets were used and bombarded at incident angle of 45 degrees. The secondary ions were extracted to the normal direction from the target.

Though targets were bombarded by nA continuous cluster ion beams for one or two hours to clean the target surface last year, cleaning was still inadequate (see Fig.1). This year the target was bombarded by 5keV Xe ion beam from an ECR ion source for 10 ~ 20 minutes.

Some results of a secondary ion emission from a HOPG target bombarded by 0.5MeV/atom C_1^+ ions, C_2^+ , C_4^+ and C_8^+ cluster ions will be discussed.

3. Results and discussion

Secondary ion mass spectra emitted from a HOPG target bombarded by C_1^+ ions and C_8^+ cluster ions are shown in Fig.1 and 2. The ordinate is the secondary ion yields normalized to the beam fluence in arbitrary units, and the abscissa is the channel number of multichannel analyzer, which corresponds to the flight time of ions (50 μ s / 1024 ch). Secondary carbon cluster ions are seen for any incident carbon cluster ion. And several dominant peaks which are H^+ , H_2^+ , H_3^+ , H_2O^+ , Na^+ , K^+ and so on can also be seen. These peaks are caused by surface contaminants.

Figure 2 shows typical mass spectra, which were taken after bombardment of 5keV Xe ion beams for 10 minutes. The contaminants and background signals remarkably diminished, and the secondary cluster ions appeared clearly, especially for C_8^+ ion bombardment, compared with spectra in Fig.1. Peak intensities of these secondary carbon cluster ions are plotted in Fig.3. In case of C_8^+ ion bombardment the emitted secondary carbon cluster ions from

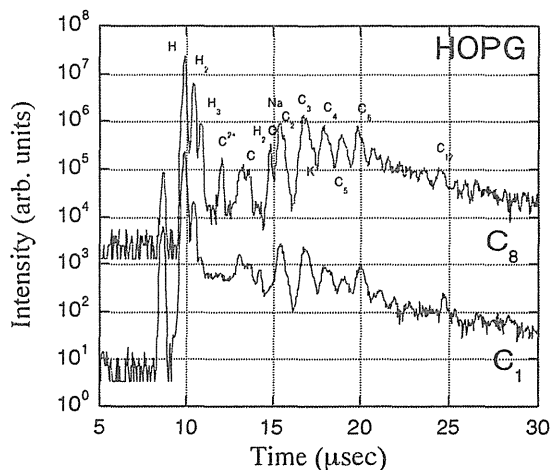


Fig.1. Secondary ion mass spectra emitted from a HOPG target bombarded by C_1^+ ions and C_8^+ cluster ions. Data were taken after bombardment of continuous cluster ion beams for one hour.

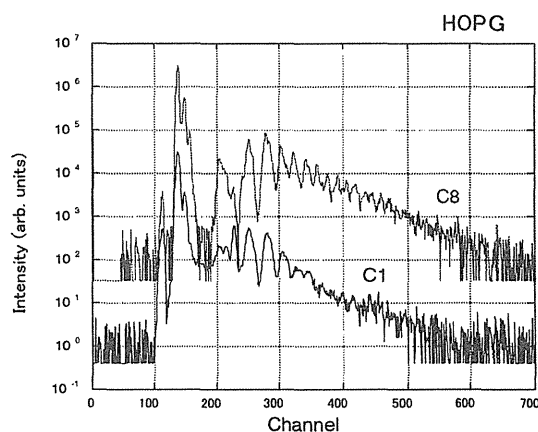


Fig.2. Secondary ion mass spectra emitted from a HOPG target bombarded by C_1^+ ions and C_8^+ cluster ions. Data were taken after bombardment of 5keV Xe ion beams for 10 minutes.

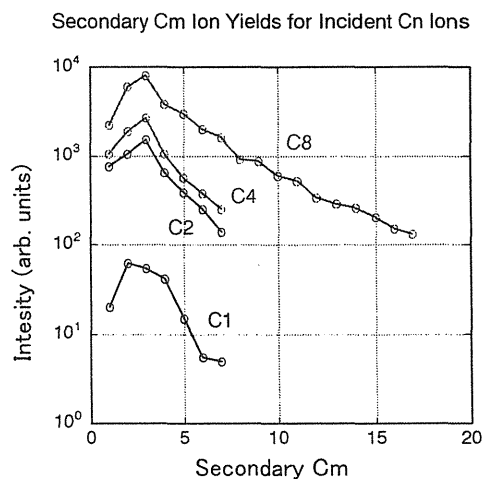


Fig.3. Secondary carbon cluster ion (C_m^+) intensity emitted from HOPG target bombarded by C_1^+ , C_2^+ , C_4^+ and C_8^+ ions.

C_1^+ to C_{17}^+ can be seen and intensities of these peaks decay exponentially. It is interesting to note that the most intense peak is C_3^+ ions for C_2^+ , C_4^+ and C_8^+ incident cluster ions.

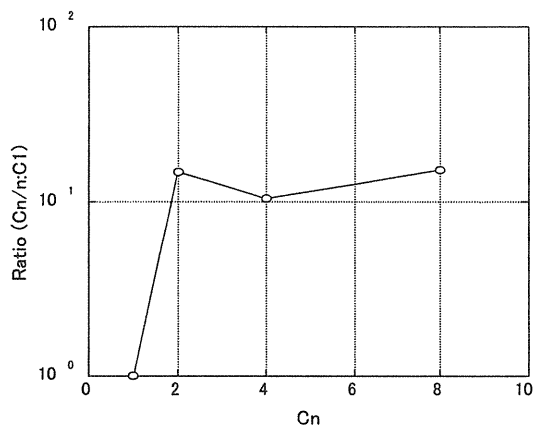


Fig.4. The ratio of yields of secondary ions per atom from HOPG target bombarded by C_8^+ cluster ions to that by C_1^+ ions.

Figure 4 shows the ratio of yields of secondary ions per atom from HOPG target bombarded by C_n^+ cluster ions to that by C_1^+ ions. If the relation between the ratio and C_n is linear, the value of the ratio is 1 for any C_n . However, the value of yield ratio for each incident cluster ions C_n^+ is over 10. The non-linear effect can be seen clearly.

The last problem concerning about experimental condition is the pulse width would be narrowed to get higher mass resolution.

References

- 1) Y. Le Beyec, Int. J. Mass Spectrom. Ion Proc. **174** (1998) 101.
- 2) S. Della-Negra, et al., Nucl. Instrum. Meth. B **74** (1993) 453.
- 3) M. Döbeli et al., Phys. Rev. B **94** (1994) 388.
- 4) K. Boussofiane-Baudin et al., Int. J. Mass Spectrom. Ion Proc. **130** (1994) 73.

9.4 The Effect of Ion Doping on Ionic Conduction of Sol-gel Phosphosilicate Glasses (II)

S. Ishiyama^{*}, S. Kitazawa^{*}, S. Yamamoto^{**} and M. Asano^{**}

Department of Advanced Nuclear Heat Technology, JAERI^{*}

Department of Material Development, JAERI^{**}

1. Introduction

Phosphosilicate glasses $(\text{P}_2\text{O}_5)_x(\text{SiO}_2)_{1-x}$ have a great deal of advantage in a high ionic conductivity in the medium temperature range, lightweight, heat-resistance and non CO toxification. A novel cogeneration system simultaneously can produce hydrogen and electric power from methane raw material using the nuclear heat by a new high temperature operation type solid electrolyte is developed. It is effective to improve the utilizing proton conductive solid electrolyte worked for the separation and use of the hydrogen energy for application of the fuel cells. Furthermore the advantages of the optical property, there are many applications of optical fiber as Raman lasers¹⁾. In the study for the phosphosilicate glass, the sol-gel method has advantage in random structure of the glass organization for proton conductivity²⁾. There are many studies to investigate the structure of phosphosilicate glass³⁾. In order to investigate dynamic effects of structural change by implanted ion on the proton conduction mechanism for the improvement in ionic conductivity in phosphosilicate glass. The structure of the sol-gel synthesis is a peculiar porous material⁴⁻⁵⁾. Then, by measuring radiation-induced luminescence (RIL) during the ion irradiation for the proton conductivity glass at in-situ, it tried to examine the correlation between RIL and structural change and conduction function in ion irradiation in order to clarify complicated change in glass structure and the mutual influence. The RIL spectra from silica glass are measure in several researcher and the red band (1.9 eV), blue band

(2.7 eV) and UV band (4.3 eV) were observed by the electron irradiation (cathode luminescence CL)⁶⁾ and a blue band (3.1 eV) is observed by the gamma and X-ray irradiations⁷⁾. In this paper, the 1 MeV H^+ ion beam was irradiated on silica glasses (SiO_2) and phosphosilicate glasses were prepared by sol-gel method to investigate dynamic effects of structural change. The changes of optical properties (absorption, PL and PL excitation (PLE) spectra) before/after ion irradiations and RIL were studied.

2. Experimental Procedures

The silica and phosphosilicate glass were prepared using tetraethoxysilane (TEOS); $\text{Si}(\text{OC}_2\text{H}_5)_4$ and trimethylphosphate; $\text{PO}(\text{OCH}_3)_3$ solution. TEOS was hydrolyzed for 1 h with water under magnetic stirring at room temperature. Ethanol was used as solvent system and formaldehyde (HCONH_2) as a catalyst. The molar ratio of TEOS: $\text{C}_2\text{H}_5\text{OH}$: H_2O : HCl was 1: 1: 1: 0.01. For the phosphosilicate glass, an alkoxide $\text{PO}(\text{OCH}_3)_3$ solution was added to the hydrolyzed TEOS solution as the molar ratio of $\text{C}_2\text{H}_5\text{OH}$: H_2O : HCl = 4: 4: 0.03 and stirred for 1 h at room temperature. The obtained transparent sols were left in glass containers. Final gels were obtained in air for 3 - 4 weeks. The dried gels were then heated to 600 °C at a rate of 50 °C/h and held at this temperature for 5 h. The ion irradiation experiments were performed using the 3 MV tandem accelerators in Takasaki Ion Accelerators for Advanced Radiation Application (TIARA) at JAERI Takasaki. The H^+ ion irradiations were performed using

fluencies of 5×10^{15} ions/cm², at 1 MeV at room temperature, with a beam current density of $0.2 \mu\text{A}/\text{cm}^2$. The ion beams direction was almost normal of the target surface. For the absorption spectroscopy, the spectra were observed by a double monochromator with a high-performance blazed holographic grating in the aberration corrected Czerny-Turner mounting with the resolution of 0.1 nm (~ 30 meV). For the PL and PLE spectroscopy, the spectra were recorded under 150 W Xe lamp illuminations and detected by a monochromator with a concave, blazed holographic grating, F/2.5, 1300 grooves/mm. The accuracy of wavelength is within 1.5 nm. For the RIL spectroscopy, the light emitted from the target was focused into an optical fiber input that located 60 degree and 30 cm from the target. The interface between vacuum chamber and air is a view port, which made from fused silica with no surface coating, that the transmittance at the ultra violet (UV) range above 5 eV is very low. The spectrometer consists the thermoelectric-cooling type Back-thinned (BT) charge coupled device (CCD) image sensors operated, which has quantum and a compact Czerny-Turner type spectrograph with F number 4, optical fiber probe and control circuit. The wavelength resolution is less than 2 nm.

3. Results and discussions

Figure 1 shows the ultra violet (UV) and visible absorption spectra of the silica glass

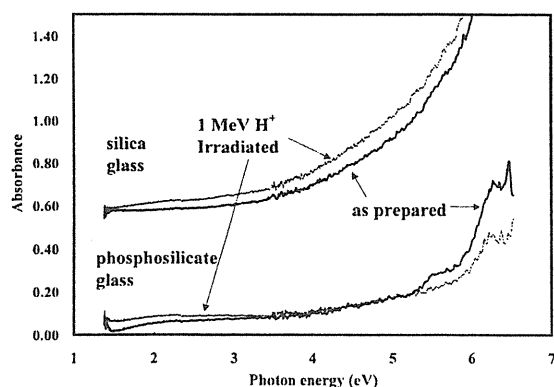


Fig.1 Absorption spectra of Phosphosilica.

and phosphosilicate glass samples. The solid lines and broken lines represent for as prepared (before irradiation) and 1 MeV H⁺ ion irradiation (after irradiation), respectively. There are not any peaks in each spectrum except for over 5 eV in phosphosilicate glass, so it shows the absence of the characteristic atomic or ionic absorbance in this range. In each spectrum, there are not conspicuous peaks because there are not any specific absorption peaks in this region. The absorbance of the silica glass is lower than that of phosphosilicate glass, because the ratio of porous structure contributed to the optical absorbance mechanism is decreased as the doped phosphor in the sol-gel methods. The absorbances after irradiation are higher in each pair of the spectra, because defects were produced by the irradiation. It is so called "colour centre".

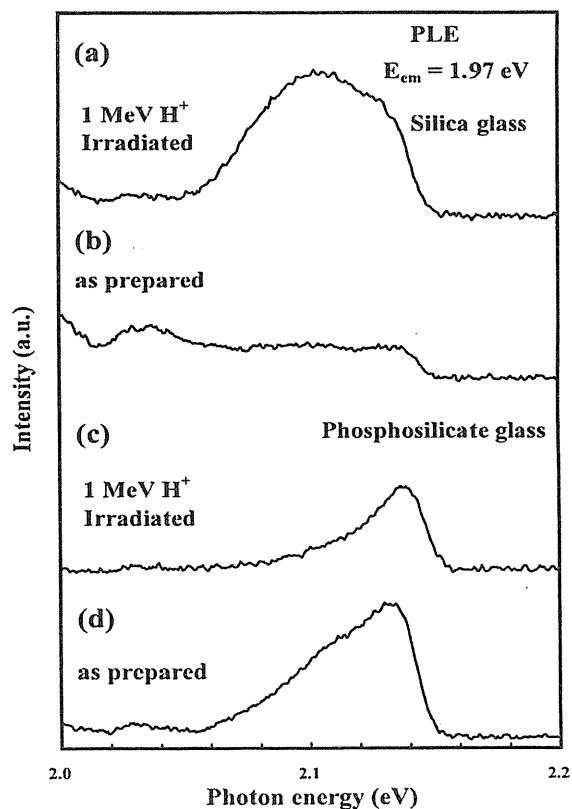


Fig.2 PLE spectra detected from glasses.

The silica glass shows a variety of PL phenomena due to defects in the sol-gel silica

glass network; oxygen deficiency-related defects ($\cdot\text{Si}^*$, $\cdot\text{Si-Si}$, oxygen vacancies,...) and oxygen excess-related defects ($\cdot\text{Si-O}^*$, $\text{O=O}, \dots$)⁴⁻⁵⁾. The mechanisms of RIL is explained on the analogy of PL phenomena. Several bands are observed in the experiment; the band centered at 2.11 and 2.13 eV in the PLE as shown in Fig. 2, 1.92 eV in the RIL and 1.98 eV in the both PL and RIL. The mechanism of PLE is comparatively simple⁴⁻⁵⁾. The PLE spectra have single band that is consist from a non-bridging oxygen hole center (NBOHC) $\cdot\text{Si-O}^*$ and a Proxy radical (POR) $\cdot\text{Si-O-O}^*$. The activities of the oxygen excess-related defects that produce the red band are low as prepared silica glass, but the ion irradiation elevated them (Fig. 2(a) and (b)). For the phosphosilicate glass, the activities are enough elevate in as-prepared state. The red bands of the PLE are anti-symmetrical and deconvoluted into two peaks, R_1 (2.11 eV, FWHM 0.04 eV) and R_2 (2.13 eV, FWHM 0.02 eV) by Lorentzian curve fitting. The relative intensity $R_1:R_2$ ratios of those peaks in before and after irradiation are 1: 1 (Fig. 2 (a)) and 10: 2 (Fig. 2(b)) at the silica glass and 4: 4 (Fig. 2(c)) and 2: 3 (Fig. 2 (d)) at the phosphosilicate glass, respectively. The assignments of excitation levels are not performed⁴⁻⁵⁾, but the existences of site-selective excitations are confirmed. In the case of silica glasses (Fig. 2 (a) and (b)), the intensities of peaks after irradiations are higher than those of before, because the defects of the sol-gel silica glass networks were activated by the irradiation. In the phosphosilicate glasses (Fig. 2 (c) and (d)), the results are contrary, because the existence of phosphor prevents the generations of the defect as forming phosphorus centers (O=P , P-O-S , $\text{P-O-P}, \dots$). In the RIL spectra, the band with the peak of 1.98 eV appeared only in the silica glass (Fig. 2). The peak position is almost same as the peak of 1.97 eV in the PL spectra, but the shape is asymmetrically tailed a skirt on lower energy side. It is derived from

the difference of the excitation process. In the case of PL, the excitation is occurring by absorptions of a photon with energy of 2.14 eV, so the energy loss is about 0.2 eV as thermal activation energy. In the RIL, the irradiation is the collision between the target glass and H^+ ion with kinematics energy of 1 MeV, therefore the excitation is produced by inelastic collision accompanied with electronic excitations. The red band (1.97 eV) in the RIL spectra of phosphosilicate glass is disappeared. It is considered that the production of the NBOHC ($\cdot\text{Si-O}^*$) are not proceeded or-and more dominantly relaxation process are exist. Phosphosilicate glass is thought currently to consist of silicon-oxygen, SiO_4 , and phosphorus-oxygen, O=PO_3 , tetrahedral bonded randomly in a three-dimensional network where each silicon atom is bonded with four silicon or phosphorus atoms by oxygen linkages, and each phosphorus atom has only three such bridging bonds. Therefore the NBOHC ($\cdot\text{Si-O}^*$) are not effectively created by the H^+ ion irradiation.

References

- 1) Rini M, Cristiani I, Degiorgio V, Kurkov A S and Paramonov V M 2002 *Optics Communications* **203** 139-44.
- 2) Matsuda A, Kanzaki T, Tadanaga K, Tatsumisago M and Minami T 2001 *Electrochimica Acta* **47** 939-44.
- 3) Plotnichenko V G, Sokolov V O, Koltashev V V and Dianov E M 2002 *J. Non-Cryst. Solids* **306** 209-26.
- 4) Skuja L 1998 *J. Non-Cryst. Solids* **239** 16-48.
- 5) Skuja L, Tanimura K and Itoh N 1996 *J. Appl. Phys.* **80** 3518-25.
- 6) Fitting H-J, Barfels T, Czarnowski A von and Trukhin A N 2000 *Mater.s Sci. Eng. B* **71** 109-14.
- 7) Yoshida T, Tanabe T, Ii T and Yoshida H 2002 *Nucl. Instr. and Meth. B* **191** 382-6

9.5 Present Status of JAERI AVF Cyclotron System

Y. Nakamura*, T. Nara*, T. Agematsu*, I. Ishibori*, S. Kurashima*, K. Yoshida*, M. Fukuda*, S. Okumura*, N. Miyawaki*, S. Tajima*, K. Akaiwa**, To. Yoshida**, S. Ishiro**, Y. Arakawa**, Tu. Yoshida**, S. Kanou**, A. Ihara** and K. Takano**

Advanced Radiation Technology Center, JAERI*
Beam Operation Service, Co., Ltd.**

1. Operation and Utilization

The JAERI AVF cyclotron system¹⁾⁻³⁾ continues to operate smoothly as well as past years. An alteration frequency of operational condition for past 12 years is shown in Fig. 1. These frequencies such as harmonic number, particle, energy and beam course gradually increase. Especially, the number of beam

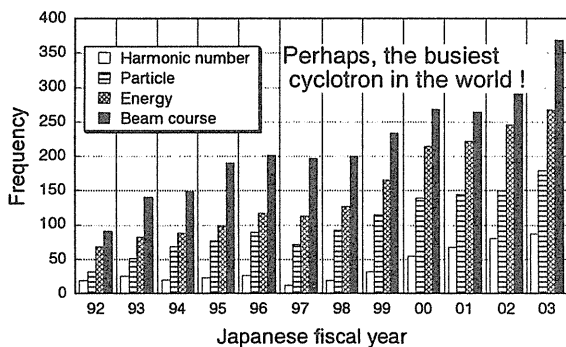


Fig. 1 Frequency of alteration of operational condition for past 12 years.

course change rapidly attained up to 369 which exceeded to more than 300 for the first. As the result, the utilization efficiency for cyclotron system, which is defined as the ratio of total allotment time to experimental one for users, decreases slowly for recent eight years as shown in Fig. 2.

In consideration of above circumstances, we propose the well-improved operation schedule that the operation time for a year increases slightly in order to compensate the reduction of utilization efficiency. The operation time for

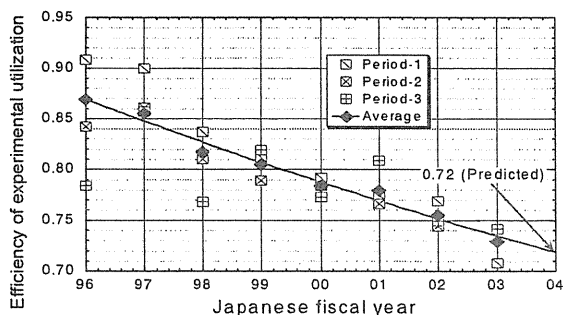


Fig. 2 Efficiency of machine time for 8 years.

last fiscal year 2003 was 3382 h which was the second longest so far. Since 1993 when the operation time for a year became steady state, one always exceeds more than 3000 hours surely although various reconstruction, improvement, renewal, maintenance, repair and so on have been carried out.

2. Present Status

2.1 Development and Improvement

With a view to certain producing the micro-beam, the central region devices of the cyclotron were improved to realize the excellent space controllability and high device reliability for the beam. Based on the detail analysis of the central region, the beam exit from the inflector was rotated about 180 degrees in comparison with the original position at third harmonic mode. In the case of first and second harmonics, these positions were a little different. The position and shape of two set of the defining phase slits were also designed carefully. Furthermore, the inflector electrode and its shield cover were separated independently as shown in Fig. 3. The modified common shield cover was fitted up at upper earth plate of the cyclotron center.

The cyclotron tuning for micro-beam production has being continued energetically under operation of the flat-top system⁴⁾. Clear turn separation at a few outermost orbits in the cyclotron was observed using the deflector probe equipped with thin molybdenum

sheet and slender graphite rod. And, the single-turn extraction was also made sure about the

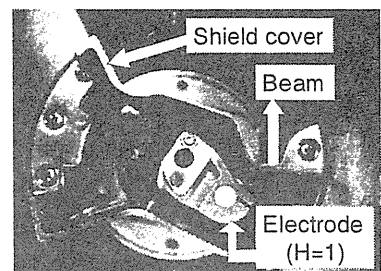


Fig. 3 New inflector electrode and shield cover (from bottom).

extracted beam of 260 MeV, $^{20}\text{Ne}^{7+}$ by means of beam pulse detection.

A new compact ECR ion source which only consists of permanent magnets has been developed. The shape of the magnet made of NdFeB was minutely designed using TOSCA code. The diameter of inner

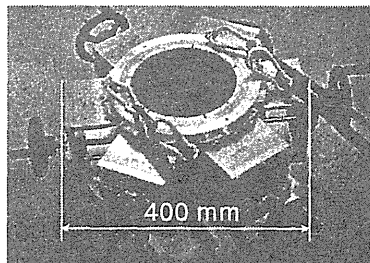


Fig. 4 An appearance of permanent magnet.

hole and the width of the magnet are 40 mm and 120 mm, respectively. As shown in Fig. 4, it is the principal characteristics that this magnet can be moved up to 50 mm along the radial direction by six round handles.

The energy absolute value of accelerated ion beam, especially light ions, was measured accurately by method of TOF. Actual energies for several kinds of protons from 10 MeV to 80 MeV and some heavy ions were obtained. The measured value was greater than the nominal one about -3 to +5 %. On the other hand, the difference between the value measured by TOF and the practical value estimated from the analyzing magnet installed at the beam transport line was evaluated at 0 to +2 %.

The ventilation condition in the power supply room was improved so that the warmed air through the cooling fan can be

almost sucked into the distributed duct directly as shown in Fig. 5. By this improvement, temperature rise in the room was suppressed more than 10 °C.

2.2 Maintenance and Repair

Comprehensive periodical maintenance including the improvement of central region devices of the cyclotron for 4 weeks and beam tuning for about 2 weeks in summer, the routine maintenance of power supplies for 1 week on October, the reconstruction of the TMP frame and installation of the cooling panels⁵⁾ for 2 weeks on late March were performed in last fiscal year.

Typical serious troubles during last year are summarized in Table 1. Half of them were concerned with the vacuum events including the water leak in vacuum. On late June, a little spout of cooling water happened at the coupling pipe for mechanical-seal of the main circulation pump as shown in Fig. 6. The cause of this water leak was originated from abnormal vibration of the shaft coupler between the mechanical-seal pump and electric induction motor.

On early October, worse vacuum condition of the cyclotron appeared during the test operation, several hours later the water leak at

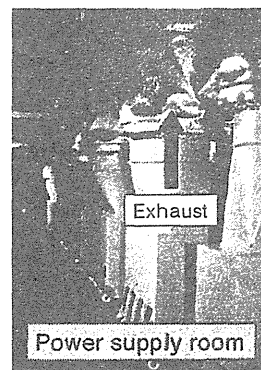


Fig. 5 Improvement of arrangement of ventilation duct.

Table 1 Summary of typical troubles occurred during fiscal year 2003.

Date	System	Content of troubles	Treatment
04/24	Control	Stop the operational sequence for inflector at harmonic mode change	Temporary treatment
06/25	Cooling	Spout of water at the coupling pipe for mechanical seal of circulation pump	Replace. of coupl. pipe
06/30	Cooling	Water leak at the mechanical seal of pump for cyclotron stabilization	Replace. of seal
07/01	RF	Malfunction of P-chopper----Deterioration of water-cooled resistor	Replace. of resistor
08/08	Vacuum	Error operation and damage of gate valve (between cyclotron and injection)	Replace. of gate valve
08/15	Vacuum	Water leak in the driving shaft for puller (in cyclotron vacuum chamber)	Disassem. & Replace.
08/28	Vacuum	Rapid air inflow into cyclotron by miss handling----Oil dropping inside	Cleaning & Recovery
09/01&24	Vacuum	Vacuum leak at two bellows for Attenuator #1 and FC for ECR	No use. #1&Replace. FC
09/26	RF	Malfunction of start sequence of S-chopper	Replace. of relays
09/29	Vacuum	Breakdown of TMP(600 L/s) vane and hair crack generation at vacuum chamber for beam diagnosis----Increase of vibration at vacuum system	Replace. of TMP & vacuum chamber
10/08	Vacuum	Bad vacuum condition of cyclotron----Water leak at RF shield for Cryo. Pump	Replace. of RF shield
10/27	Control	Sequencer alarm (for vacuum control in No.1 light ion room)----Radi. damage	Reinstall. of seque.progm.
12/04	Pow. Sup.	Meltdown of rapid fuse in main RF amplifier box (twice)	Replace. of fuse
02/09	Control	Malfunction of buncher----Damage of FET(2SK409) in power amplifier	Replace. of FET's
02/17	Vacuum	Bad vacuum condition of cyclotron----Water leak at baffle of Mag. Channel	Replace. of baffle
02/23	Pow. Sup.	Electric leakage in AC 200V line----Contact of connector pin for cryo. Pump	Temporary treatment
03/04	Vacuum	Malfunction of small air-cooled TMP for HECR----Reassemble	Carring & repair
03/24	Vacuum	Bad vacuum condition of ECR----Crack at the window for micro-wave	Repair (maker)
03/25	Vacuum	Water leak in the stem of Inflector----Crack generation in coupled block	Disassembly & Repair

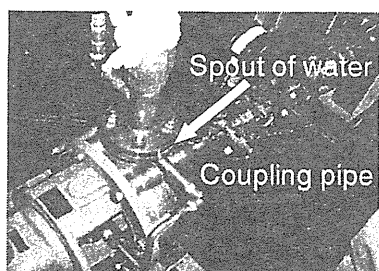


Fig. 6 Spout of water at main circulation pump.

the RF shield in front of the cryogenic pump was found out based on the information of vapour partial pressure from a quadrupole mass analyzer. Fortunately, we could restore this trouble quickly, since the used spare parts had been just stocked.

As well as the serious trouble experienced once in 1994, the TMP vane was broken completely as seen in Fig.7 and the hair crack occurred at the conjunction part to the beam diagnostic chamber. Therefore, some measures for avoidance from serious vibration were performed later, of course, the damaged TMP and chamber were also replaced by new ones.

On early February, the buncher driven by sinusoidal wave came to out of order. The breakdown of a small power FET (2SK409) in the amplifier was discovered after careful investigation.

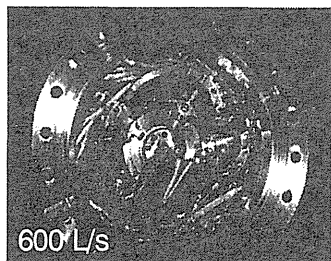


Fig. 7 Breakdown of TMP rotating vane.

3. Beam Development

After improvement of the central region devices, the test operation for beam tuning was continued energetically about thirty kinds of the allotted ion species for utilization since the middle of August.

Sixty-five kinds of ion species have been accelerated by the JAERI AVF cyclotron so far as summarized in Table 2.

Two sorts of He^{2+} ion of 75 MeV and 80 MeV with harmonic number (H) of 2 were newly developed for efficient utilization and less radioactivation on the experiment of RI production, instead of 100 MeV ion with H=1. The intensities of both ions were successfully extracted about 6 μA .

Both efficiencies of "Text" and "Tail" in several kinds of ions were also improved by the fine tuning mainly in daily operation.

References

- 1) Y. Nakamura, T. Nara, *et al.*, TIARA Annual Report 2002 (JAERI-Review 2003-033) (2003) pp. 312-314
- 2) Y. Nakamura, T. Nara, *et al.*, Proc. 4th Int. Workshop on Accel. Opera., Kanagawa and Ibaraki, Japan (2003) pp. 8-13
- 3) Y. Nakamura, T. Nara, *et al.*, Proc. 16th Int. Conf. Cyclo. Their Applic., East Lansing, MI, USA (2001) pp. 129-132
- 4) S. Kurashima, M. Fukuda, *et al.*, this annual report
- 5) Y. Nakamura, K. Takano, *et al.*, this annual report

Table 2 The list of ion species accelerated by the JAERI AVF cyclotron. The symbol of "Text" is defined by a ratio of the beam current at the Faraday cup just behind the cyclotron to that at 900 mm of the cyclotron radius. The "Tail" is a ratio of the beam current extracted from the cyclotron to that injected into.

Ion species	Energy (MeV)	Intensity (μA)	Text (%)	Tail (%)	Ion species	Energy (MeV)	Intensity (μA)	Text (%)	Tail (%)	Ion species	Energy (MeV)	Intensity (μA)	Text (%)	Tail (%)
H^+	10	12	80	27	4He^{2+}	100	10	32	10	$^{36}\text{Ar}^{8+}$	195	2.5	73	13
	20	11.5	89	25		108	1.6	M/Q=2			195	0.1	43	1.2
	30	6.2	78	22	$^{12}\text{C}^{3+}$	75	2	M/Q=4		$^{36}\text{Ar}^{10+}$	970	10 ⁵ cps	M/Q=2	
	45	30	79	14	$^{12}\text{C}^{5+}$	220	0.25	77	22	$^{40}\text{Ar}^{8+}$	150	2.4	M/Q=5	6.2
	50	5	64	14	$^{12}\text{C}^{6+}$	320	0.037	M/Q=2			175	3	73	15
	55	5	63	14	$^{14}\text{N}^{3+}$	67	4	43	10	$^{40}\text{Ar}^{10+}$	250	0.2	M/Q=4	
	60	5	68	22	$^{15}\text{N}^{3+}$	56	0.70	M/Q=5	5.0	$^{40}\text{Ar}^{11+}$	330	0.7	86	22
	65	7	78	12	$^{16}\text{O}^{4+}$	100	5	M/Q=4	22	$^{40}\text{Ar}^{13+}$	460	0.045	76	24
	70	5	42	12	$^{16}\text{O}^{5+}$	100	4	34	21	$^{40}\text{Ca}^{9+}$	200	2	61	11
	80	4.4	72	13	$^{16}\text{O}^{6+}$	160	1.9	58	21	$^{56}\text{Fe}^{11+}$	210	1.4	M/Q=5	16
	90	10	48	7.7	$^{16}\text{O}^{7+}$	225	1	82	13	$^{56}\text{Fe}^{15+}$	400	0.59	66	28
D^+	10	11	29	3.7		335	0.1	41	6	$^{58}\text{Ni}^{15+}$	390	0.012	M/Q=4	
	20	5.6	80	16	$^{16}\text{O}^{8+}$	430	0.0045	M/Q=2		$^{82}\text{Kr}^{20+}$	490	10 ⁵ cps	M/Q=4	
	25	15	88	31	$^{20}\text{Ne}^{4+}$	75	1.5	M/Q=5	6.6	$^{84}\text{Kr}^{17+}$	320	0.08	M/Q=5	5.0
	35	40	76	23	$^{20}\text{Ne}^{5+}$	125	0.01	M/Q=4		$^{84}\text{Kr}^{18+}$	400	0.04	60	2
	50	20	49	9.7	$^{20}\text{Ne}^{6+}$	120	1.6	53	18	$^{84}\text{Kr}^{20+}$	520	0.06	75	22
$^3\text{He}^{2+}$	60	8.2	68	18	$^{20}\text{Ne}^{6+}$	200	0.8	Scaling		$^{84}\text{Kr}^{21+}$	525	0.0032	M/Q=4	
$^4\text{He}^{2+}$	25	3.6	M/Q=4	13	$^{20}\text{Ne}^{7+}$	260	9.8	70	22	$^{102}\text{Ru}^{18+}$	320	0.013	50	3.9
	20	5.5	69	12		270	0.28	Scaling	14	$^{120}\text{Xe}^{23+}$	450	0.2	72	14
	30	10	42	10	$^{20}\text{Ne}^{8+}$	350	1.5	63	26	$^{199}\text{Au}^{31+}$	500	0.038	49	3.8
	50	20	36	22	$^{20}\text{Ne}^{10+}$	540	10 ⁵ cps	M/Q=2						
	75	6	81	7.5	$^{22}\text{Ne}^{6+}$	165	0.007	M/Q=4						
80	6	65	9.2											
M/Q = 2, 4 and 5 : a series of cocktail beams														
Woven pattern : modified data on previous table														

9.6 Beam Development for Flat-top Acceleration in the JAERI AVF Cyclotron (II)

S. Kurashima, M. Fukuda, S. Okumura, N. Miyawaki, T. Nara
T. Agematsu, I. Ishibori, K. Yoshida, Y. Nakamura and K. Arakawa
Advanced Radiation Technology Center, JAERI

1. Introduction

A flat-top acceleration system using fundamental and fifth-harmonic frequencies for an acceleration voltage has been developed to minimize the energy spread mainly for a microbeam production¹⁾. The energy spread of a beam extracted from a cyclotron is required to be reduced to $\Delta E/E \leq 0.02\%$ to produce a microbeam with a spot size of $1\ \mu\text{m}$ by focusing the beam with a set of quadrupole magnets. The flat-top acceleration is an excellent technique to reduce the energy spread²⁾. In order to achieve the energy spread of $\Delta E/E \leq 0.02\%$, precise control of beam phase and stabilization of the magnetic field and the acceleration voltage are required in addition to the flat-top acceleration system. So far, the tolerable stability of the acceleration voltage, $\Delta V/V \leq 0.02\%$, and the magnetic

field, $\Delta B/B \leq 0.002\%$, have been already achieved. In this paper, we report improvement of a central region for the precise beam phase defining and the development of a new beam buncher system to inject a beam into the defined phase range with high efficiency. Preliminary beam development of a 260 MeV $^{20}\text{Ne}^{7+}$ ion beam using the flat-top acceleration technique is also described.

2. Highly efficient beam buncher system

In order to succeed in the flat-top acceleration, a beam phase width has to be limited within $\pm 8^\circ$ rf²⁾. In this condition, beam injection efficiency from the ion source into the cyclotron is very low even if a conventional sinusoidal waveform beam buncher is used. In general, a saw-tooth voltage waveform is more suitable for highly efficient beam bunching to modulate the energy of the injected beam. The saw-tooth waveform voltage was generated by combining the fundamental, second and third harmonics of a sinusoidal waveform voltage so far. This method requires an individual signal control system for each harmonics, which brings an increase in costs.

We have been developing a new type of saw-tooth waveform beam buncher. The saw-tooth waveform is generated by using the transitional phenomenon of electric circuit, and it requires a single control system. The saw-tooth waveform of the new beam buncher observed by an oscilloscope and a high voltage probe is shown in Fig. 1.

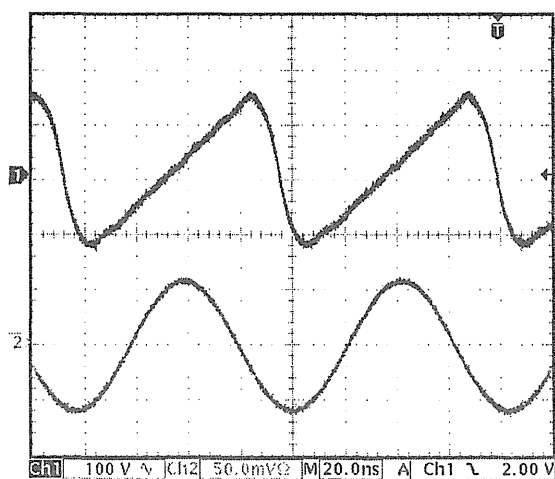


Fig. 1 Voltage waveforms of the beam buncher. The upper saw-tooth and the lower sinusoidal waveforms represent the newly developed buncher and the usual one, respectively.

The beam bunching test was performed using a 260 MeV $^{20}\text{Ne}^{7+}$ ion beam. As a result, a beam current by using the new saw-tooth waveform buncher was increased 5 times as large as that without a beam buncher, while 3.8 times by a conventional sinusoidal waveform buncher. Furthermore, by operating both beam bunchers simultaneously, a beam current increased up to 6.3 times.

3. Development of the new central region

A newly designed central region of the cyclotron has been installed to improve the capability of the beam phase defining slits for precise control of beam phase width. In order to create strong correlation between the beam phase and the radial position of beams at the phase slits, configuration and arrangement of the electrodes in the central region were optimized by using the three dimensional electromagnetic field analysis code TOSCA and an orbit calculation code.

The arrangement of electrodes and beam trajectories for acceleration harmonics $h=2$ is shown in Fig. 2. Temperature increase of an rf-shield, caused by rf heating, is reduced by water cooling pipes. The rf-shield cover is isolated to prevent thermal conduction from the rf-shield cover to the inflector electrode. The design of the inflector electrode itself was not changed in this modification of the central region. Positions of the inflector electrode and the puller electrode were determined to realize the necessary correlation between the beam phase and the radial position of beams. The puller electrode can be used in common for acceleration harmonics of 1 and 2. The beam phase width is controllable by two pairs of the phase slits.

4. Development of the flat-top accelerated beam

We have been developing a 260 MeV $^{20}\text{Ne}^{7+}$

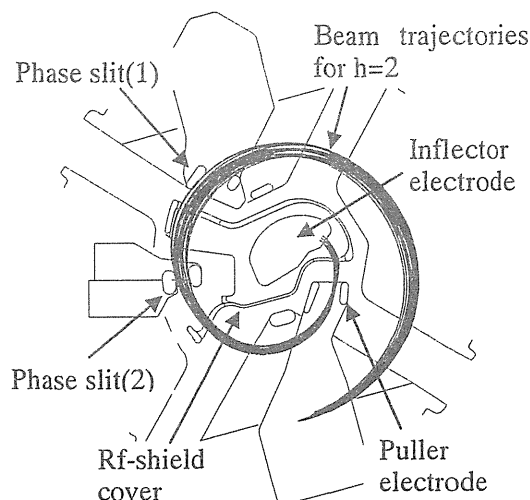


Fig. 2 Schematic drawing of the improved central region.

ion beam with the flat-top acceleration system for the biological application. Operation parameters of the cyclotron, such as ratio of fundamental and fifth-harmonic voltages, magnetic field, beam pulse width, were optimized to achieve single-turn extraction that is an indispensable condition to obtain the energy spread of $\Delta E/E = 0.02\%$. A radial spread of the beam in the extraction region of the cyclotron can be reduced by the flat-top acceleration owing to the uniformity of energy gain. Figure 3 shows the beam patterns of the 260 MeV $^{20}\text{Ne}^{7+}$ ion beam measured by the deflector probe of differential type using a molybdenum sheet. Obvious turn separation in

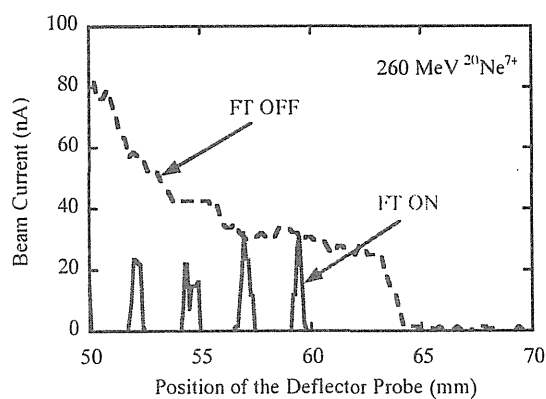


Fig. 3 Beam patterns of the 260 MeV $^{20}\text{Ne}^{7+}$ ion beam measured by the differential probe placed at the entrance of the deflector.

the beam pattern for the flat-top acceleration (FT ON) has been observed in the extraction region, while no turn separation has been seen in the ordinary acceleration mode without flat-topping (FT OFF).

5. Measurement of beam energy spread

In order to measure the energy spread of the flat-top accelerated beam, we have developed a micro-slit system to evaluate the horizontal beam spread caused by energy dispersion in the energy-analysing magnet. The object size of the beam is horizontally defined with a set of the

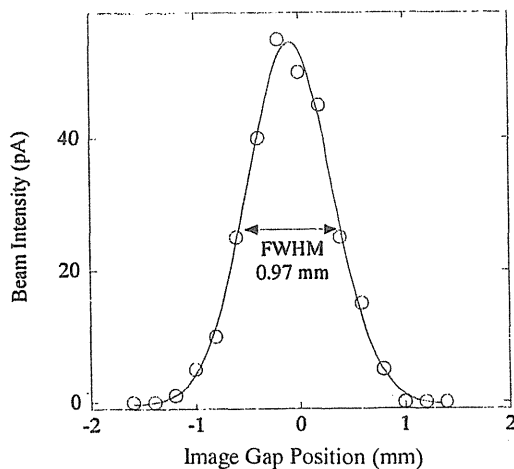


Fig. 4 Beam image of the 260 MeV $^{20}\text{Ne}^{7+}$ ion beam measured with the micro-slits and a Faraday cup by scanning the gap position of the image slits.

micro-slits. The image size of the beam dispersed with the energy-analysing magnet is measured with a set of the micro-slits and a beam intensity monitor. Either a Faraday cup or a semiconductor detector is used for the beam intensity monitor, selected according to the beam intensity. The gap of the micro-slits is defined by adjusting the left and right slit positions individually with micrometers. Minimum gap of the micro-slits is 10 μm . The designed energy resolution of the micro-slit system is $\Delta E/E = 0.001\%$. The gap position is scanned automatically with a stepping motor. The micro-slit system was installed at beam diagnostic chambers in the beam line of the cyclotron.

We carried out a preliminary test of the energy spread measurement for the 260 MeV $^{20}\text{Ne}^{7+}$ ion beam with flat-top acceleration. Figure 4 shows a measured dispersed beam image with a 1 mm gap of the micro-slits. The energy spread of the flat-top accelerated beam was estimated to be less than 0.1 % full width at half maximum (FWHM).

References

- 1) S. Kurashima, et al., TIARA Annual Report 2002 (JAERI-Review 2003-033) (2003) 310.
- 2) M. Fukuda, et al., Rev. Sci. Instrum. 74 (2002) 2293.

9.7 Design of a Small ECR Ion Source with Permanent Magnets for Cyclotron

K. Yoshida, T. Nara, Y. Saitoh, W. Yokota
Advanced Radiation Technology Center, JAERI

1. Introduction

The JAERI AVF cyclotron has been providing various ion beams to experiment for R&D in materials science and biotechnology science since 1991.

In 2000, we carried out to reduce the magnetic field change by the temperature rise of the cyclotron which caused the intensity change of accelerated beam. As a result, we realized the high magnetic field stability of the order of 10^{-5} for tens of hours, and beam intensity has become stable without adjustment of magnetic field¹⁾.

On the other hand, the improvement of the beam stability of the ion sources leads to the higher stability of cyclotron beams and the reduction of the adjustment time. Two ECR ion sources the heavy ion generation and metallic ion generation, respectively, are installed at the JAERI cyclotron²⁾. The beam extracted from the sources has long-period instability and it is thought that the temperature rise of the mirror coils change the magnetic field and consequently the condition of the plasma very slowly.

For this reason, we have started development of an all-permanent-magnet ECR ion source.

2. Magnet design

2.1 Mirror and hexapole magnet

The schematic view of the all-permanent-magnet ECR ion source is shown in Fig.1.

The JAERI cyclotron can accelerate ions with $M/Q \leq 6.5$ (M: mass number, Q: charge state). Therefore, the microwave frequency is set at 14GHz ($B_{\text{ECR}}=0.50\text{T}$) to produce not only light ions but also highly charged ions of medium-heavy element.

The magnet design was carried out by using the code OPERA3D that calculates three-dimensional magnetic field. We chose the N48H (Shin-Etsu Chemical Co., Ltd) of NdFeB for the

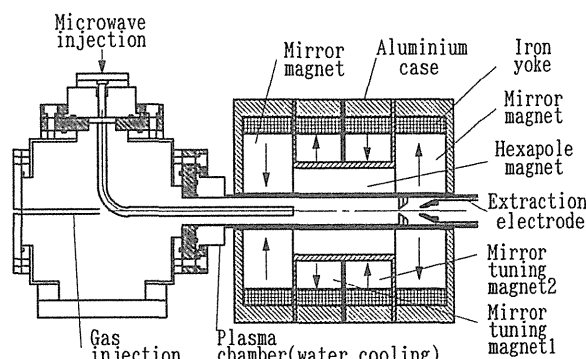


Fig.1 Cross sectional view of the ECR ion source.

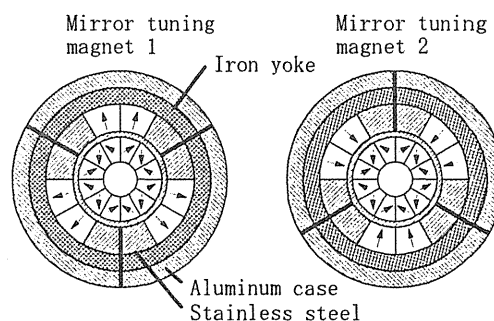


Fig.2 Cross sectional view of the mirror tuning magnets and the hexapole magnet.

mirror magnets from the point of view of the high magnetic flux density. As a result of calculation, the maximum magnetic flux density B_{MAX} of 0.80T ($1.6B_{\text{ECR}}$) was obtained. The minimum magnetic flux density B_{MIN} was 0.32T, and the mirror ratio $B_{\text{MAX}}/B_{\text{MIN}}$ was 2.5. In order to adjust the magnetic flux density, the mirror tuning magnets which can be removed are installed between the mirror magnets. They change B_{MAX} to 0.88T ($1.76B_{\text{ECR}}$), B_{MIN} to 0.22T, and $B_{\text{MAX}}/B_{\text{MIN}}$ to 4.0. The calculated size of the resonance zone is 110mm in length and 25.4mm in diameter.

It is also required that the magnetic flux density at the hexapole magnet is as high as possible. If we use the N48H for the hexapole magnet as well as for the mirror magnet, the magnet flux density

decreases by a few percent when the magnet temperature become 45°C due to the temperature rise of the plasma chamber. For this reason, the N44MH is selected as hexapole magnet from the points of the higher coercive force. In addition, the mirror tuning magnets are arranged not to increase the demagnetizing field against the hexapole as shown in Fig. 2. The magnetic flux density at the chamber surface is 0.80T ($1.6B_{\text{ECR}}$). The main parameters are listed in Table 1. The calculated and measured values of the magnetic flux density of axial and radial fields are shown in Fig.3 and Fig.4.

The measured size of the resonance zone with the mirror-tuning magnets is 109mm in length, and 25.8mm in diameter. The measured magnetic flux densities are $B_{\text{MAX}}=0.86\text{T}$ ($1.7B_{\text{ECR}}$), $B_{\text{MIN}}=0.20\text{T}$, $B_{\text{MAX}}/B_{\text{MIN}}=4.3$.

Table 1. Specification of the ECR ion source.

Microwave:		
Frequency		14GHz
Maximum power		125W
Mirror magnet:		
Material		NeFeB (N48H)
Length		240mm
Outer diameter		182mm
Inner diameter		41mm
Maximum field strength		0.88T
Minimum field strength		0.22T
Hexapole magnet:		
Material		NeFeB (N44MH)
Length		120mm
Outer diameter		102mm
Segment		12piece
Inner diameter		41mm
Radial field at 16mm		0.80T
Plasma chamber:		
Outer diameter		39mm
Inner diameter		32mm
Material		SUS316

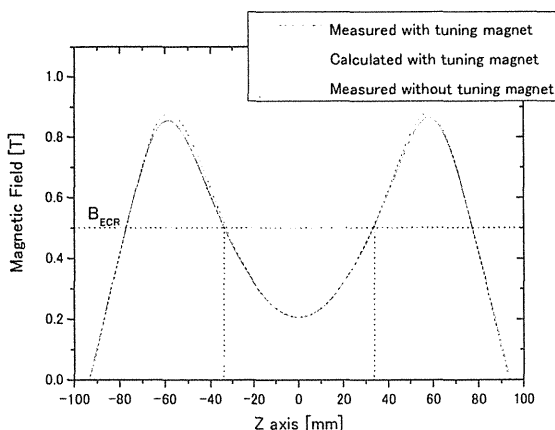


Fig.3 Axial magnetic field distribution.

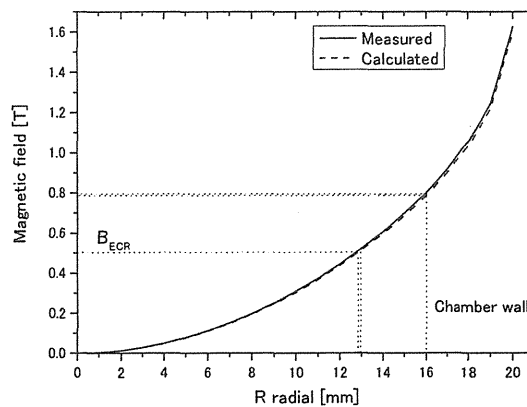


Fig.4 Radial magnetic field distribution.

Without the mirror tuning magnets, the measured resonance length is 90 mm, and the measured magnetic flux densities are $B_{\text{MAX}}=0.80\text{T}$ ($1.6B_{\text{ECR}}$), $B_{\text{MIN}}=0.32\text{T}$, $B_{\text{MAX}}/B_{\text{MIN}}=2.5$.

2.2 Microwave generator and plasma chamber

A DRO (Dielectric Resonator Oscillator) of microwave oscillator has been chosen because the frequency stability is high and noise is very low. The microwave is amplified by a TWT (Traveling Wave Tube) with the maximum power of 125W.

The plasma chamber made of a SUS316 has double pipe structure for cooling water, and its outer diameter is 38.5mm and inner diameter 32mm.

3. Schedule

Next year, operations and improvement will be carried out to generate highly charged ion and to realize the high stability.

References

- 1) S. Okumura, K.Arakawa, M.Fukuda, Y.Nakamura, W.Yokota, T.Ishimoto, S.Kurashima, I.Ishibori, T.Nara, T.Agematsu, H.Tamura, and A.Matsumura, "Temperature control of a cyclotron magnet for stabilization of the JAERI AVF cyclotron beam", Proc. 16th Int. Conf. on Cyclotron and their Applications, East Lansing, USA, 330 (2001).
- 2) T. Nara, W.Yokota, Y.Nakamura, M.Fukuda, T.Agematsu, S.Okumura, I.Ishibori and K.Arakawa, "Status of ECR ion Source at JAERI", Proc. 9th Symp. on Accelerator Science and Technology, Tsukuba, Japan, 89 (1993).

9.8 Installation of Cooling Panel for Cyclotron Stabilization

Y. Nakamura*, K. Takano**, To. Yoshida** and Y. Arakawa**

Advanced Radiation Technology Center, JAERI*

Beam Operation Service, Co., Ltd.**

1. Introduction

Various ion beams extracted from the JAERI AVF cyclotron almost have been delivered constantly for a long time because the measures for beam stabilization were already carried out ¹⁾⁻³⁾. However, the hottest room temperature near the cyclotron bottom often rises up to 33 °C at the season when the air-conditioner is not worked fully, especially in late spring and autumn.

A small possibility is predicted that high temperature may affect to beam stability. During more than ten years, several additional devices such as a flat-top system, a new gradient corrector, an exclusive cooling system for beam stabilization, etc. have been installed in the cyclotron pit room. As the result, the room temperature in the pit room at basement increases gradually.

An outline of ventilation system surrounding the cyclotron is illustrated in Fig. 1. Fresh air is supplied into the cyclotron vault from the rectangular duct on the shielding wall, then is transferred to the pit room through narrow gaps around the cyclotron, finally is exhausted from the ducts in the pit room and the cable distribution room. And two heat-pump package controllers (HPC's) are operated independently. In addition, a part of the warmed air above the pit room is sucked by added four blowers, then is returned once to the cyclotron vault. The other air is also put back directly to the HPC again.

So far, it was rather difficult to do the maintenance work because several large ducts were laid on the floor around the cyclotron. The suppression of the temperature rise by operation

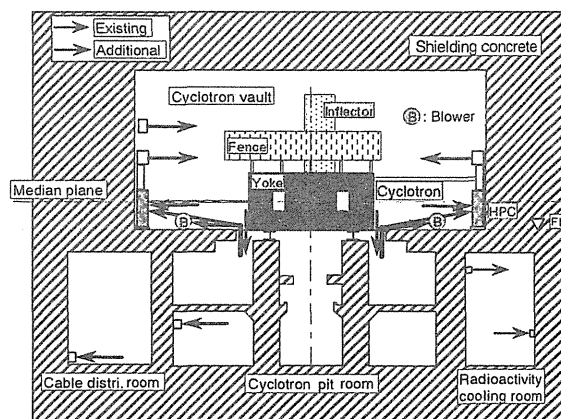


Fig. 1 Outline of air ventilation surrounding the cyclotron.

of this blower system was estimated to be only 1.0 °C or less in comparison with the stopping condition. Finally, we concluded that the blower system was not so effective.

Therefore, in order to avoid the influence to the cyclotron at least, we installed the cooling panels within a residual space as wide as possible in the cyclotron bottom where has been already equipped with many devices, pipes, cables and so on.

2. Temperature in Cyclotron Vault

Room temperature in the cyclotron vault is always set up at 25 °C through a year. An amount of ventilation air is about 7000 m³/h and relative humidity changes from 20% to 50%. Figure 2 shows a typical temperature deviation for last ten days every three months among the four seasons. Actually, average room temperature in the vault slightly fluctuates in the range of 23-26 °C through a year. Furthermore, it obviously seems that the room temperature increases about 0.7-1.1 °C at

the middle of a week since our cyclotron system has been usually operated continuously from Monday morning to Friday evening.

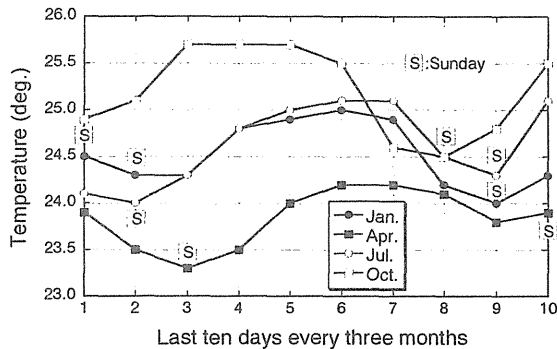


Fig. 2 Typical average temperature through the season in the cyclotron vault.

3. Temperature Condition around Cyclotron

The temperature condition around the cyclotron is foreseen as shown in Fig. 3. Upper and lower yokes of the cyclotron are insulated thermally from the main coil stack by the water cooling jacket controlled at 22-25 °C according to the exciting current. Twelve pairs of trimming coils are also controlled constantly at 25.5 °C independent of the exciting condition by the exclusive cooling system. Taking into account these states, the water temperature in the cooling panel should be regulated at 23-24 °C. By means of installation of the cooling panels, the symmetrical condition for temperature distribution can be achieved approximately.

In regard to the room temperature rise up to 33 °C at the cyclotron bottom as mentioned before, we estimated simply the amount of heat transfer to the cyclotron yoke. If an average heat transfer coefficient is 10 W/m²K for natural heat convection, the quantity of input heat to the lower yoke is calculated at about 1.5 kW since the effective surface area around the bottom is 21 m² and the temperature difference between the yoke surface at 26 °C and surrounding warmed air is 7 °C. Assuming the continuous operation of 100 hours for a week and complete adiabatic

condition, the temperature rising of the cyclotron weighed at 220 tons is converted into 6 °C for the same period. This condition may be a little serious problem for cyclotron stabilization. Therefore, it is required to remove the extra heat by installation of the cooling panels.

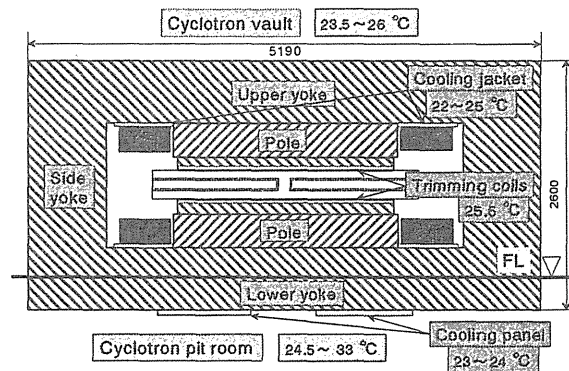


Fig. 3 Temperature condition around the cyclotron.

4. Installation of Cooling Panel

The cooling panel is thin box whose thickness is 20 mm, is formed inside the fifth folded water path. This panel which has no pressure-tight function is made of SUS 304 stainless steel with the simple structure of welding. Four panels with two shapes are 960 × 600 mm and 960 × 320 mm wide, respectively. The weight of the larger panel is about 35 kg without cooling water. Each of four panels was fitted up certainly by six steel bolts after the processing of screwed holes into the lower yoke as shown in Fig. 4. Moderate

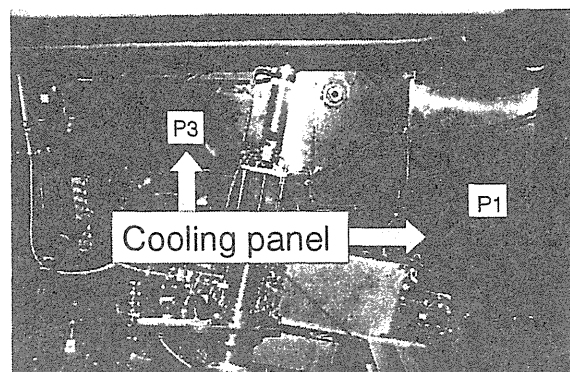


Fig. 4 Two (P1 & P3) of the four cooling panels installed below the cyclotron bottom.

silicon sealant was inserted between the panels and yoke to keep good heat conduction. The installation work for cooling panels was rather hard because of narrow space and upward posture.

A system outline of the cooling panel is illustrated in Fig. 5. Cooling water is fed by the cooling water circulation device “EYELA CA-1112” with the buffer tank of 16.5 L and the cooling capacity of 1.5 kW at 25 °C. Individual device was connected using the pressure-resistant rubber hose and socketless-hose metal fitting. For the purpose of moving the circulation device, a pair of quick couplers flowed through the cooling water were equipped with outlet and inlet ports.

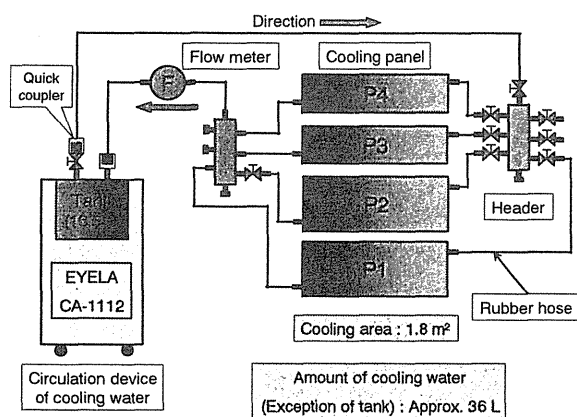


Fig. 5 System outline for cooling panel.

The amount of cooling water is roughly 36 L with the exception of the tank. The whole flow rate is about 8.7 L/min and the effective cooling area in the cyclotron bottom is about 1.8 m².

5. Future Plan

We are going to make sure the effect of the cooling panel under actual cyclotron operation. If these panels are effective for beam stabilization, additional panels will be able to be installed elsewhere.

Acknowledgment

Authors wish to thank Mr. H. Takada for the supply of original data and some information about the ventilation system.

References

- 1) Y. Nakamura, S. Okumura, *et al.*, TIARA Annual Report 1999 (JAERI-Review 2000-024) pp. 282-284
- 2) S. Okumura, S. Kurashima, *et al.*, Proc of 13th Sympo. Accel. Sci. Technol., Suita, Osaka, Japan (2001) pp.283-285
- 3) S. Okumura, S. Kurashima, *et al.*, TIARA Annual Report 2000 (JAERI-Review 2001-039) pp. 290-292

9.9 Inverter Chain Driving System for the 3MV Tandem Accelerator

K.Mizuhashi*, A. Chiba*, M.Ishii**, T.Kitano**, S.Kanai** and S. Tajima*

Advanced Radiation Technology Center, JAERI*
Beam Operation Service, Co., Ltd.**

1. Introduction

TIARA 3 MV tandem accelerator has been operating for over ten years. On the other hand, it had some problems as follows. 1) Dust dispersed by chain driving was much quantity. After three months operation, the inside the accelerator tank has covered by the black dust like the inside of a chimney. As the dust becomes a cause of the discharge in the tank, it makes accelerator operation unstable. 2) Sound noise in pellet chain running was about 95dB in the accelerator room. It is not good for work environment when we check the machine in the accelerator room. 3) Stability of the terminal voltage was not enough for the beam analysis experiment. The stability in normal operation was over 3×10^{-4} (FWHM). This is not so good for the position stability of beam and the intensity fluctuates on the target.

In order to solve these problems, the pellet chain drive system was improved into the inverter drive.

2. Outline of the improvement

Before the improvement on the pellet chain driving system, it was directly operated by the commercial electric power (210V, 50Hz). In this case, the chain speed was fixed, because the rotational number of the motor is decided by the frequency of an electric power. The rotation speed of induction motor is shown by following

equation $N=120f/(p(1+s))$ (rpm). Where, f is a frequency, p is the magnetic pole number of a motor (6 poles), s is a slip factor (about 5%). The other side, an inverter can change a frequency of the electric power and arbitrarily control a speed of the pellet chain. By choosing the optimal speed, it was considered that the problems described in the top could be solved. In addition, we had to perform some measures to remove the electric noise, because the inverter was a noise source for the other electrical measuring instrument. At present, the inverter system can be stably operating without noise problem.

3. Features of the inverter drive system

The charging current to the high voltage terminal is dependent on the pellet chain speed and the electric charge of a pellet. The charging quantity of a pellet is dependent on the CPS (charging power supply) voltage. Therefore, the charging current is expressed in equation (1).

$$I_c = K \times V_{cps} \times S_{chain} \cdots (1)$$

Where, I_c is the charging current (A), K is a constant value that is the inductive charge of a pellet per unit voltage (C/V), V_{cps} is the CPS voltage (V) and S_{chain} is the chain speed that means the numbers of pellet per one second (n/s).

3.1 Load current

The load currents of the chain motor to obtain the same terminal voltage were measured by changing the frequency of the inverter. It is proven that the load current is smaller when the chain speed is low (Fig. 1). The load current at 30Hz driving is about 1A less than it at 50Hz driving. This result shows that a stress of chain is also small at the low-speed operation. Although a life of the chain with normal operation is the about

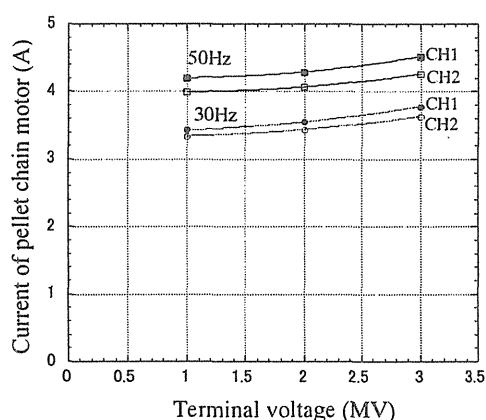


Fig.1 Load current of pellet chain motor

20,000 hours, it will be extended by choosing suitable chain speed.

3.2 Inductor volt

From the equation (1), the relation between chain speed and CPS voltage is in inverse proportion at the same charging current. Therefore, CPS voltage must be higher to get the same terminal voltage when the chain is operated at lower speed (Fig.2). From this fact, the low-speed operation by the inverter is impossible with the accelerator without sufficient capacity of the pellet chain charging system. Therefore, it is desirable that the machine has over two chains system for the low-speed operation.

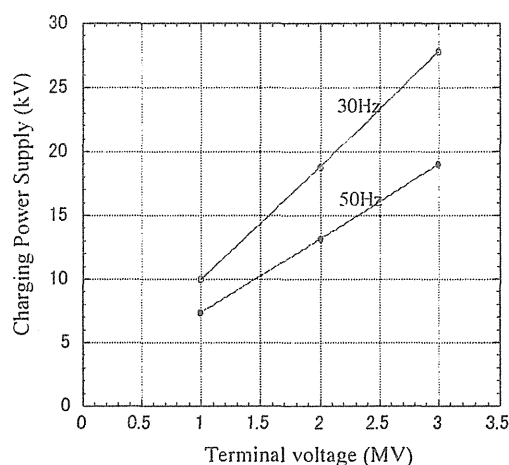


Fig. 2 Characteristic of the charging system

4. Result of the improvement

Results for the remodeling purpose are as follows.

4.1 Dust problem is solved

The friction of sheave and chain is decreased by low-speed operation of the chain. The other hand, the slip between sheave and chain in the starting was improved by the slow starting function of the inverter. The time until it reaches the steady speed from the chain starting is the 40 seconds. Therefore, the rapid load is not applied to the chain at the moment of the starting by this function. By these two effects, it is considered that the generation of the dust decreases. The quantity of the dust was reduced about 1/10 by 70% (35Hz) speed operation. This generation rate of the dust can be allowed in the pellet chain type accelerator and the frequency of discharge in the tank decreased.

4.2 Work environment is improved

When the chain was operated by full speed (50Hz), the sound-noise level was 95dB at accelerator room, but it decreased to 87dB at 70% speed operation in the accelerator room (Fig.3). In addition, as the

performance test of charging system is done near the running chain in the outside of the tank, the safety for the staffs for this test is ensured by the slowing speed operation of the chain.

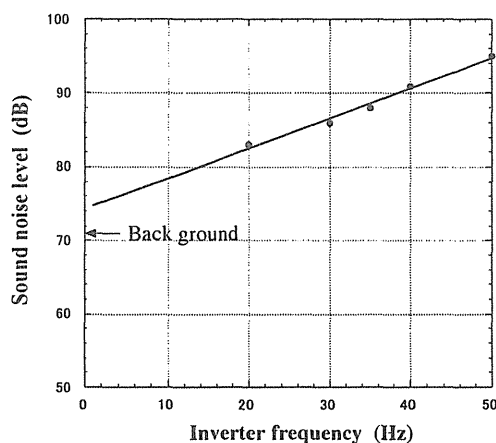


Fig.3 Characteristic of the noise

4.3 Stability of the terminal voltage is improved

Figure 4 shows that the stability of terminal voltage is improved by changing chain speed. This phenomenon is considered as follows. The CPO (Capacitive Pick Off) signal is used for the feedback of the voltage

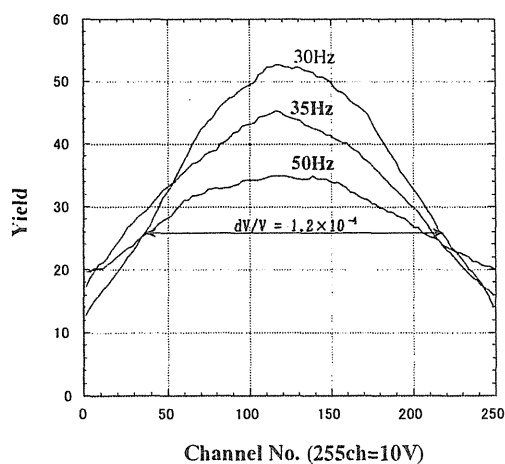


Fig.4 Stability of the terminal voltage (at 3MV)

stabilization and influenced by the mechanical vibration of the terminal. The mechanical vibration is dependent on the chain speed and condition. Therefore, it is considered that the stability improves when the chain speed slows down. The frequency components of the CPO signal are shown in Fig.5. In this figure, there are two peaks of 15.8Hz and 9.5Hz in this figure. These peaks are correspondent to the rotational number of the chain motor when the inverter output frequencies are at 50Hz and 30Hz respectively. It is proven that the frequency component in the region near 10Hz has been improved when the chain speed is low (30Hz). Such low-frequency components in the CPO signal seem to be the effect of the terminal vibration.

At the 60% chain speed, the stability has been improved to about 67% for the full speed of it in Fig. 4.

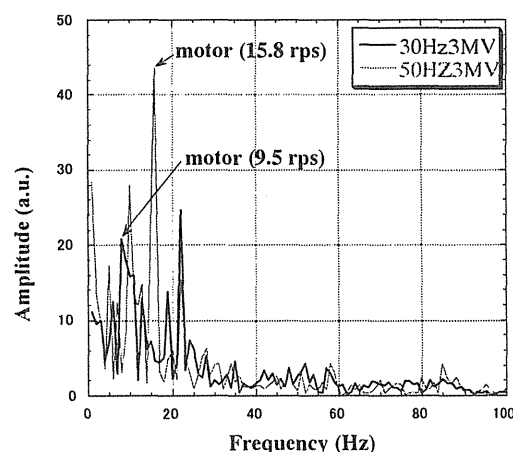


Fig. 5 Frequency components of the CPO signal

5. Conclusion

The inverter which feeds variable frequency power to motor drive is effective for the pellet chain type accelerator, and some peculiar problems with the accelerator for the long time was improved.

9.10 Development of Beam Current Stabilization System using Wire Type Beam Attenuator

K.Ohkoshi, A.Chiba, K.Mizuhashi and S.Tajima
Advanced Radiation Technology Center, JAERI

1. Introduction

A variety of ions from H^+ to Bi^+ have been available for various experiments by means of a 400kV ion implanter equipped with a Freeman ion source¹⁾ in TIARA facility²⁾. However, since the surface state of the sample in the source gradually changes, it is difficult to generate solid ions such as a metal and a fullerene(C_{60}) stably for a long time³⁾. Instability of the beam current is a cause of the irradiation dose error to the target. Therefore, we developed a system to keep a constant beam current using a wire type beam attenuator, and we achieved below $\pm 3\%$ of the beam stability by this system.

2. Wire Type Beam Attenuator

Usually, a double slit is used to adjust beam current for the irradiation. It consists of two pairs of the metal blocks, and a position of each block is controlled in order that it may adjust beam current. However, since the cross-sectional shape of the beam changes depending on current intensity, it is not suitable for the beam current stabilization system.

Therefore, we developed the wire type beam attenuator. It adjusts the beam current by changing the density of thin metal wires in the beam. The schematic diagram of the double slit and the wire type beam attenuator are shown in Fig.1.

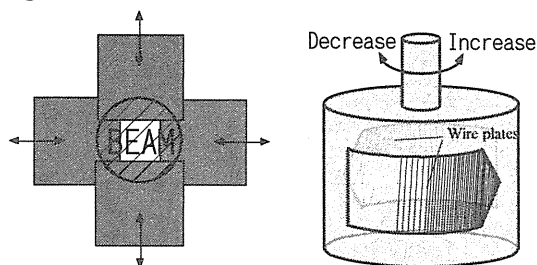


Fig.1 Schematic diagram of the double slit and the wire type beam attenuator.

The wire plates are installed in the window of the front-side and rear-side of the cylinder. The wire plate consists of five wire interval patterns shown in Fig.2. The first space of 30mm in width is not wire, and the beam

passed through there without decreasing. The density of a wire on the plate is gradually increased in 5, 10, 15 and 20 (wires/10mm) as it goes to the right. The size of width and thickness of the wire are 0.2mm and 0.3mm, and the quality of material is stainless steel. The wires are aslant attached on the plate, and the plates are symmetrically installed on the both side of the cylinder.

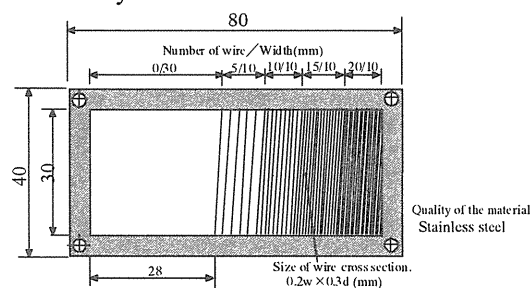


Fig.2 Scheme of the wire plate.

When the attenuator is rotated to decrease direction, the number of the wire beam in the beam region gradually increase. And since the front wires overlap the rear wires, the many lattices are formed by the both wire plates at the beam area. Figure 3 shows the wire position of the front and rear side when the attenuation rates are 0% and 30%.

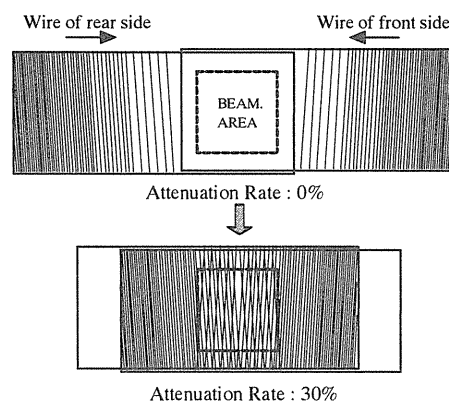


Fig.3. Wire position of front and rear side when attenuation rate are 0% and 30%

If the attenuator is rotated more, the attenuation rate will become large linearly. The relation between the angle of the attenuator and Ar^+ beam current is shown in Fig.4.

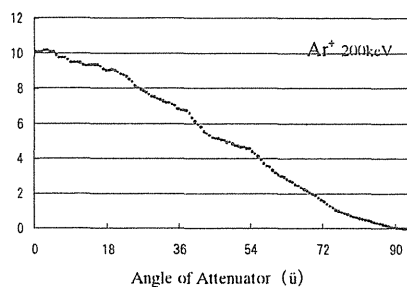


Fig.4 Relation between the angle of the attenuator and beam current.

The beam shape was checked by a beam profile monitor(BPM) when the attenuation rate are 0% and 50%. Consequently, the beam shape hardly changed at 0% and 50% of attenuation rate as shown in Fig.5. The range of H^+ ion at 500keV in the stainless steel is about $2.5\mu\text{m}$. Therefore, the thickness of the wire, $300\mu\text{m}$ is enough to prevent the skinny beam to the target.

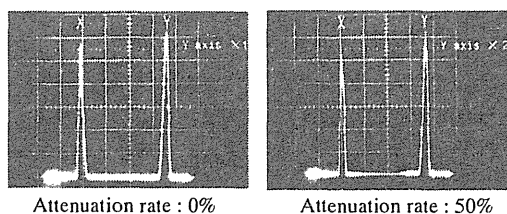


Fig.5 Cross-sectional shape of beam when attenuation rate are 0% and 50%.

3. Beam Current Stabilization System

The beam current stabilization system consists of the wire type beam attenuator, the control PC and a transparent-type beam current monitor⁴⁾. An irradiation beam current value(setting value) is inputted into the control PC. The beam current measured by the target beam monitor or the transparent type beam monitor is read into the control PC, and it is compared with the setting value. The wire type attenuator is controlled by the difference of them to become beam current to the setting value. The scheme of the beam current stabilization system is shown in Fig.6.

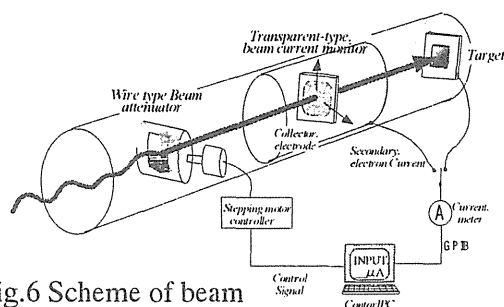


Fig.6 Scheme of beam current stabilization system.

4. Experiments and Results

The wire type beam attenuator was attached in the beam line connected to the 400kV Ion Implanter. And a demonstration was carried out using C_{60}^+ , 200keV beam. The target beam current was measured by a Faraday cup(FC I-2). The setting value was set as $1.0\mu\text{A}$, and the attenuator will be controlled when the difference of the target current and the setting value become 1% of setting value or more. When the stabilization system is off, the beam current was unstable, because it is caused from the ion source. However, by working this system, it was able to supply stable beam of about $1\mu\text{A}\pm 3\%$. The schematic diagram of the experimental set up and the result are shown in Fig.7 and Fig.8.

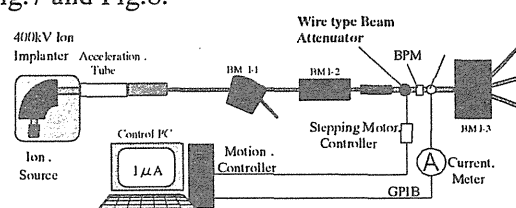


Fig.7 Schematic diagram of experiment set up.

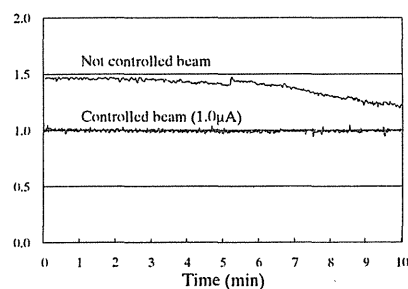


Fig.8 Result of the beam current stabilization system experiment.

5. Summary

The unstable beam mainly caused by the ion source was able to be stabilized by this system. By having developed the wire type attenuator, it was possible to decrease or increase beam current without continuously changing cross-sectional shape of the beam.

References

- 1) J.H.Freeman, Nucl. Instrum. Methods 109, p477 (1973)
- 2) Y.Saitoh, S.Tajima et al., Nucl. Instrum. Methods phys. Res. B89, 23 (1994)
- 3) K.Ohkoshi, Y.Saitoh et al., JAERI-Review 2003-033, 323-324
- 4) Y.Nakajima, Y.Saitoh and S.Tajima, JAERI-Review 2000-024, 280-281

9.11 Automatic Measurement of Beam Energy Spread for JAERI Single-ended Accelerator II

Y. Ishii, A. Chiba, T. Sakai and I. Takada

Advanced Radiation Center, JAERI

1.Introduction

A measurement technique of beam energy spreads using resonance nuclear reactions with small reaction spreads within 200 eV has been developed as one of the precise measurement ones¹⁾. Energy spreads of the proton (H^+) beams produced by 3MV Single-ended Accelerator have been measured using the measurement technique with resonance nuclear reactions of $^{27}Al(p, \gamma)^{28}Si$ and $^{24}Mg(p, \gamma)^{25}Al$. Proton beams, in the measurement technique, were injected in aluminum (Al) or magnesium (Mg) targets, changing their beam energy on the basis of applying suppression voltage up to 5 kV to the targets. The suppression voltage was, however, manually applied step by step in a voltage between 50 V and 500 V. Since each measurement time in a series of suppression voltages from 0 V to 5 kV was over 5 min, a series of total measurement time took over 2 hours. Thereby the measurement technique was carried out only if a beam energy spread was almost constant for the series of total measurement time.

A method of applying scanning suppression voltage controlled by an external function generator to the targets using a part of micro-PIXE system²⁾ (scanning suppression method) was introduced in order to include slow fluctuations with a period of over 30 minutes into a beam energy spread. The method led us to change proton beam energy finely and continuously by applying the scanning suppression voltage to the targets between 0 V and 5 kV. In the previous work, the result of beam energy spread measurement

demonstrated that slow fluctuated beam energy spreads could be included into its result at beam energy of 2.4 MeV³⁾. In this work, beam energy spreads at a series of beam energy, 0.992, 1.317 and 2.010 and 2.400 MeV, were measured using the scanning suppression method.

2.Experimental Setup

The experimental chamber for using the scanning suppression method was connected to the zero-degree beam line of Single-ended Accelerator as shown in Fig.1.

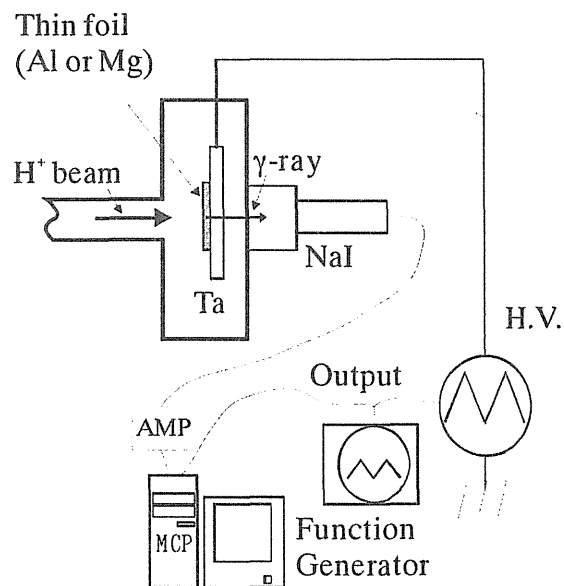


Fig.1 Schematic diagram of the experimental setup

Aluminum and magnesium thin foil with thickness of 60 nm and 100 nm evaporated on a Tantalum of 10x20 cm were used as targets, respectively. A 2.5 inch NaI γ -ray detector was placed to the forward direction to injection beam because the γ -ray emissions of the

resonance reactions have the forward directivities. A power supply for the suppression voltage was controlled by a function generator. The γ -rays of nuclear reactions were detected with the NaI detector. The signals of the NaI were accumulated in a PC through a multi channel analyzer (MCP). A γ -ray yield was counted in the range of the γ -ray energy of 50 keV centering the γ -ray energy set between lower and upper roi s.

3.Measuement result and Summary

Curves of γ -ray yield at beam energies of 0.992, 1.317, 2.010 and 2.40 MeV were measured as a function of injection beam energies. One of the curves to the beam energy at 1.317 MeV is shown in Fig.2.

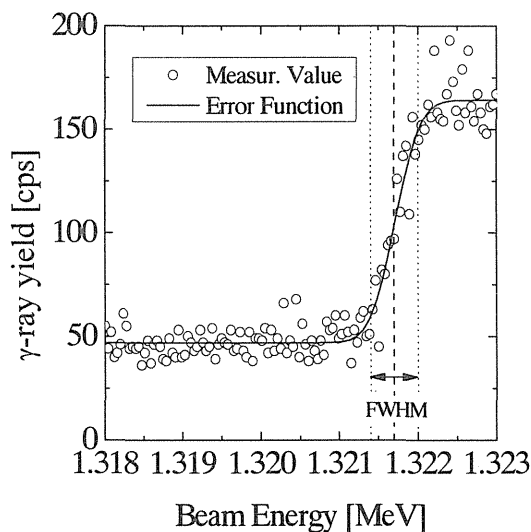


Fig.2 One of the measurement results at the injection beam energy of 1.317 MeV.

Each measurement point in the curve shows an integration of γ -ray yields. Thereby beam energy spreads were estimated by fitting an error function which is represented as

$$y = \frac{2}{\sqrt{\pi}} \int_0^x e^{-u^2} du,$$

on the basis of assuming that the energy ones were Gaussian distribution. Where x and y are parameters and u is an integration parameter. The beam energy spreads measured by the scanning suppression method were defined as a Full Width at Half Maximum (FWHM) of Gaussian distribution. The estimated results of beam energy spreads (ΔE) are listed in Table -1. The Stability of beam energies is also written in Table-1 as a ratio of the energy spread to the beam energy. The stability values are minimized at 1.317 and 2.010 MeV. One of the reasons of the values minimized at these beam energies is that the controller of the accelerator is adjusted at 2.00 MV because the accelerator is mainly used around 2 MV.

Beam energy spreads at the serious of beam energy were measured using the scanning suppression method. The stability of the incident beams was estimated from the spreads. Since the spreads and the stability included the slow fluctuations, the stability is close to the real beam one.

Table-1 Beam energy spreads estimated from fitting the measurement value using an error function and beam energy stability from the beam energy spread.

Beam Energy [MeV]	0.992	1.317	2.010	2.400
Beam Energy Spread $\Delta E(\text{FWHM})$ [eV]	698	598	897	1296
Stability $\Delta E/E$ [$\times 10^{-4}$]	7.0	4.5	4.5	5.4

Reference

- 1) Y.Ishii, et. al, JAERI-Review 2001-39
- 2) T.Sakai, et. al, Nucl. Instr. and Meth. B136-138(1998)390

9.12 Renewal of Control System for the 3MV Single-ended Accelerator

S.Uno*, A.Chiba*, T.Takayama**, M.Kouka**, I.Takada* and S.Tajima*

Advanced Radiation Technology Center, JAERI*
Beam Operation Service Co., Ltd.**

1. Introduction

The 3MV single-ended accelerator has been worked for about ten years since installation. And the control system of this accelerator was improved to respond various experimental requests of the users. But it had been difficult for this control system to solve several problems, for example, it could not adapt to equip high brightness ion source, we had not get any spare parts, and it was also unable to repair by maker.

Therefore, we have renewed control system for this accelerator in order to have the ability for the new ion source, and operate smoothly without any troubles of the control system.

2. Control system overview

An old control system consisted of a workstation, x-terminal and VME bus apparatus. This workstation ran the UNIX, and the VME CPU ran a real-time operating system VxWorks^{®1}, due to they could improve response speed of the operation for accelerator. However it was trite capability compared with performance of a recent personal computer.

The schematic diagram of the new control system constitution is shown in Fig. 1. Three personal computers comprise a control system, which are interfaced to the programmable logic controllers (PLC) by network of Ethernet. These personal computers run the Linux operating system

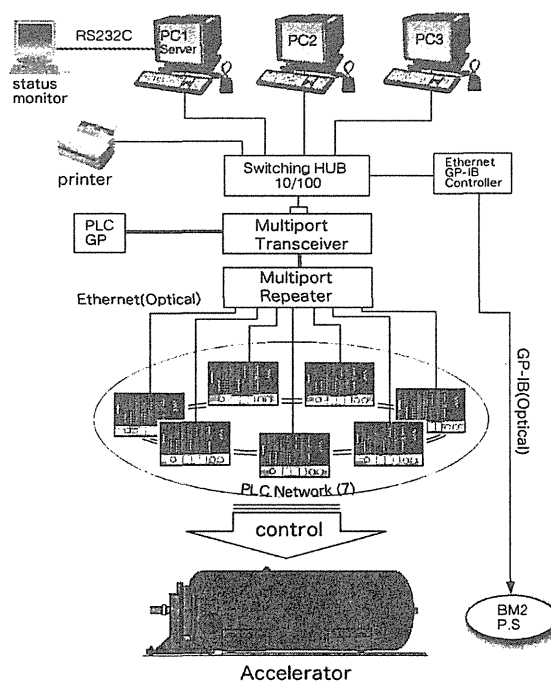


Fig. 1. Schematic diagram of the new control system.

and they act necessary task such as network management, transmitting of status information to a workstation for status monitor and the graphic panel. Additionally these computers are performing to operate the accelerator as man-machine interface.

This control system has seven PLCs, which were utilized previously. The PLCs at each room are connected with the computers at control room by optical fiber of Ethernet, because they protect signals on the network against electromagnetic noises. The power supply of analyzing magnet (BM2) is controlled directly at the computers via GP-IB interface to achieve by high resolution control.

3. Software features

We have included various functions in the software for control of accelerator based on the operation experience for about ten years, such as some control screens, data loggings, and trend recording. These functions were considered they could be use easily for operators. The database system, which is used parameter management of devices, was replaced to the InterBase^{®2}. Therefore, this system has made easy to respond for change and addition of apparatus.

The principal functions of software are shown in Fig.2. The programs are developed using the Kylix^{®2}. All functions of software are started by selecting each item on the launcher window as show in ① in Fig.2. General operation for parameters can control using the graphic window which

disply all devises as show in ② in Fig.2, and the character window which collects and displys only devices required for specific operations as show in ③ in Fig.2. The trend recording window indicates four signals and sampling are changed from 0.5sec to 6sec at intervals of time. The data logging function store all parameters, and also output setting them as values for the devices. The calculation of magnet parameter function computes magnetic field and load current corresponding the specific beam condition, and the results are automtstically setting to the magnets.

In addition, the new system has scaling and automatic high voltage conditioning functions and so on, to secure effective and smooth accelerator operation.

@1 VxWorks is a product of WindRiver Systems.

@2 These are a product of Borland Software Co..

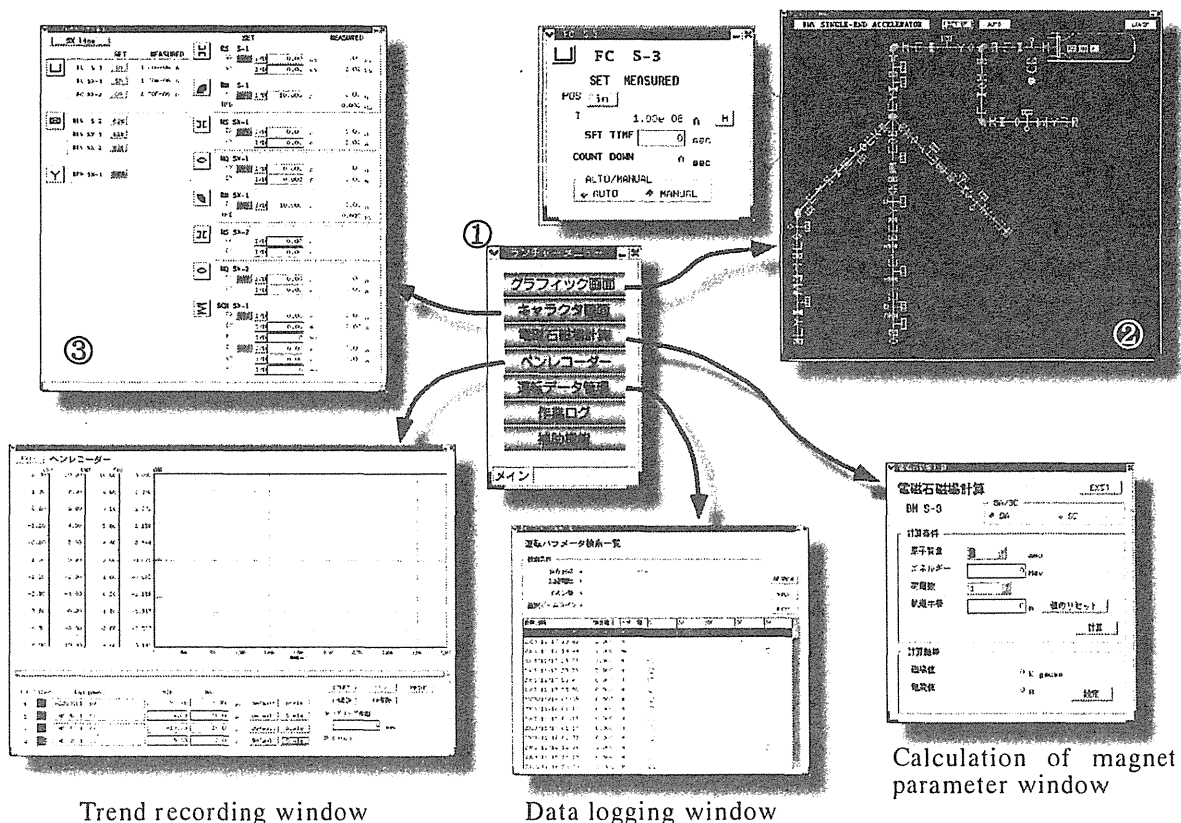


Fig. 2. Schematic of the control functions.

9.13 Beam Chopping System for Cluster T.O.F. Measurement in 3 MV Tandem Accelerator

Y. Saitoh, A. Chiba and K. Mizuhashi
Advanced Radiation Technology Center, JAERI

1. Introduction

It was revealed that the intensity of secondary ions with MeV energy cluster ion irradiation was higher than that with single ion irradiation as cluster effect. So the time of flight (T.O.F.) surface analysis to which the cluster effect mentioned above is applied is being developed¹⁾. For the T.O.F. analysis, we manufactured a beam chopping system to make a pulsed cluster beam and set it at the upper stream of the tandem accelerator shown in Fig. 1. The beam chopping system consists of electrostatic deflection plates (chopper), beam slits, a high voltage power supply and a pulse generator. The system was operated at a frequency from 5 kHz to 10 kHz. The pulse width and the number of ions in a pulse are important parameter for a quantitative analysis. So far those values deduced from DC current of cluster beam, a chopping frequency and FWHM of a hydrogen peak in a measured T.O.F. spectrum²⁾. We measured those values directly using particle detector (MCP, SSD) and verified that the deduced values almost corresponded to the measured one.

2. Experiments and Results

The measurements were carried out using C_8 ions in the energy of 0.5MeV/atom at a chopping frequency of 8 kHz.

The pulse width was measured with the T.O.F. system²⁾. A direct cluster ion signal detected with MCP was used as a stop pulse of a TAC circuit in stead of the secondary ion signal²⁾. After tuning the beam transport, the minimum pulse width measured 160 nS. This is the almost same value with the deduced one.

The number of cluster ions in a pulse was directly measured with a SSD detector shown in Fig. 1. The beam current before being chopped was 10 pA and a pulse width was 160 nS (These are a usual beam condition of C_8 beam). As a result, the measured average number of cluster ions in a pulse beam was 11.6 ions and the calculated value was 10 ions in a pulse.

So the deduced values are useful for usual experiments.

References

- 1) K. Hirata, et al. Appl.Phys. Lett. 83 p. 4827.
- 2) H. Shibata, et al. JAERI-Review 2003-033, p. 303.

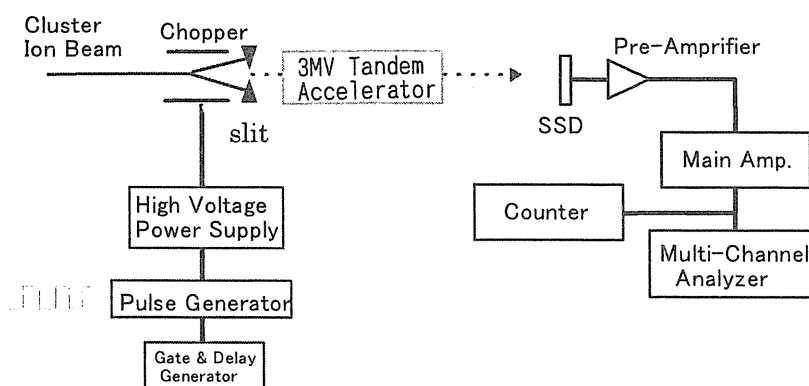


Fig. 1. Beam chopping system and beam measurement system

10. Status of TIARA 2003

10.1	Utilization of TIARA Facilities	333
	Su. Tanaka, K. Nishimura, H. Kaneko, M. Hosono, H. Watanabe, H. Tachibana, S. Mochizuki, S. Kaneya, K. Daikubara, M. Kawabata and M. Iijima	
10.2	Operation of JAERI AVF Cyclotron System	336
	Y. Nakamura, T. Nara, T. Agematsu, I. Ishibori, S. Kurashima, K. Yoshida, M. Fukuda, S. Okumura, N. Miyawaki, S. Tajima, K. Akaiwa, To. Yoshida, S. Ishiro, Y. Arakawa, Tu. Yoshida, S. Kanou, A. Ihara and K. Takano	
10.3	Operation of the Electrostatic Accelerators	337
	K. Mizuhashi, S. Uno, K. Ohkoshi, A. Chiba, I. Takada, S. Tajima, Y. Saitoh, Y. Ishii, T. Sakai, M. Ishii, T. Orimo, T. Takayama, M. Kouka, A. Ohmae, T. Kitano and S. Kanai	
10.4	Radiation Control & Radioactive Waste Management in TIARA	338
	Safety Division & Utilities and Maintenance Division Department of Administrative Services, JAERI	

This is a blank page.

10.1 Utilization of TIARA Facilities

Su. Tanaka*, K. Nishimura*, H. Kaneko*, M. Hosono*, H. Watanabe**,
H. Tachibana**, S. Mochizuki**, S. Kaneya**, K. Daikubara***,
M. Kawabata**, M. Iijima**

Advanced Radiation Technology Center, JAERI*

Radiation Application Development Association**

Research Center for Nuclear Science and Technology, The University of Tokyo***

1. Introduction

TIARA is a center of the ion accelerator facilities composed of four ion accelerators, the AVF cyclotron, the 3MV tandem accelerator, the 3MV single-ended accelerator, and the 400kV ion implanter. These accelerators have been fully served for ion beam applications since January 1994.

2. Utilization system

TIARA is opened for public use: it receives applications of the experimental subjects in wide areas once a year from outside users as well as JAERI staffs. The subjects and the allocated beam time are approved after the official investigation by Subcommittee for TIARA under Advisory Council for JAERI's Research Facilities, which has been organized since 1999. To attain an effective outcome of the research program, the beam time of each accelerator is fairly allotted to the subjects three times in a year based on the approved beam time.

Charges for the utilization are remitted in the case that a contract of the joint research between

JAERI and a university or a company or that of the projective joint research between JAERI and universities is made. However, the results of research have to be published at the TIARA Research Review Meeting and in the JAERI TIARA Annual Report. There is another system of visitor use with charges but without the publication duty.

3. Experimental subject approved

Number of experimental subjects using cyclotron approved in FY2003 was 57 while the total number using three electrostatic accelerators was 51 as shown in Table 1. Table 2 shows the number allotted to users under various contracts.

Fig. 1 shows the change of number of experimental subjects in various research fields from FY1991 to FY2004.

4. Allotted time to users

The cyclotron has been continuously operated from Monday to Friday. The utilization time for the cyclotron is allotted in units of an hour.

Table 1 Number of experimental subjects in FY2003 at various research fields.

Accelerators Fields of research	Number of subjects	
	Cyclotron	Electrostatic accelerators
Materials for space	6	7
Materials for fusion	1	6
Biotechnology	36	1
Inorganic material	0	22
RI & nuclear sci.	3	0
Organic material & Radiation chemistry	6	1
Basic technology	5	14
Total	57	51

Table 2 Number of experimental subjects in FY2003 at various relations with users.

Accelerators Relations with users		Number of subjects	
		Cyclotron	Electrostatic accelerators
JAERI only	Takasaki Establishment	10	9
	Others	1	9
Cooperative research with university		17	13
Joint research project		11	16
Joint research with private company or governmental institute		18	4
Total		57	51

In case of the electrostatic accelerators, on the other hand, the utilization time is allotted in units of a day either from 9 a.m. to 7:30 p.m. (A mode), or from 9 a.m. to 10 p.m. (B mode).

As shown in Table 3 and Fig. 2, the cyclotron was used in the various research fields, while the electrostatic accelerators were mainly

used in the field of inorganic materials and materials for fusion. The ratios of allotted time for JAERI staffs to total utilization time were 32% for the cyclotron and 41% for the electrostatic accelerators as shown in Table 4 and Fig. 3.

Table 3 Utilization of the accelerators in FY2003 at various research fields.

Accelerators Fields of research	Utilization time at each period															
	Cyclotron (hours)				Tandem accelerator (days)				Single-ended accelerator (days)				Ion implanter (days)			
	02-1	02-2	02-3	total	02-1	02-2	02-3	total	02-1	02-2	02-3	total	02-1	02-2	02-3	total
Material for space	164.5	146	151.5	462	14	9	9	32	0	2	0	2	14	17	11	42
Material for fusion	0	31	12	43	11	11	7	29	9	7	6	22	4	5	4	13
Biotechnology	349.5	313	143	805.5	2	2	2	6	0	0	0	0	0	0	0	0
Inorganic material	0	0	0	0	11	13	14	38	12	15	23	50	25	23	24	72
RI & Nuclear science	30	31	17	78	0	0	0	0	0	0	0	0	0	0	0	0
Organic material & Radiation chemistry	84	91	93	268	4	4	4	12	0	0	0	0	0	0	0	0
Basic technology	84	122	96	302	8	6	8	22	24	25	20	69	0	0	0	0
Machine study	107	115	82	304	3	3	3	9	5	5	1	11	4	5	1	10
Charged use	96.5	141	42	279.5	4	4	3	11	0	0	1	1	1	2	5	8
Total	915.5	990	636.5	2542	57	52	50	159	50	54	51	155	48	52	45	145

Table 4 Utilization of the accelerators in FY2003 at various relations with users.

Accelerators Relation with users		Utilization time at each period															
		Cyclotron (hours)				Tandem accelerator (days)				Single-ended accelerator(days)				Ion implanter (days)			
		02-1	02-2	02-3	total	02-1	02-2	02-3	total	02-1	02-2	02-3	total	02-1	02-2	02-3	total
JAERI	Takasaki Establishment	172	167	159	498	17	13	15	45	6	9	10	25	13	14	9	36
Only	others	3	6	4	13	5	6	5	16	9	9	7	25	3	4	5	12
Cooperative research with universities		180	154.5	103	437.5	5	5	4	14	6	5	13	24	19	17	18	54
Joint research project		195	245	127	567	19	17	18	54	24	24	19	67	5	6	5	16
Joint research with company or governmental institute		162	161.5	119.5	443	4	4	2	10	0	2	0	2	3	4	2	9
Machine study		107	115	82	304	3	3	3	9	5	5	1	11	4	5	1	10
Charged use		96.5	141	42	279.5	4	4	3	11	0	0	1	1	1	2	5	8
Total		915.5	990	636.5	2542	57	52	50	159	50	54	51	155	48	52	45	145

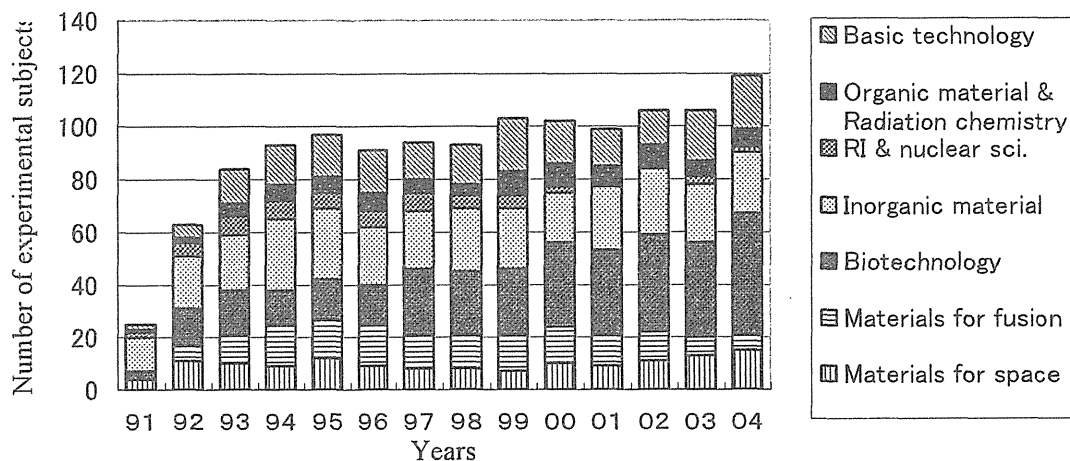


Fig. 1 The change of number of experimental subjects in various research fields.

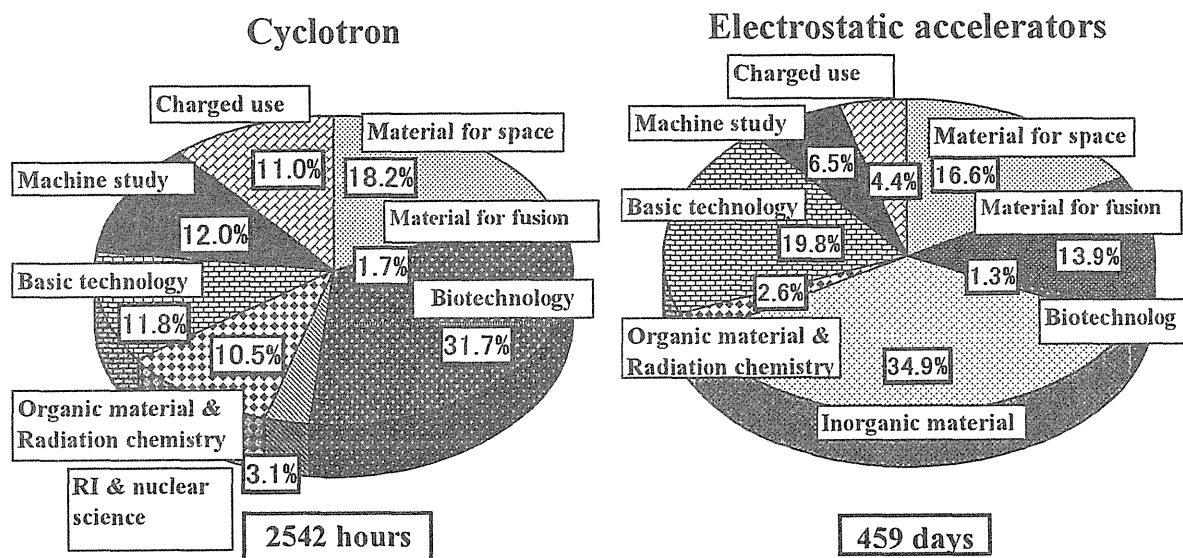


Fig. 2 Utilization of the accelerator in FY2003 in various research fields.

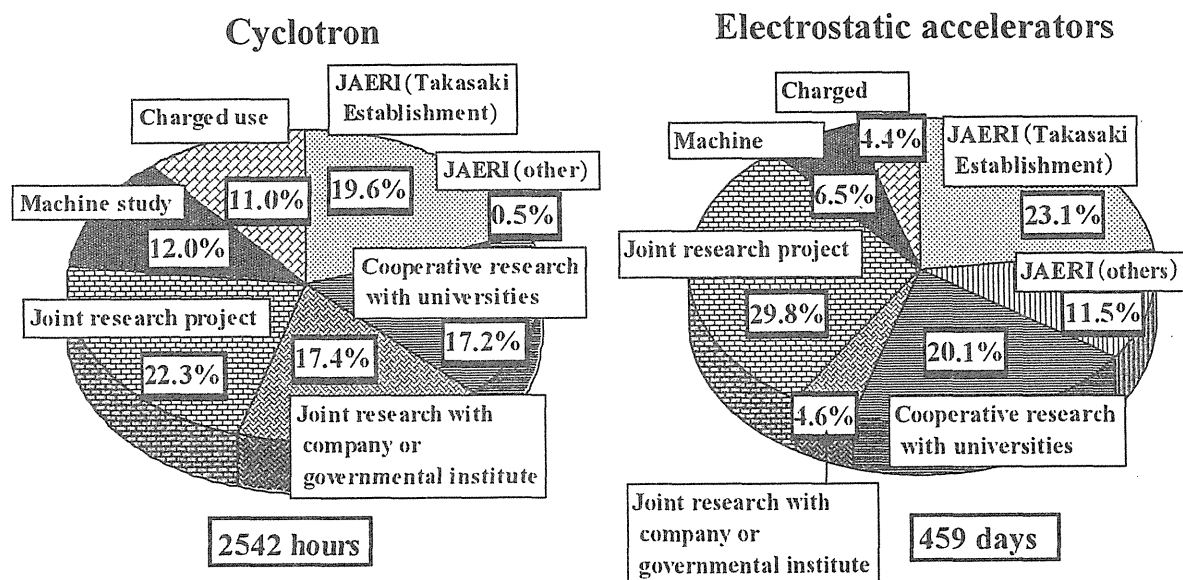


Fig. 3 Utilization of the accelerator in FY2003 in relation to the various types of users.

10.2 Operation of JAERI AVF Cyclotron System

Y. Nakamura*, T. Nara*, T. Agematsu*, I. Ishibori*, S. Kurashima*, K. Yoshida*, M. Fukuda*, S. Okumura*, N. Miyawaki*, S. Tajima*, K. Akaiwa**, To. Yoshida**, S. Ishiro**, Y. Arakawa**, Tu. Yoshida**, S. Kanou**, A. Ihara** and K. Takano**

Advanced Radiation Technology Center, JAERI*
Beam Operation Service, Co., Ltd.**

The JAERI AVF cyclotron system has been smoothly operated without any serious troubles since 1991 when the first beam was successfully extracted. Figure 1 shows the yearly operation time and cumulative one for past 14 years. What fair steps with the increase of the year are formed, it obviously means that very steady operation has been carried out. The total operation time during fiscal year 2003 amounted to 3382 hours which is the second longest time so far.

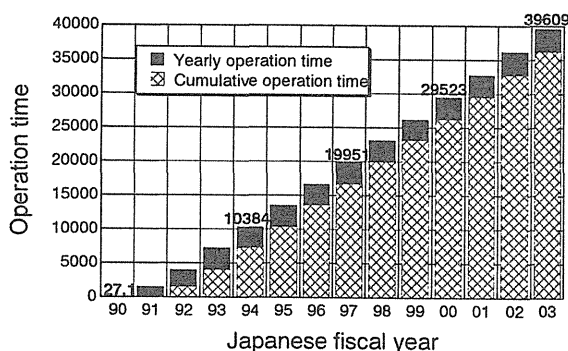


Fig. 1 Yearly and cumulative operation time since 1990.

The ratios of operation time used for experiments including charged use, machine tuning, beam development and machine study to total operation time were 65.7%, 23.8% and 10.5%, respectively.

The operation time of the cyclotron and the ECR ion source (OCTOPUS) for every month in

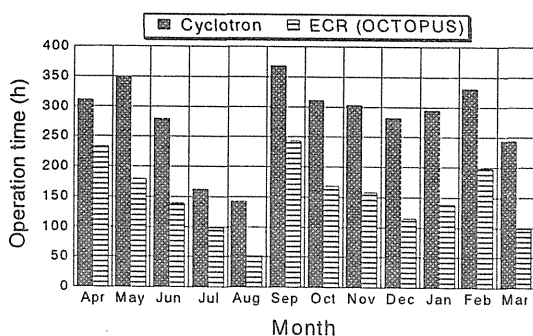


Fig. 2 Operation time of cyclotron and ECR ion source for each month in fiscal year 2003.

fiscal year 2003 is shown in Fig. 2. The cyclotron has been operated about 300 hours for normal month, on the other hand, the operation time of the OCTOPUS is 54 % of that of cyclotron on an average.

During 4 weeks between the middle of July and August in summer 2003, regular yearly overhaul including the improvement of central region devices in the cyclotron was continued. After this improvement, the beam tuning for allotted ion species was further done to maintain surely the operational schedule. On late March, the maintenance work such as the installation of cooling panel at the cyclotron bottom, the renewal of the broken TMP and vacuum chamber for beam diagnostic station, and so on was performed for two weeks.

Figure 3 shows the percentage beam time of accelerated ions. Neon beams increase slowly for recent a few years for the experiment of micro-beam. The percentage of heavy ions and cocktail ones occupied 68.0 %, while that of light ions was 32.0 %.

A great part of occurred troubles was concerned to vacuum and cooling water as well as past years. The altering frequency of operational condition also increases gradually. In especial, the frequency of beam course change reached about 370 times which was the greatest number so far.

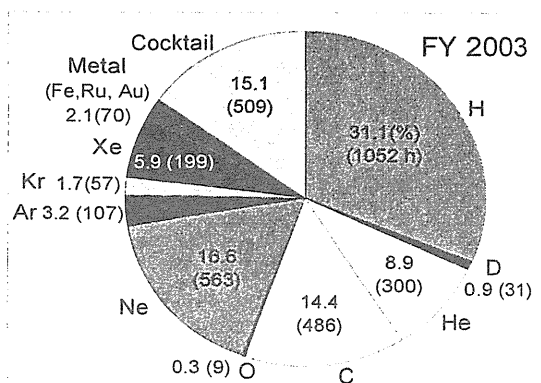


Fig. 3 Percentage beam time of accelerated ions in fiscal year 2003.

10.3 Operation of the Electrostatic Accelerators

K.Mizuhashi*, S.Uno*, K.Ohkoshi*, A.Chiba*, I. Takada*, S. Tajima*,
Y.Saitoh*, Y.Ishii*, T.Sakai*, M. Ishii**, T.Orimo**, T.Takayama**,
M.Kouka**, A.Ohmae**, T.Kitano** and S.Kanai**

Advanced Radiation Technology Center, JAERI*
Beam Operation Service, Co., Ltd.**

1. Operation

The three electrostatic accelerators were operated smoothly for various experiments in FY 2003. The total operation time for each accelerator in this fiscal year was 1,987.7 hours for the tandem accelerator, 2,286.2 hours for the single-ended accelerator and 1,773.3 hours for the 400kV ion implanter, respectively. Monthly operation time of each accelerator is shown in Fig.1. The periodic maintenance of accelerators were carried out in April, August and December. In the utilization of the basic technology, the Micro-PIXE analysis with single-ended accelerator and the experiments using cluster-beam with tandem accelerator are showing a tendency to increase recently. Figure2 shows the detailed item of the basic technology.

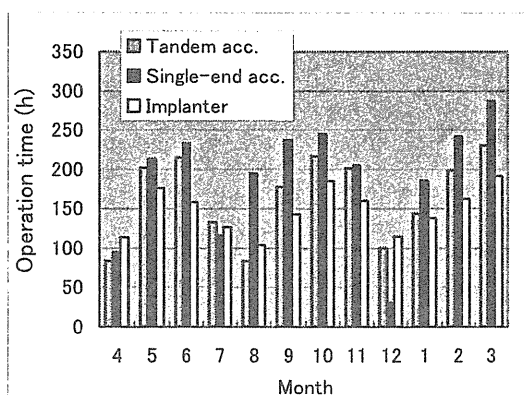


Fig.1 Monthly operation time in FY 2003

2. Maintenance of accelerators

In the tandem accelerator, the inverter fed power to the pellet chain motor system was installed in 2002 to restrain the dust of the

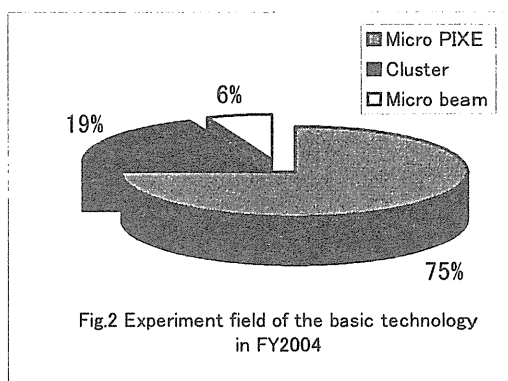


Fig.2 Experiment field of the basic technology in FY2004

carbon powder state from the electro-conductive rubber of the sheave surface. But the noise from inverter has been entrapped in many signal lines, which are related to the accelerator control. In 2003, this noise problem was solved by the measures using an electromagnetic shielding case, two sets of ferrite core and two power filters. In present state, this pellet chain driving system is completed and also the yield of the dust from pellet chain is decreased.

In the Single-ended accelerator, the computer control system was renewed in December 2003 and the control function was satisfactory by this renewal. The other side, since discharge mark greatly grows on the acrylic boards which are main structure of this accelerator, the board was exchanged to new them for the stable voltage generation.

In the ion implanter, the acceleration of fullerene (C_{60}) ions with intensity of $2\mu A$ is succeeded under the good conditions at 400keV. At present, the C_{60} ions are used research on irradiation effects for materials.

10.4 Radiation Control & Radioactive Waste Management in TIARA

Safety Division & Utilities and Maintenance Division
Department of Administrative Services, JAERI

1. Radiation Control

Maximum dose was 1.8 mSv/y due to the overhauling of the cyclotron.

1.1 Individual monitoring

(1) Individual monitoring for the radiation workers

Table 1 shows a distribution on effective dose of the radiation workers in FY 2003. The effective dose values of almost workers were less than 0.1 mSv (minimum detectable dose).

(2) Individual monitoring for the visitors and others

Table 2 shows number of persons who have been temporally entered the radiation controlled areas. The effective dose of all persons was less than 0.1 mSv.

Table 1. Distributions on the effective dose in FY 2003.

Items	Persons	Number of persons			
	Periods	1st quarter	2nd quarter	3rd quarter	4th quarter
Distribution range on effective dose HE: Effective dose ^{*1} (mSv)	HE < 0.1	529	546	557	579
	$0.1 \leq \text{HE} \leq 1.0$	3	24	3	4
	$1.0 < \text{HE} \leq 5.0$	0	1	0	0
	$5.0 < \text{HE} \leq 50.0$	0	0	0	0
	$50.0 < \text{HE}$	0	0	0	0
Persons for radiation control(A)		532	571	560	583
Exposure above 1mSv	Persons(B)	0	1	0	0
	$(B)/(A) \times 100(\%)$	0	0.2	0	0
Mass effective dose (Persons · mSv)		0.3	6.5	0.4	1.1
Mean dose (mSv)		0.00	0.01	0.00	0.00
Maximum dose (mSv)		0.1	1.5	0.2	0.3

*1 Not detected according to internal exposure.

Table 2. Number of temporary entrance persons to radiation controlled areas in FY 2003.

Temporary entrance persons	Persons	Number of persons				
	Periods	1st quarter	2nd quarter	3rd quarter	4th quarter	Total
		454	459	455	503	1871

1.2 Monitoring of radioactive gases

Table 3 shows the maximum radioactive concentrations and total activities for radioactive gases released from TIARA's stack, during each quarter of FY 2003.

The least amount of ^{41}Ar , ^{11}C , ^{77}Kr and ^{133}Xe were detected for some time during operation of the cyclotron, but the pulverized substance (^{65}Zn , etc) were not detected.

Table 3. Monitoring results of released gaseous radioactivity in FY 2003.

Nuclide	Periods	1st quarter	2nd quarter	3rd quarter	4th quarter	Total
	Items					
^{41}Ar	Maximum concentration (Bq/cm^3)	$< 1.4 \times 10^{-4}$	$< 1.4 \times 10^{-4}$	$< 1.4 \times 10^{-4}$	$< 1.4 \times 10^{-4}$	$< 1.4 \times 10^{-4}$
	Activity (Bq)	2.3×10^8	4.7×10^7	7.6×10^8	1.4×10^8	1.2×10^9
^{11}C	Maximum concentration (Bq/cm^3)	$< 1.4 \times 10^{-4}$	—	$< 1.4 \times 10^{-4}$	$< 1.4 \times 10^{-4}$	$< 1.4 \times 10^{-4}$
	Activity (Bq)	3.5×10^7	—	1.7×10^8	1.7×10^7	2.2×10^8
^{77}Kr	Maximum concentration (Bq/cm^3)	$< 1.4 \times 10^{-4}$	$< 1.4 \times 10^{-4}$	—	—	$< 1.4 \times 10^{-4}$
	Activity (Bq)	1.9×10^6	3.1×10^7	—	—	3.3×10^7
^{133}Xe	Maximum concentration (Bq/cm^3)	$< 1.4 \times 10^{-4}$	$< 1.4 \times 10^{-4}$	—	—	$< 1.4 \times 10^{-4}$
	Activity (Bq)	1.4×10^7	7.6×10^6	—	—	2.2×10^7
^{65}Zn	Maximum concentration (Bq/cm^3)	$< 4.9 \times 10^{-10}$	$< 3.8 \times 10^{-10}$	$< 4.3 \times 10^{-10}$	$< 4.4 \times 10^{-10}$	$< 4.9 \times 10^{-10}$
	Activity (Bq)	0	0	0	0	0

2. Radioactive Waste Management

2.1 Solid wastes

Table 4 shows the amounts of solid wastes at various properties and kinds generated in each quarter of FY 2003. All wastes were combustible matter such as rubber gloves, compressible matter such as thin metals, and incompressible matter such as contaminated components. Compressible wastes were generated mainly by the cyclotron maintenance.

2.2 Liquid wastes

Liquid waste was almost waste water ("inorganic" in Table 5) generated with chemical experiments and operation of air conditioning units installed in each room of the first class radiation controlled area. Larger quantities of the wastewater in summer season (2nd quarter) are mainly due to condensed water, which is treated by evaporation, and condensed water is reused in the controlled area. Only small amounts of residue are generated by the evaporation because the waste quality is very pure.

Table 4. Radioactive solid wastes generated in FY 2003.

Items	Amounts	Amounts of generation in each periods (m ³)					Number of package /drum
		1st quarter	2nd quarter	3rd quarter	4th quarter	Total	
Category A*		2.34	0.96	0.60	3.51	7.41	
1)Combustible		0.18	0.72	0.52	0.34	1.76	12**
2)Incombustible		2.16	0.24	0.08	3.17	5.65	0
Compressible		0.16	0.24	0.08	0.04	0.52	5**
Filters		0	0	0	2.73	2.73	0
Incompressible		2.00	0	0	0	2.00	10**
Ion exchange resin		0	0	0	0.40	0.40	2**
(Cement solidify)		0	0	0	0	0	0
Category B*		0	0	0	0	0	0
1)Incombustible		0	0	0	0	0	0

* defined by dose at the outer surface of container : (A) < 2 mSv/h ≤ (B)

** 200-liter drum

Table 5. Radioactive liquid waste generated in FY 2003.

Items	Amounts	Amounts of generation in each periods (m ³)					Number of package /drum
		1st quarter	2nd quarter	3rd quarter	4th quarter	Total	
Category A*		11.77	10.81	10.80	8.01	41.39	
1)Inorganic		11.77	10.81	10.80	8.01	41.39	treatment
2)Organic		0	0	0	0	0	0
Organic		0	0	0	0	0	0
Oil		0	0	0	0	0	0
3)Sludge		0	0	0	0.10	0.10	1
Category B*		0	0	0	0	0	0
1)Inorganic		0	0	0	0	0	0
2)Organic		0	0	0	0	0	0
Organic		0	0	0	0	0	0
Oil		0	0	0	0	0	0
3)Sludge		0	0	0	0	0	0
Evaporation residue		0	0	0	0.10	0.10	1

* defined by concentrations in Bq/cm³ (β, γ) : (A) < 3.7 × 10³ ≤ (B) < 3.7 × 10⁴

This is a blank page.

Appendix

Appendix 1. List of Publication	345
A1.1 Publications in Journal	345
A1.2 Publications in Proceeding	363
Appendix.2. Type of Research Collaboration	371
Appendix.3. Organization and Personnel of TIARA	373

This is a blank page.

Appendix 1. List of Publication

A. 1.1 Publications in Journal

13J01

J. S. Laird, T. Hirao, S. Onoda, H. Mori, H. Itoh

“A comparison of heavy ion and picoseconds laser microbeams for investigating single event transients in InGaAs on InP photodetectors”

Nucl. Instrum. Methods Phys. Res. B, 210 (2003) 243.

T SCS 32002

633-636.

I SCS 32004

13J05

K. K. Lee, T. Ohshima and H. Itoh

“Modeling of Radiation Response of p-Channel SiC MOSFETs”

Mater. Sci. Forum 433-436 (2003) pp. 761-764.

I SCS 32004

13J02

T. Hirao, H. Mori, J. S. Laird, S. Onoda, H. Abe, T. Wakasa and H. Itoh

“Study of single-event current pulses induces in SOI diodes by collimated swift heavy-ions micro-beams”

Nucl. Instrum. Methods Phys. Res. B, 206 (2003) 457.

C SCS 31001

13J06

K. K. Lee, Y. Ishida, T. Ohshima, K. Kojima, Y. Tanaka, T. Takahashi, H. Okumura, K. Arai and T. Kamiya

“N-Channel MOSFETs Fabricated on Homoepitaxy-Grown 3C-SiC Films”

IEEE Electron Device Lett. 24 (2003) pp.466-468.

I SCS 32004

13J03

T. Ohshima, K. K. Lee, Y. Ishida, K. Kojima, Y. Tanaka, T. Takahashi, M. Yoshikawa, H. Okumura, K. Arai, and T. Kamiya

“The Electrical Characteristics of Metal-Oxide-Semiconductor Field Effect Transistors Fabricated on Cubic Silicon Carbide”

Jpn. J. Appl. Phys. 42 (2003) pp.L625-L627.

TI SCS 32004

13J07

T. Nishijima, S. M. Hearne, D. J. Jamieson, T. Ohshima, K. K. Lee and H. Itoh

“Radiation Damage on 6H-SiC Schottky Diodes”

Nucl. Instrum. Methods Phys. Res. B, 210 (2003) pp.196-200.

I SCS 32004

13J04

T. Ohshima, A. Uedono, O. Eryu, K. K. Lee, K. Abe, H. Itoh and K. Nakashima

“Annealing of a Vacancy-Type Defect and Diffusion of Implanted Boron in 6H-SiC”

Mater. Sci. Forum 433-436 (2003) pp.

13J08

T. Ohshima, K. K. Lee, S. Onoda, T. Kamiya, M. Oikawa, J. S. Laird, T. Hirao and H. Itoh

“Evaluation of the Characteristics of Silicon Carbide Diodes using Transient-IBIC Technique”

Nucl. Instrum. Methods Phys. Res. B, 210 (2003) pp.201-205.

TI SCS 32004

13J09

Y. Nakanishi, A. Wakahara, H. Okada, A. Yoshida, T. Ohshima, H. Itoh, S. Nakao, K. Saito and Y. T. Kim

“Effects of Implantation Conditions on the Luminescence Properties of Eu-Doped GaN”
Nucl. Instrum. Methods Phys. Res. B, 206 (2003) p.1033.

I IOM 32006

13J10

Y. Nakanishi, A. Wakahara, H. Okada, A. Yoshida, T. Ohshima, H. Itoh, T. Shibata and M. Tanaka

“Effects of Al Composition on Luminescence Properties of Europium Implanted $\text{Al}_x\text{Ga}_{1-x}\text{N}$ ($0 \leq x \leq 1$)”
Physica Status Solidi (c) 0, (2003) p.2623.

I IOM 32006

13J11

Y. Nakanishi, A. Wakahara, A. Yoshida, T. Ohshima and H. Itoh

“Improvement of Luminescence Capability of Tb^{3+} -Related Emission by $\text{Al}_x\text{Ga}_{1-x}\text{N}$ ”
Physica Status Solidi (b), 240, No.2, (2003) pp.372-375.

I IOM 32006

13J12

H. -S. Lee, T. Ohshima, H. Itoh, S. Kawakita, M. Imaizumi, S. Matsuda, H. Okada, A. Wakahara and A. Yoshida

“Effects of High-Energy Proton Irradiation on the Density and Hall Mobility of Majority-Carriers in Single Crystalline n-Type CuInSe_2 Thin Films”

Physica Status Solidi (a), 199, (2003) p.471.

I SCS 32006

13J13

H. -S. Lee, H. Okada, A. Wakahara, A. Yoshida, T. Ohshima and H. Itoh

“Photoelectromagnetic Effects on Electron and Proton Irradiated CuInSe_2 Thin Films”
J Appl. Phys. 94 (2003) p.276.

I SCS 32006

13J14

T. Tanaka, T. Yamaguchi, T. Ohshima, H. Itoh, A. Wakahara and A. Yoshida

“Effect of Cl Ion Implantation on Electrical Properties of CuInSe_2 Thin Films”
Solar Energy Materials and Solar Cells, 75 (2003) pp.109-113.

I SCS 32006

13J15

H. -S. Lee, H. Okada, A. Wakahara and A. Yoshida

“Effect of Proton Irradiation on Electrical Properties of CuInSe_2 Thin Films”
Solar Energy Materials and Solar Cells, 75 (2003) pp.57-63.

I SCS 32006

13J16

S. Kitamura, M. Inoue, N. Ohmido, K. Fukui and A. Tanaka

“Chromosomal rearrangements in interspecific hybrids between *Nicotiana glauca* Domin and *N. tabacum* L., obtained by crossing with pollen exposed to helium ion beams or gamma-rays”

Nucl. Instrum. Methods Phys. Res. B, 206, (2003) pp.548-552.

C BIT 31008

13J17

Y. Yokota, Y. Hase, N. Shikazono, A. Tanaka and M. Inoue

“LET dependence of lethality of carbon ion

irradiation to single tobacco cells”

Int. J. Radiat. Biol. 79,(2003) pp.681-685.

C BIT 31008

13J18

Y. Yokota, T. Funayama, Y. Kobayashi, T. Sakashita, S. Wada, Y. Hase, N. Shikazono, A. Tanaka and M. Inoue

“Development of an ion microbeam system for irradiating single plant cell[s]”

Biol. Sci. Space 17,(2003)pp. 298-301.

C BIT 31008, 31026

13J19

A. Sakamoto, V. T. T. Lan, N. Shikazono, Y. Hase, T. Matsunaga and A. Tanaka

“Disruption of the *AtREV3* gene causes hypersensitivity to ultraviolet B light and γ -rays in Arabidopsis: Implication of the presence of a translation synthesis mechanism in plants”

Plant Cell 15, (2003)pp.2042-2057.

C BIT 31011

13J20

M. Okamura, N. Yasuno, M. Takano, A. Tanaka, N. Shikazono and Y. Hase

“Wide variety of flower-color and -shape mutants regenerated from leaf cultures irradiated with ion beams”

Nucl. Instrum. Methods Phys. Res. B, 206 (2003)574-578.

C BIT 31014

13J21

M. Okamura

“Commercialization of New Variety Series in 3 Major Flowers bred by Ion Beam Breeding”

Radiation & Industries, 99, (2003)46-53.

C BIT 31014

13J22

S. Nagayoshi

“Irradiation Breeding in KAGOSHIMA; Breeding of ‘few axillary bud lines’ using ion beam in Chrysanthemum”

Radiation & Industries 98 (2003): 10-16.

C BIT 31015

13J23

K. Ishii, Y. Yamada, Y. Hase, N. Shikazono and A. Tanaka

“RAPD Analysis of Mutants Obtained by Ion Beam Irradiation to Hinoki Cypress Shoot Primordia”

Nucl. Instrum. Methods Phys. Res. B, 206 (2003) 570-573.

C BIT 31016

13J24

T. Sato

“Breeding of Chrysanthemum”

Annual of Akita prefecture Agricultural experiment station (2003) in press.

C BIT 31020

12J25

Y. Kobayashi, T. Funayama, S. Wada, M. Taguchi and H. Watanabe

“System of Cell Irradiation with a Precise Number of Heavy ions”

Radiat. Res., 161, (2004)90-91.

C BIT 31026

13J26

T. Funayama, S. Wada and Y. Kobayashi

“Effect of a Single Argon-Ion Hit on Cultured Mammalian Cells”

Radiat. Res., 161, (2004)111-112.

C BIT 31026

13J27

Y. Kobayashi, T. Funayama, S. Wada, M.

Taguchi and H. Watanabe

“Irradiation of single mammalian cells with a precise number of energetic heavy ions - Applications of microbeams for studying cellular radiation response -”

Nucl. Instrum. Methods Phys. Res. B, 210 (2003) 308-311.

C BIT 31026

13J28

K. Kiguchi, K. Shirai, R. Kanekatsu, Y. Kobayashi, Z. -L. Tu, T. Funayama and H. Watanabe

“Radiosurgery using heavy ion microbeams for biological study: Fate mapping of the cellular blastoderm-stage egg of the silkworm *Bombyx mori*”

Nucl. Instrum. Methods. B, 210 (2003) 312-315.

C BIT 31026

13J29

Y. Furusawa, C. Shao, Y. Kobayashi, T. Funayama and S. Wada

“Bystander effect induced by counted high-LET particles in confluent human fibroblasts: a mechanistic study”

FASEB J, 17, (2003) 1422-1427.

C BIT 31026

13J30

S. Wada, T. V. Khoa, Y. Kobayashi, T. Funayama, K. Yamamoto, M. Natsuhori and N. Ito

“Detection of Radiation-Induced Apoptosis Using the Comet Assay”

J. Vet. Med. Sci., 65 (11), (2003) 1161-1166.

C BIT 31026, 31029

13J31

S. Wada, M. Natsuhori, N. Ito, T. Funayama and Y. Kobayashi

“Detection of DNA damage induced by heavy ion irradiation in the individual cells with comet assay”

Nucl. Instrum. Methods Phys. Res. B, 206 (2003) 553-556.

C BIT 31026

13J32

Z. -L. Tu, Y. Kobayashi, K. Kiguchi and H. Watanabe

“Irradiation effect of different heavy ions and track section on the silkworm *Bombyx mori*”

Nucl. Instrum. Methods Phys. Res. B, 206 (2003) 591-595.

C BIT 31026

13J33

S. Wada, H. Kurahashi, Y. Kobayashi, T. Funayama, K. Yamamoto, M. Natsuhori and N. Ito

“The Relationship between Cellular Radiosensitivity and Radiation-Induced DNA Damage Measured by the Comet Assay”

J. Vet. Med. Sic. 65 (4), (2003) 471-477.

C BIT 31026

13J34

K. Kiguchi, K. Shirai, R. Kanekatsu, Y. Kobayashi, Z. -L. Tu, T. Funayama and H. Watanabe

“Radiosurgery using heavy ion microbeams for biological study: Fate mapping of the cellular blastoderm-stage egg of the silkworm, *Bombyx mori*”

Nucl. Instrum. Methods Phys. Res. B, 210 (2003) 312-315.

C BIT 31027

13J35

Y. Kobayashi and K. Kiguchi

“Radiomicrosurgery using heavy ion microbeams—Application for analysis of

regeneration mechanism of hemopoietic organ after irradiation of heavy ion microbeam in the silkworm *Bombyx mori*—”

Isotope News, (9), (2003)9-12.

C BIT 31027

13J36

C. Shao, Y. Furusawa and M. Aoki

“Sper/NO-induced reversible proliferation inhibition and cycle arrests associated with a micronucleus induction in HSG cells”

Nitric Oxide: Biol. Chem., 8(2): (2003)83-88.

O BIT 31028

13J37

C. Shao, Y. Furusawa, Y. Kobayashi, T. Funayama and S. Wada

“Bystander effect induced by counted high-LET particles in confluent human fibroblasts: a mechanistic study”

FASEB J. 17, (2003)1422-1427.

C BIT 31028

13J38

C. Shao, Y. Furusawa, M. Aoki and K. Ando

“Role of gap junctional intercellular communication in radiation-induced bystander effect on human fibroblast cell”

Radiat. Res. 160(3), (2003)64-69.

C BIT 31028

13J39

C. Shao, M. Aoki and Y. Furusawa

“Bystander effect on cell growth stimulation in neoplastic HSGc cells induced by heavy-ion irradiation”

Radat, Environ, Biophys., 42, (2003)183-187.

O BIT 31028

13J40

C. Shao, M. Aoki and Y. Furusawa

“Bystander effect in lymphoma cells vicinal to

irradiated neoplastic epithelial cells: Nitric oxide is involved”

J. Radiat. Res., 45, (2004)97-103.

C BIT 31028

13J41

Y. Bai, Y. Soda, K. Izawa, T. Tanabe, X. Kang, A. Tojo, H. Hoshino, H. Miyoshi, S. Asano and K. Tani

“Effective transduction and stable transgene expression in human blood cells by a third-generation lentiviral vector”

Gene Ther., 10, (2003)1446-1457.

C BIT 31030

13J42

S. Kusagawa, Y. Imamura, A. Yasuoka, H. Hoshino, S. Oka and Y. Takebe

“Identification of HIN type 2 subtype B transmission in East Africa”

AIDS Res. Hum. Retrovir., 19, (2003)1045-1049.

C BIT 31030

13J43

A. Shimizu, N. Shimizu, A. Tanaka, A. Jinno-Oue, B. B. Roy, M. Shinagawa, O. Ishikawa and H. Hoshino

“Human T-cell leukaemia virus type I is highly sensitive to UV-C light”

J. Gen. Virol. (in press).

C BIT 31030

13J44

H. Hayashi, S. Wada, T. Funayama, I. Narumi, Y. Kobayashi, H. Watanabe, M. Furuta and K. Uehara

“Evaluation of the resistance of *Euglena gracilis* to ion beam radiation”

J. Eukaryot. Microbiol. 51(3), (2004) pp. 321-324.

C BIT 31032

13J45

M. Watanabe, T. Kikawada and T. Okuda

“Increase of internal ion concentration triggers trehalose synthesis associated with cryptobiosis in larvae of *Polypedilum vanderplanki*”

J. Exp. Biol. 206, (2003) 2281-2286.

C BIT 31034

13J46

E. A. Reda, H. Saneoka and K. Fujita

“Effect of salinity on osmotic adjustment, glycinebetaine accumulation and the betaine aldehyde dehydrogenase gene expression in two halophytic plants, *Salicornia europaea* and *Suaeda maritima*”

Plant Sci., 166, (2004) 1345-1349.

O BIT 31038

13J47

Pravat K. Mohapatra, Y. Masamoto, S. Morita, J. Takanashi, T. Kato, T. Itani, Joseph J. Adu-Gyamfi, M. Shunmugasondaram, N. T. Nguyen, H. Saneoka and K. Fujita

“Partitioning of ^{13}C -labelled Photosynthate varies with Growth Stages and Panicle Size in High Yielding Rice”

Functional plant biology, 31, (2004) 1-9.

O BIT 31038

13J48

K. Fujita, M. Okada, Kei Li, J. Ito, K. Ohkura, Joseph J. Adu-Gyamfi and Pravat Kumar Mohapatra

“Effect of P-deficiency on photoassimilate partitioning and rhythmic changes in fruit and stem diameter of tomato (*Lycopersicon esculentum*) during fruit growth”

J. Exp. Bot. 54, (2003)2519-2528.

O BIT 31038

13J49

K. Fujita, J. Ito, P. K. Mohapatra, H. Saneoka,

K. Lee, H. Kurban, K. Kawai and K. Ohkura
“Circadian rhythm of stem and fruit diameter dynamics of Japanese persimmon (*Diospyros Kaki* Thunb.) is affected by deficiency of water in saline environments”

Functional Plant Biology 30, (2003)747-754.

O BIT 31038

13J50

H. A. El-Shemy, A. M. Aboul-Enein, M. I. Aboul-Enein, S. I. Issa and K. Fujita

“The Effect of Willow Leaf Extracts on Human Leukemic Cells In Vitro”

J. Biochem. and Mol. Biology, 36, (2003)387-389.

O BIT 31038

13J51

N. T. Nguyen, P. K. Mohapatra and K. Fujita

“Leaf necrosis is a visual symptom of the shift from growth stimulation to inhibition effect of Al in *Eucalyptus camaldulensis*”

Plant Sci., 165, (2003)147-157.

O BIT 31038

13J52

Nguyen Tran Nguyen, K. Nakabayashi, J. Thompson and K. Fujita

“Role of organic acids and phosphate exudation on aluminum-tolerance in four tropical woody plants”

Tree Physiology 23, (2003)1041-1050.

O BIT 31038

13J53

H. Nobuyasu, Shunki Liu, Joseph J. Adu-Gyamfi, Pravat Kumar Mohapatra and K. Fujita

“Variation in the export of ^{13}C and ^{15}N from soybean leaf: the effects of nitrogen

application and sink removal”

Plant and Soil, 253, (2003) 331-339.

O BIT 31038

13J54

Y. Maekawa, H. Koshikawa and M. Yoshida
“Anisotropically conducting films consisting
of sub-micron copper wires in the ion track
membranes of poly(ethylene terephthalate)”

Polymer 45 (2004) 2291 – 2295.

C RCO 31046

13J55

S. Takahashi, M. Yoshida, M. Asano, M.
Notomi and T. Nakagawa

“Characterizations of heavy ion irradiated PET
membranes”

Nucl. Instrum. Methods Phys. Res. B, 217
(2004)435-441.

C RCO 31047

13J56

S. Takahashi, M. Yoshida, M. Asano and T.
Nakagawa

“Gas-permeation control by PET membranes
with nanosized pores”

Polym. J., 36, (2004)50-53.

C RCO 31047

13J57

S. Tsukuda, S. Seki, S. Tagawa, M. Sugimoto,
A. Idesaki, S. Tanaka and A. Ohshima

“Fabrication of Nano-Wires Using
High-Energy Ion Beams”

J. Phys. Chem. B, 108 (2004) 3407-3409.

C RCO 31050

13J58

S. Seki, Y. Koizumi, T. Kawaguchi, H.
Habara and S. Tagawa

“Dynamics of Positive Charge Carriers on Si
Chains of Polysilanes”

J. Am. Chem. Soc. 126 (2004) 3521-3528.

C RCO 31050

13J59

S. Tsukuda, S. Seki, A. Saeki, T. Kozawa, S.
Tagawa, M. Sugimoto, A. Idesaki and S.
Tanaka

“Precise Control of Nanowire Formation
Based on Polysilane for Photoelectronic
Device Application”

Jpn. J. Appl. Phys. 43 (2004) 3810-3814.

C RCO 31050

13J60

S. Chanprateep, K. Kikuya, H. Shimizu, S.
Seki, S. Tagawa and S. Shioya

“Nonisothermal crystallization kinetics of
biodegradable random
poly(3-hydroxybutyrate-co-3-hydroxyvalerate)
and block one”

J. Chem. Eng. Jpn., 36 (2003) 639-646.

C RCO 31050

13J61

Y. Matsui, S. Umeda, S. Seki, S. Tagawa, S.
Ishikawa and T. Itani

“Dependence of Outgassing Characters at a
157nm Exposure on Resist Structures”

Jpn. J. Appl. Phys., 42 (2003) 3894-3899.

C RCO 31050

13J62

S. Seki, Y. Matsui, S. Tagawa, H. Tsuji, A.
Toshimitsu and K. Tamao

“Transient absorption spectroscopy of radical
ions of rigid anti- and syn-tetrasilane”

Chem. Phys. Lett., 380 (2003) 141-145.

C RCO 31050

13J63

S. Tsukuda, S. Seki, S. Tagawa, M. Sugimoto,
A. Idesaki and S. Tanaka

“Cross-linked Polymer Nanowires with Controlled Shape and Orientation by High Energy Single Ion Hitting”

J. Photopolym. Sci. Technol., 16 (2003) 433-434.

C RCO 31050

13J64

T. Kawaguchi, S. Seki, K. Okamoto, A. Saeki, Y. Yoshida and S. Tagawa

“Pulse Radiolysis Study of Radical Cations of Polysilanes”

Chem. Phys. Lett., 374 (2003) 353-357.

C RCO 31050

13J65

Y. Terashima, S. Seki, M. Tashiro, Y. Honda and S. Tagawa

“Study of Nano-Space in Au-Polysilane Interfaces by Slow Positron Beam”

J. Photopolym. Sci. Technol., 16 (2003) 445-446.

C RCO 31050

13J66

S. Seki, S. Tsukuda, Y. Yoshida, T. Kozawa, S. Tagawa, M. Sugimoto and S. Tanaka

“Nano-wire Formation and Selective Adhesion on Substrates by Single Ion Track Reaction in Polysilanes”

Jpn. J. Appl. Phys., 43 (2003) 4159-4161.

C RCO 31050

13J67

M. Tashiro, C. Y. Tseng, S. Seki, Y. Honda and S. Tagawa

“Influence of Radiation-induced Species on Positronium Formation in Poly(methylmethacrylate) at Low Temperature”

Radiat. Phys. Chem., 68 (2003) 475-479.

C RCO 31050

13J68

S. Seki, Y. Terashima, K. Kunimi, T. Kawamori, M. Tashiro, Y. Honda and S. Tagawa

“The Effects of Free Volumes on Charge Carrier Transport in Polysilanes Probed by Positron Anihilation”

Radiat. Phys. Chem., 68 (2003) 501-505.

C RCO 31050

13J69

K. Hirata, Y. Saitoh, A. Chiba, K. Narumi, Y. Kobayashi and K. Arakawa

“Time-of-flight secondary ion mass spectroscopy for surface analysis of insulators using a cluster ion beam”

Appl. Phys. Lett., 83, (2003)4872.

T RCO 32015

13J70

K. Hirata, Y. Saitoh, K. Narumi, and Y. Kobayashi

“Effect of external bias potential on secondary charged emissions from an organic insulator by C_1^+ and C_8^+ bombardments”

Nucl. Instrum. Methods Phys. Res. B, 206 (2003) 47.

T RCO 32015

13J71

A. Hasegawa, S. Miwa, S. Nogami, A. Taniguchi, T. Taguchi and K. Abe

“Study of Hydrogen effects on microstructural development of SiC base materials under simultaneous irradiation with He- and Si-ion irradiation condition”

J. Nucl. Mater., in press.

T I S IOM 32008

13J72

T. Taguchi, N. Igawa, S. Miwa, E. Wakai, L. L. Snead, A. Hasegawa and S. Jitsukawa

“Synergistic effect of implanted He and H and effect of irradiation temperature on microstructure of SiC/SiC composites”

J. Nucl. Mater., in press.

T I S IOM 32008

13J73

M. Ando, E. Wakai, T. Sawai, H. Tanigawa, K. Furuya, S. Jitsukawa, H. Takeuchi, K. Oka, S. Ohnuki and A. Kohyama

“Synergistic Effect of Displacement Damage and Helium Atoms on Radiation hardening in F82H at TIARA Facility”

J. Nucl. Mater. in press.

T S IOM 32009

13J74

Y. Tsuchiya, F. Kano, N. Saito, A. Shioiri, K. Moriya and S. Kasahara

“SCC properties of metals under supercritical-water cooled power reactor conditions”

Corrosion2004(2004),Paper04485.

T IOM 32013

13J75

D. Yamaki, T. Nakazawa, T. Tanifuji, T. Aruga, S. Jitsukawa and K. Hojou

“Observation of the microstructural changes in lithium titanate by multi-ion irradiation”

J.Nucl.Mater. In press.

T I S IOM 32037

13J76

H. Abe, N. Sekimura and Y. Yang

“Stability and mobility of defect clusters in copper under displacement cascade conditions”

J. Nucl. Mater. **323** (2003) 220–228.

I IOM 32016

13J77

H. Abe

“Atomistic observations and analyses of lattice defects in transmission electron microscopes” (Japanese)

Journal the Visualization Society of Japan 23(2003)145.

I IOM 32016

13J78

V. Lavrentiev, H. Abe, S. Yamamoto, H. Naramoto and K. Narumi

“Isolation of Co nanoparticles by C60 molecules in co-deposited film”

Mat. Lett., 57 (2003)4093-4097.

I IOM 32016

13J79

M. Matsubara, T. Yamaki, H. Itoh, H. Abe and K. Asai

“Preparation of TiO₂ nanoparticles by pulsed laser ablation: ambient pressure dependence of crystallization”

Jpn. J. Appl. Phys. **42** (2003) L479-L481.

I IOM 32016

13J80

Y. Kasukabe, Z. L. Dizard, Y. Fujino, H. Tani, M. Osaka, Y. Yamada and H. Abe

“In-situ observation of formation process of titanium compound thin films due to ion implantation in a transmission electron microscope”

Nucl. Instrum. Methods Phys. Res. B, 206 (2003) 390-394.

I IOM 32016

13J81

T. Hirabayashi

“C₆₀ nanowhiskers –their synthesis, microstructure and stability under electron irradiation”

B.E. Thesis, School of Engineering, The University of Tokyo (2003).

I IOM 32016

13J82

Y. Kasukabe, Z. L. Dizard, Y. Fujino, H. Tani, M. Osaka, Y. Yamada and H. Abe

“In-situ Observation of Formation Processes of Titanium Compound Thin Films due to Ion Implantation in A Transmission Electron Microscope”

Nucl. Instrum. Methods Phys. Res. Section B, 206 (2003) 390-394.

I IOM 32017

13J83

H. Kudo, K. Takeda, T. Suguri, W. Iwazaki, C. Sakurai, I. Arano, S. Numazawa and S. Seki

“Electron loss from fast partially-stripped C and O ions incident on crystal targets”

Nucl. Instrum. Methods Phys. Res. B, 207 (2003) 283-290.

O MAN 32023

13J84

H. Abe, H. Uchida, Y. Azuma, A. Uedono, Z. Q. Chen and H. Itoh

“Improvement of hydrogen absorption rate of Pd by ion irradiation”

Nucl. Instrum. Methods Phys. Res. B, 206 (2003), p.224.

I IOM 32031

13J85

Z. Q. Chen, S. Yamamoto, M. Maekawa, A. Kawasuso and T. Sekiguchi

“Postgrowth Annealing of Defects in ZnO Studied by Positron Annihilation, X-ray Diffraction Rutherford backscattering, Cathodoluminescence and Hall Measurement”

J Appl. Phys., 94, (2003)4807.

O MAN 32032

13J86

Z. Q. Chen, T. Sekiguchi, M. Maekawa and A. Kawasuso

“N⁺ ion-implantation induced defects in ZnO studied with a slow positron beam”

J. Phys. Condens. Matter, 16, (2004) S293.

I MAN 32032

13J87

Z. Q. Chen, M. Maekawa, S. Yamamoto, A. Kawasuso, X. L. Yuan, T. Sekiguchi, R.

Suzuki and T. Ohdaira

“Evolution of voids in Al⁺-implanted ZnO probed by a slow positron beam”

Phys. Rev., B 69, (2004)035210.

I MAN 32032

13J88

Z. Q. Chen, M. Maekawa, T. Sekiguchi, R. Suzuki and A. Kawasuso

“Ion-implantation Induced Defects in ZnO Studied by a Slow Positron Beam”

Mater. Sci. Forum, 57 (2004)445-446.

I MAN 32032

13J89

A. Kawasuso, Y. Fukaya, K. Hayashi, M. Maekawa, S. Okada and A. Ichimiya

“Si(111)-(7x7) surface probed by reflection high-energy positron diffraction”

Phys. Rev. B68 (2003) 241313.

O IOM off line

13J90

A. Kawasuso, T. Ishimoto, Y. Fukaya, K. Hayashi and A. Ichimiya

“Top Most Surface Studies by Total Reflection Positron Diffraction”

e-J. Surf. Sci. Nanotech. 1, (2003) 152.

O IOM off line

13J91

K. Hayashi, Y. Fukaya, A. Kawasuso and A. Ichimiya

“Kinematical and dynamical analysis of reflection high-energy positron diffraction (RHEPD) patterns from Si(111)7x7 surfaces”
Appl. Surf. Sci., in press.

O IOM off line

13J92

Y. Fukaya, A. Kawasuso, K. Hayashi and A. Ichimiya

“Precise determination of surface Debye-temperature of Si(111)-7x7 surface by reflection high-energy positron diffraction”
Appl. Surf. Sci., in press.

O IOM off line

13J93

T. Umebayashi, T. Yamaki, H. Itoh and K. Asai

“Band-Gap Narrowing of Titanium Dioxide by Sulfur Doping”
Appl. Phys. Lett. 81 (2002) 454-456.

I IOM 32020

13J94

T. Umebayashi, T. Yamaki, S. Yamamoto, A. Miyashita, S. Tanaka, T. Sumita and K. Asai

“Sulfur-doping of rutile-titanium dioxide by ion implantation: Photocurrent spectroscopy and first-principles band calculation studies”
J. Appl. Phys. 93 (2003) 5156-5160.

I IOM 32020

13J95

T. Umebayashi, T. Yamaki, S. Tanaka and K. Asai

“Sulfur Doped Titanium Dioxide as a Novel Visible-Light Photocatalyst”
Chem. Lett. 32 (2003) 330-331.

I IOM 32020

13J96

Y. Choi, T. Umebayashi and M. Yoshikawa

“Fabrication and characterization of C-doped anatase TiO₂ photocatalysts”

J. Mater. Sci. Lett. (2003) in press.

I IOM 32020

13J97

Y. Choi, T. Umebayashi, S. Yamamoto and S. Tanaka

“Fabrication of TiO₂ photocatalysts by oxidative annealing of TiC”

J. Mater. Sci. Lett. 22 (2003) 1209-1211.

I IOM 32020

13J98

A. Kawasuso, Y. Fukaya, K. Hayashi, M. Maekawa, T. Ishimoto, S. Okada and A. Ichimiya

“Observation of Fast Positron Diffraction from a Si(111)7x7 Surface”

Mater. Sci. Forum 445-446 (2004) 385.

O IOM off line

13J99

J. Vacik, V. Hnatowicz, J. Cervena, H. Naramoto, S. Yamamoto and D. Fink

“Energy Loss and Energy Straggling of Light Ions in Fullerite”

Fullerene Science and Technology 9 (2001) 197-209.

O IOM off line

13J100

K. Narumi and H. Naramoto

“AFM Investigation of Growth Process of C60 Thin Films on a KBr (001) Surface”

Diamond and Related Materials 10 (2001) 980-983.

I S IOM 32029

13J101

J. Vacik, H. Naramoto, K. Narumi, S. Yamamoto and K. Miyashita
 "Pattern Formation Induced by Co-deposition of Ni and C60 on MgO(100)"
 J. Chem. Phys., 114 (2001) 9115-9119.
 O IOM off line

13J102

X. D. Zhu, Y. H. Xu, H. Naramoto, K. Narumi and K. Miyashita
 "Role of simultaneous Ne⁺ ion bombardments in preparing carbon films from C60 fullerene"
 J. Phys.: Condensed Matter 14 (2002) 5083-5090.
 O IOM off line

13J103

X. D. Zhu, H. Naramoto, Y. H. Xu, K. Narumi and K. Miyashita
 "Tuning Surface Morphologies of Ion-Assisted Diamond-like Carbon Film on Nanometer Scale"
 J. Chem. Phys., 116 (2002) 10458-10461.
 O IOM off line

13J104

V. I. Lavrentiev, H. Abe, S. Yamamoto, H. Naramoto and K. Narumi
 "Formation of Carbon Nanotubes under Conditions of Co+C60 Films"
 Physica B: Condens Matter 323 (2002) 303-305.
 O IOM off line

13J105

V. I. Lavrentiev, H. Abe, S. Yamamoto, H. Naramoto and K. Narumi
 "Co and C60 Interaction under Conditions of Mixture"
 Mol. Cryst. Liq. Cryst. 386 (2002) 139-143.
 I/S IOM 32029

13J106

K. Narumi and H. Naramoto
 "Modification of C60 Thin Films by Ion Irradiation"
 Surf. Coat Technol., 158-159C (2002) 364-367.
 I S IOM 32029

13J107

X. D. Zhu, H. Naramoto, Y. H. Xu, K. Narumi and K. Miyashita
 "Coarsening Dynamics and Surface Stability of during Ion-beam-assisted Growth of Amorphous Diamond-like Carbon"
 Phys. Rev. B 66 (2002) 165426.
 O IOM off line

13J108

H. Naramoto, X. D. Zhu, J. Vacik, Y. H. Xu, K. Narumi, S. Yamamoto and K. Miyashita
 "Allotropic Conversion of Carbon-related Films by Using Energy Beams"
 Phys. of the Solid State 44 (2002) 668-673.
 T S IOM 32029

13J109

A. Ya. Vul, V. G. Golubev, S. A. Grudinkin, A. Krüger and H. Naramoto
 "Diamond Films: Initial CVD Growth Stage Using Nanodiamonds as Nucleation Centers"
 Tech. Phys. Letters 28 (2002) 787-789.
 O IOM off line

13J110

V. I. Lavrentiev, H. Abe, S. Yamamoto, H. Naramoto and K. Narumi
 "Formation of Promising Co-C Nano-compositions"
 Surf. Interface Anal., 35 (2003) 36-39.
 I S IOM 32029

13J111

K. Narumi, Y. Xu, K. Miyashita and H. Naramoto

“Effect of Ion Irradiation on C60 Thin Films”
Euro. Phys. J. D 24 (2003) 385-388.

I S IOM 32029

13J112

X. D. Zhu, Y. H. Xu, H. Naramoto, K. Narumi, A. Miyashita and K. Miyashita

“Ion Beam Assisted Hexagonal Diamond Formed from C60 Fullerene”

J. Phys. : Condens. Matter. 15 (2003) 2899-2906.

O IOM off line

13J113

J. Vacik, H. Naramoto, S. Yamamoto and K. Narumi

“RBS and SEM Analysis of the Nickel-fullerene Hybrid Systems”

Nucl. Instrum. Methods Phys. Res. B, 206 (2003) 395-398.

O IOM off line

13J114

R. Ookawa, K. Takahiro, K. Kawatsura, F. Nishiyama, S. Yamamoto and H. Naramoto

“Structure of Amorphized C60 films Studied by Raman and X-ray Photoelectron Spectroscopy”

Nucl. Instrum. Methods Phys. Res. B, 206 (2003) 175-178.

O IOM off line

12J115

J. Vacik, H. Naramoto, K. Narumi, S. Yamamoto and H. Abe

“RBS and SEM Analysis of The Nickel-Fullerene Hybrid Systems”

Nucl. Instrum. Methods Phys. Res. B, 206 (2003) 395-398.

O IOM off line

13J116

V. Lavrentiev, H. Abe, S. Yamamoto, H. Naramoto and K. Narumi

“Isolation of Co Nanoparticles by C60 Molecules in Co-deposited Film”

Mater. Lett., 57 (2003) 4093-4097.

O IOM off line

13J117

V. Lavrentiev, H. Naramoto, H. Abe, S. Yamamoto, K. Narumi and S. Sakai

“Chemically-driven Microstructure Evolution in Cobalt-fullerene Mixed System”

Fullerene, Nanotubes and Carbon Nanostructures 12 (2004) 519-528.

O IOM off line

13J118

X. D. Zhu, X. H. Wen, R. J. Zhan, H. Naramoto and F. Arefi-Khonsart

“Control of Characteristic Lengths for Self-Organized Nanostructures of Amorphous Carbon”

J. Phys.: Condensed Matter 16 (2004) 1175-1181.

O IOM off line

13J119

J. Vacik, H. Naramoto, K. Narumi, S. Yamamoto and H. Abe

“Study of the Nickel-Fullerene Nano-structured Thin Films”

Nucl. Instrum. Methods Phys. Res. B, 219-220 (2004) 862-866.

O IOM off line

13J120

X. D. Zhu, K. Narumi, Y. Xu, H. Naramoto and F. Arefi-Khonsari

“Self-organized Textured Surfaces of Amorphous Carbon”

J. Appl. Phys. 95 (2004) 4105-4110.

O IOM off line

13J121

J. Vacik, H. Naramoto, S. Yamamoto and K. Narumi

“Epitaxial Re-crystallization of the Ni/MgO(001) Interfaces”

Nucl. Instrum. Methods Phys. Res. B, 219-220 (2004) 867-870.

S IOM MAN 32022

13J122

C. Lin, H. Naramoto, Y. H. Xu, S. Kitazawa, K. Narumi and S. Sakai

“Formation of Nano-sized Pinholes Array in Thin Ni Film on MgO(100) Substrate”

Thin Solid Films 443 (2003) 28-32.

O IOM 32022

13J123

C. Lin, Y. H. Xu, H. Naramoto, P. Wei, S. Kitazawa and K. Narumi

“Morphology Evolution of Thin Ni Film on MgO(100) Substrate”

J. Phys. D 35 (2002) 1864-1866.

O IOM 32022

13J124

K. Yamakawa, Y. Chimi, N. Ishikawa and A. Iwase

“Hydrogen migration in electron irradiated Pd based dilute alloys around the 50 K anomaly”

J. Alloys and Compounds 370 (2004) 211-216.

S IOM 32027

13J125

S. Ishino, Y. Chimi, Bagiyono, T. Tobita, N. Ishikawa, M. Suzuki and A. Iwase

“Radiation Enhanced Copper Clustering

Processes in Fe-Cu Alloys during Electron and Ion Irradiations as Measured by Electrical Resistivity”

J. Nucl. Mater. 323 (2003) 354-359.

S IOM 32028

13J126

S. Sakai, H. Tanimoto, E. Kita and H. Mizubayashi

“Characterization and Determination of Elastic Property of High-Density Nanocrystalline Gold Prepared by Gas-Deposition Method”

Mater. Trans., 44, (2003), 94-103.

S IOM 32029

13J127

H. Tanimoto, S. Sakai¹, K. Otuka, E. Kita, and H. Mizubayashi

“Underlying Mechanisms for Unique Elastic Properties of Nanocrystalline Au”

Mater. Sci. Eng. A, 370(2004), 177-180.

S IOM 32029

13J128

J. Isoya, T. Ohshima, N. Morishita, T. Kamiya, H. Itoh and S. Yamasaki

“Pulsed EPR studies of shallow donor impurities in SiC”

Physica B 340-342 (2003) 903.

T IOM 32030

13J129

T. Souno, H. Nishikawa, M. Hattori, Y. Ohki, E. Watanabe, M. Oikawa, T. Kamiya and K. Arakawa

“Characterization of ion-implanted silica glass by micro-photoluminescence and Raman spectroscopy”

Nucl. Instrum. Methods Phys. Res. B, 210 (2003) 277-280.

T S IOM 32034

13J130

M. Hattori, Y. Ohki, M. Fujimaki, T. Souno, H. Nishikawa, E. Watanabe, M. Oikawa, T. Kamiya and K. Arakawa

“Characterization of refractive index changes of silica glass induced by ion microbeam”

Nucl. Instrum. Methods Phys. Res. B, 210 (2003) 272-276.

T S IOM 32034

13J131

H. Nishikawa, K. Fukagawa, T. Yanagi, Y. Ohki, E. Watanabe, M. Oikawa, T. Kamiya and K. Arakawa

“Effects of Ion Microbeam Irradiation on Silica Glass”

Trans. Mater. Res. Soc. Jpn., 29 (2004) 603-606.

T S IOM 32034

13J132

C. -J. Ma, M. Kasahara, S. Tohno and T. Sakai
“A replication technique for the collection of individual fog droplets and their chemical analysis using micro-PIXE”

Atmos. Environ. 37, (2003)4679-4686.

S RCO 32038

13J133

C. -J. Ma, Y. Inoguchi, M. Kasahara, S. Tohno and T. Sakai

“Micro-PIXE analysis of reference standards for the quantitative analysis of trace elements in individual raindrops”

Nucl. Instrum. Methods Phys. Res. B, 215 (2003)501-508.

S RCO 32038

13J134

T. Ohnuki, F. Sakamoto, N. Kozai, T. Ozaki, I. Narumi, A. J. Francis, H. Iefuji, T. Sakai, T. Kamiya, T. Satoh and M. Oikawa

“Application of micro-PIXE technique to uptake study of Cesium by *Saccharomyces cerevisiae*”

Nucl. Instrum. Methods Phys. Res. B, 210 (2003)378-382.

S C IOM 32039

13J135

N. Kozai, T. Ohnuki, S. Komaeneni, T. Kamiya, T. Sakai, M. Oikawa and T. Satoh

“Uptake of cadmium by synthetic mica and apatite: Observation by micro-PIXE”

Nucl. Instrum. Methods Phys. Res. B, 210, (2003)513-518.

S C IOM 32039

13J136

T. Ohnuki, F. Sakamoto, N. Kozai, T. Sakai, T. Kamiya, T. Satoh and M. Oikawa

“Micro-PIXE study on sorption behaviors of cobalt by lichen biomass”

Nucl. Instrum. Methods Phys. Res. B, 210 (2003)407-411.

S C IOM 32039

13J137

T. Ohnuki, N. Kozai, T. Ozaki, T. Yoshida, A. J. Francis, H. Iefuji and T. Sakai

“Accumulation of Co by *Saccharomyces cerevisiae*”

Geochim. Cosmochim. Acta, Suppl., 67, (2003)18S A352..

S C IOM 32039

13J138

T. Kamiya, T. Hirao and Y. Kobayashi

“Development of single-ion hit techniques and their applications at TIARA of JAERI Takasaki”

Nucl. Instrum. Methods Phys. Res. B, 219-220 (2004) pp.1010-1014.

T ACT 32040

13J139

T. Satoh, K. Ishii, T. Kamiya, T. Sakai, M. Oikawa, K. Arakawa, S. Matsuyama and H. Yamazaki

“Development of a large-solid-angle and multi-device detection system for elemental analysis”

Nucl. Instrum. Methods Phys. Res. B, 210 (2003) pp.113-116.

T ACT 32040

13J140

T. Ohshima, K. K. Lee, S. Onoda, T. Kamiya, M. Oikawa, J. S. Laird, T. Hirao and H. Itoh

“Evaluation of the characteristics of silicon carbide diodes using transient-IBIC technique”

Nucl. Instrum. Methods Phys. Res. B, 210 (2003) pp.201-205.

IT SCS ACT 32004, 32040

13J141

T. Kamiya, M. Oikawa, T. Ohshima, T. Hirao, K. K. Lee, S. Onoda and J. S. Laird

“Observation of single-ion induced charge collection in diode by a heavy ion microbeam system”

Nucl. Instrum. Methods Phys. Res. B, 210 (2003) pp.206-210.

IT SCS ACT 32004, 32040

13J142

H. Yamamoto, M. Nomachi, K. Yasuda, Y. Iwami, S. Ebisu, N. Yamamoto, T. Sakai and T. Kamiya

“Fluorine Mapping of Teeth Treated with Fluorine-releasing Compound Using PIGE”

Nucl. Instrum. Methods Phys. Res. B, 210(2003) p388.

S ACT 32042

13J143

S. Harada, K. Ishii, A. Tanaka, T. Satoh, S.

Matsuyama, H. Yamazaki, T. Kamiya, T. Sakai, K. Arakawa, M. Saitoh, S. Oikawa and K. Sera

“METHOD FOR DETERMINING THE LOCALIZATION OF TRACE ELEMENTS OBSERVED BY THE MICRO PIXE CAMERA”

Int. J. PIXE IN PRESS.

S BIT 32046

13J144

S. Matsuyama, K. Ishii, H. Yamazaki, R. Sakamoto, M. Fujisawa, Ts. Amartaivan, Y. Oishi, M. Rodriguez, A. Suzuki, T. Kamiya, M. Oikawa, K. Arakawa and N. Matsumoto

“Preliminary Results ob microbeam at TohokuUniversity”

Nucl. Instrum. Methods Phys. Res. B, 210(2003) 59-64

S ACT 32048

13J145

Y. Oishi, K. Hotta, K. Ishii, Y. Komori, S. Matsuyama, H. Yamazaki, T. Amartivan, M. Rodriguez, K. Katoh, D. Izukawa, K. Mizuma, T. Satoh, T. Kamiya, T. Sakai, K. Arakawa, M. Saidoh and M. Oikawa

“3D imaging of elemental distributions using multi-angle RBS 2D-data”

Nucl. Instrum. Methods Phys. Res. B, 210 (2003) 117-122.

S ACT 32048

13J146

T. Satoh, K. Ishii, T. Kamiya, T. Sakai, M. Oikawa, K. Arakawa, S. Matsuyama and H. Yamazaki

“Development of a large-solid-angle and multi-device detection system for elemental analysis”

Nucl. Instrum. Methods Phys. Res. B, 210 (2003) 113-116.

S ACT 32048

13J147

K. Ishii, H. Yamazaki, S. Matsuyama and Y. Kikuchi

“Establishment of Central Research Laboratory for Accurate Quantitative PIXE Analysis -An Approach of Tohoku University-”

Int. J. PIXE, 13 (1&2), (2003) 17-22.

S ACT 32048

13J148

S. Matsuyama, K. Katoh, S. Sugihara, K. Ishii, H. Yamazaki, T. Satoh, Ts. Amartaivan, A. Tanaka, H. Komori, K. Hotta, D. Izukawa, K. Mizuma, H. Orihara, E. Nakamura, N. Satoh, S. Futatsugawa and K. Sera

“Multi-site Aerosol Monitoring Using Mini Step Sampler”

Int. J. PIXE, 13 (1&2), (2003) 65-80.

S ACT 32048

13J149

H. Yamazaki, K. Ishii, S. Matsuyama, Y. Komori, K. Mizuma and T. Izukawa

“Summary of the Workshop on Practical Problems in Biological Application of Micro-PIXE Analysis”

Int. J. PIXE, 13 (1&2), (2003) 89-96.

S ACT 32048

13J150

S. Iwatani, J. Kaneko, J. Hasegawa, H. Fukuda, R. He, Y. Saitoh, T. Sakai, M. Ogawa and Y. Oguri

“Imaging by Using Proton-Induced Quasi-Monochromatic X-ray Emission”

Sci. Tech. Adv. Mater., in press.

S MAN 32049

13J151

K. Sato, S. Yokoyama, H. Noguchi, Su. Tanaka, T. Iida, S. Furuichi, Y. Kanda and Y. Oki

“Attachment of ^{38}Cl and ^{39}Cl induced by high-energy neutrons to coexisted aerosols”

J. Nucl. Sci. Technol., Suppl. 4, (2004) p. 518-521.

C RSH 31053

13J152

K. Oda, Y. Imasaka, K. Tsukahara, T. Yamauchi, Y. Nakane and Y. Yamaguchi

“Radiator effect on plastic nuclear track detectors for high-energy neutrons”

Radiation Measurements, 36 (2003) 119-124.

C RSH 31055

13J153

A. Endo, E. Kim, Y. Yamaguchi, T. Sato, M. Yoshizawa, Su. Tanaka, T. Nakamura and D. R. D. Rasolonjatovo

“Development of Neutron-monitor Detectors Applicable to Energies from Thermal to 100MeV”

J. Nucl. Sci. Technol., Suppl.4, (2004)510-513.

C RSH 31055

13J154

K. Oda, Y. Imasaka, T. Yamauchi, Y. Nakane, A. Endo and Y. Yamaguchi

“Deuterized radiator for detection of high-energy neutrons with plastic nuclear track detector”

J. Nucl. Sci. Technol., Suppl.4, (2004)514-517.

C RSH 31055

13J155

T. Sato, A. Endo, Y. Yamaguchi and F. Takahashi

“Development of Neutron-monitor Detector
Using Liquid Organic Scintillator Coupled
with $^6\text{Li}+\text{ZnS}(\text{Ag})$ Sheet”

Radiat. Prot. Dosim., in press.

C RSH 31055

13J156

S. Kitazawa, S.Yamamoto, M Asano and S.
Ishiyama

“Radiation-induced luminescence and
photoluminescence from sol-gel silica glasses
and phosphosilicate glasses”

Physica B 349(2004)159-165.

T I IOM 32036

A.1.2 Publications in Proceeding

13C01

S. Kawakita, M. Imaizumi, T. Sumita, K. Kushiya, T. Ohshima, M. Yamaguchi, S. Matsuda, S. Yoda and T. Kamiya

“Super Radiation Tolerance of CIGS Solar Cells Demonstrated in Space by MDS-1 Satellite”

Proc. of 3rd World Conference on Photovoltaic Energy Conversion, May 2003 (Osaka) 3PB511.

I SCS 31003,32003

13C02

S. Kawakita, M. Imaizumi, S. Kuwajima, S. Yoda, T. Ohshima, T. Kamiya and M. Yamaguchi

“Analysis of Radiation Response of Cu(In,Ga)Se₂ Thin-Film Solar Cells by Spectral Response”

Proc. of 14th International Photovoltaic Science and Engineering Conference, January 2004 (Bangkok) P-131.

I SCS 31003,32003

13C03

M. Imaizumi, T. Takamoto, T. Sumita, T. Ohshima, M. Yamaguchi, S. Matsuda, A. Ohi and T. Kamiya

“STUDY OF RADIATION RESPONSE ON SINGLE-JUNCTION COMPONENT SUB-CELLS IN TRIPLE-JUNCTION SOLAR CELLS”

Proc. of 3rd World Conference on Photovoltaic Energy Conversion, May 2003 (Osaka) 3O-D6-02.

I SCS 31003,32003

13C04

S. Matsuda, M. Imaizumi, O. Anzawa, S. Kawakita, T. Sumita, K. Aoyama and N. Tanioka

“RADIATION EFFECTS IN SPACE ON SOLAR CELLS DEVELOPED FOR TERRESTRIAL USE DEMONSTRATED BY MDS-1”

Proc. of 3rd World Conference on Photovoltaic Energy Conversion, May 2003 (Osaka) 3O-D12-03.

I SCS 31003,32003

13C05

T. Takamoto, T. Agui, K. Kamimura, M. Kaneiwa, M. Imaizumi, S. Matsuda and M. Yamaguchi

“MULTIJUNCTION SOLAR CELL TECHNOLOGIES - HIGH EFFICIENCY, RADIATION

RESISTANCE, AND CONCENTRATOR APPLICATIONS”

Proc. of 3rd World Conference on Photovoltaic Energy Conversion, May 2003 (Osaka) 3PL-C2-01.

I SCS 31003,32003

13C06

T. Sumita, M. Imaizumi, S. Matsuda, T. Ohshima, A. Ohi and T. Kamiya

“Analysis of End-of-Life Performance for Proton Irradiated Triple-Junction Space Solar Cell”

Proc. of 3rd World Conference on Photovoltaic Energy Conversion, May 2003 (Osaka) 3PB510.

I SCS 31003,32003

13C07

T. Sumita, M. Imaizumi, S. Kawakita, S. Matsuda, S. Kuwajima, T. Ohshima and T. Kamiya

“Analysis of Radiation Effects in Space for Terrestrial Solar Cells on MDS-1”

Proc. of 40th IEEE Nuclear and Space Radiation Effects Conference (NSREC) , 2003.7 Monterey CA.

I SCS 31003,32003

13C08

T. Sumita, M. Imaizumi, S. Kuwajima, T. Ohshima, A. Ohi and T. Kamiya

"Analysis of radiation response of triple-junction space solar cells and component sub-cells"

Proc. of 14th International Photovoltaic Science and Engineering Conference, January 2004 (Bangkok) P-113.

I SCS 31003,32003

13C09

H. Shindou, S. Kuboyama, N. Ikeda, S. Matsuda and T. Hirao

"Bulk Damage Caused by Single Protons in SDRAMs"

The IEEE Nuclear and Space Radiation Effects Conference(NSREC 2003).

C SCS 31002

13C10

S. Kuboyama, H. Shindo S. Matsuda and T. Hirao

"Consistency of Bulk Damage Factor and NIEL for Electrons, Protons, and Heavy Ions in Si CCDs"

The IEEE Nuclear and Space Radiation Effects Conference(NSREC 2002).

C SCS 31002

13C11

A. Makihara, S. Kuboyama, S. Matsuda, N. Nemoto, H. Ohtomo, K. Furuse, S. Baba and T. Hirose

"Non-Damaging Beam Blanking SEM Test Method and its Application to Highly Integrated Devices"

The IEEE Nuclear and Space Radiation Effects Conference(NSREC 2001).

C SCS 31002

13C12

A. Makihara, H. Shindou, N. Nemoto, S. Kuboyama, S. Matsuda T. Ohshima, T. Hirao, H. Itoh S. Buchner and A. B. Campbell

"Analysis of Single-Ion Multiple-Bit Upset in High-Density DRAMs"

The IEEE Nuclear and Space Radiation Effects Conference(NSREC 2000).

C SCS 31002

13C13

T. Ohshima, N. Morishita, T. Kamiya, J. Isoya, S. Baba, J. Aihara, M. Yamaji and M. Ishihara

"Introduction of Phosphorus Atoms in Silicon Carbide using Nuclear Transmutation Doping at Elevated Temperature"

Proceedings of the 3rd Information Exchange Meeting on Basic Studies in the Field of High Temperature Engineering, 11-12 Sept. 2003, Oarai (Japan) pp.197-202.

I SCS 32004

13C14

H.S. Lee, H. Okada, A. Wakahara, T. Ohshima, H. Itoh and A. Yoshida

"Effects of High-Energy Proton Irradiation on the Diffusion Length in CuInSe₂ Thin Films"

The 14th Int. Photovoltaic Science and Engineering Conference (Jan. 26-30,2004, Bangkok, Thailand) P-139.

I SCS 32006

13C15

Y. Hase, S. Fujioka, S. Yoshida, G. Sun, M. Umeda and A. Tanaka

"Endoreduplication caused by sterol alteration results in serrated petals in Arabidopsis"

Plant & Cell Physiology 45 Supplement (2004),

p213.

C BIT 31011

13C16

Sakinah Ariffin and Mohd Nazir B.

“Mutagenesis of *Oncidium lanceanum* “

Proceedings of MINT R&D Seminar 2004. In press.

I BIT 31012

13C17

Degi K., S. Nagatomi, T. Morishita, H. Yamaguchi, K. Miyagi, A. Tanaka, N. Shikazono and Y. Hase

“The variation of nuclear DNA contents and the induction of somatic mutation with gamma rays and helium ion irradiation to in vitro shoots of sugarcane”

Breed. Research.5(suppl.1) :(2003)280.

C BIT 31013

13C18

K. Ueno, S. Nagayoshi, Y. Hase, N. Shikazono and A. Tanaka

“Additional Improvement of Chrysanthemum using Ion Beam Re-irradiation.”

Ion beam breeding (2004) 1:

C BIT 31015

13C19

S. Isogai, K. Touno, K. Shimomura, Y. Hase and A. Tanaka,

“Research on mutants induced by exposure to heavy ion beam in *Cephaelis ipecacuanha*”

March 2004 (Hiroshima) , Japan Society for Bioscience, Biotechnology, and Agrochemistry, p. 298.

C BIT 31024

13C20

Y. Kobayashi, T. Funayama, S. Wada, M. Taguchi and H. Watanabe

“Irradiation of single mammalian cells with a precise number of energetic heavy ions”

12th International Congress of Radiation Research (ICRR2003), Brisbane, Australia, Aug 17-22, 2003. p. 341.

C BIT 31026

13C21

T. Funayama, Y. Kobayashi and S. Wada

“Effect of Targeted Heavy Ion Irradiation on Cell Nucleus”

12th International Congress of Radiation Research (ICRR2003), Brisbane, Australia, Aug 17-22, 2003. p. 340.

C BIT 31026

13C22

S. Wada, T. Funayama and Y. Kobayashi

“The Effect of Track Structure on the Induction of DNA Damage and Cell Killing”

12th International Congress of Radiation Research (ICRR2003), Brisbane, Australia, Aug 17-22, 2003. p. 305.

C BIT 31026

13C23

Y. Furusawa, K. Ando, M. Aoki, C. Shao, Y. Kobayashi, T. Funayama and S. Wada

“Bystander effects through gap junction channels by heavy-ion microbeam”

12th International Congress of Radiation Research (ICRR2003), Brisbane, Australia, Aug 17-22, 2003. p. 286.

C BIT 31026

13C24

C. Shao, K. M. Prise, V. Stewart, M. Folkard and B.D. Michael

“Involvement of Nitric Oxide in the Bystander Response Induced by Microbeam Targeted Cells”

Microbeam Probes of Cellular Response,

March 2003 (Oxford) Vol.6, 127-129.

C BIT 21029

13C25

N. Shimizu, A. Tanaka, A. Oue, K. Kanbe and H. Hoshino

“G protein-coupled receptors having DY-sequence in the amino-terminal region act as coreceptors for human and simian immunodeficiency viruses: Identification of the functional domain of the coreceptor activity of GPR1”

The 6th international Symposium on VIP, PACAP and Related Peptides 2003(Hakone).

C BIT 31030

13C26

K. Akeo, R. Inoue, A. Ogawa, T. Funayama and Y. Kobayashi

“Effects of gamma irradiation on genes related to apoptosis in the ciliary body”

14th Annual Meeting of Ocular Oxidative Stress Research Society 10. 10. 2003. Okayama.

O BIT 31031

13C27

K. Akeo, R. Inoue, T. Funayama, Y. Kobayashi and A. Ogawa

“Comparison of the effects on the ciliary body between gamma ray irradiation and ion beam”

108th Annual Meeting of Japanese Ophthalmological Society. 4. 16 2004. Tokyo.

O BIT 31031

13C28

H. Hayashi, T. Funayama, I. Narumi, M. Kikuchi, Y. Kobayashi, M. Furuta, K. Uehara and H. Watanabe

“The effect of various radiations with different LET on survival of *Euglena gracilis*”

RadTech Asia '03 Yokohama, Japan, 2003 pp. 693—696.

C BIT 31032

13C29

T. Okuda, M. Watanabe, T. Kikawada, A. Fujita and E. Forczek

“Cryptobiosis in the African chironomid: physiological mechanism to survive complete dehydration”

Proc. Arthropod. Embryol. Soc. Jpn. 39: 1-7 (2004).

C BIT 31034

13C30

M. Saitou, T. Sugihara, K. Tanaka and T. Matsumoto

“Effects of Heavy Ion Microbeam on Gene Expression of Mouse Cultured Cells Effects of Low Dose-Rate Radiation on Genes”

The 2003 Fiscal Year Report of Institute for Environmental Sciences, 2004. (In press) [In Japanese].

C BIT 31035

13C31

K. Sakamoto, S. Fujimaki, N. S. Ishioka, S. Watanabe, K. Arakawa and S. Matsuhashi

“Real-Time Imaging of the Translocation of the Products of Photosynthesis in Hemp”

The 41st Annual Meeting on Radioisotopes and Radiation in the Physical Sciences and Industries, July 2004 (Tokyo).

C BIT 31036

13C32

H. Sekimoto, R. Matsuki, Y. Kobayashi D. Sato, K. Yoneyama, Y. Takeuchi, S. Matsuhashi, S. Fujimaki, K. Sakamoto, N. S. Ishioka, S. Watanabe, K. Arakawa and T. Kume

“Visualization of sink activity of a root

parasite, broomrape, for translocating nitrate in the host plant”

38th Annual Meeting of The Japanese Society for Chemical Regulation of Plants 2003 (Nagoya) Proceedings p.92-93.

C BIT 31042

13C33

Y. Yoshida, J. Yang, S. Seki, S. Tagawa, H. Shibata, M. Taguchi, T. Kojima and H. Nanba
“Ion Beam Pulse Radiolysis for Optical Absorption Spectroscopy”

Proc. 46th. Japan Radiation Chemistry, 2003(Japan) p102.

C RCO 31049

13C34

T. Sawai, M. Ando, E. Wakai and S. Jitsukawa
“Microstructural Evolution and Hardening in F82H up to 100dpa”

Proc. of 11th International Conference on Fusion Reactor Materials, December, 2003, (Kyoto)p.43.

T S IOM 32009

13C35

T. Sawai, M. Ando, E. Wakai, H. Tanigawa and S. Jitsukawa

“Hardening of F82H steel Multi-Beam Irradiated in TIARA”

Proc. of 6th Meeting of Fusion and Energy, JPSF, Sendai, (2004), p162.

T S IOM 32009

13C36

I. Ioka, K. Kiuchi, K. Yamamoto and H. Kitamura

“Development of new cladding materials applied for advanced LWR”

7th Russian Conference on Material Science, Sep 8-12, Dimitrovgrad, (2003).

T I S MAN 32010

13C37

I. Ioka, M. Futakawa, A. Naito, Y. Nanjyo, K. Kiuchi and T. Naoe

“Mechanical Characterization of Austenitic Stainless Steel ion-irradiated under External Stress”

11th International Conference on Fusion Reactor Materials, Dec 7-12, Kyoto, (2003).

T I S MAN 32010

13C38

Y. Tsuchiya, F. Kano, N. Saito, A. Shioiri, K. Moriya and S. Kasahara

“SCC and irradiation properties of metals under supercritical-water cooled power reactor conditions”

Proceedings of GENES4/ANP2003 (2003) Paper1096.

T IOM 32013

13C39

T. Hirabayashi, H. Abe, T. Fukui and N. Sekimura

“Microstructure of fullerene nanowhiskers and their stability under irradiation with electrons and ions”

The 59th annual meeting of Japanese society of microscopy (2003).

I IOM 32016

13C40

H. Abe, T. Tadokoro and N. Sekimura

“Experimental evidence of crowdion bundles by in-situ TEM under ion irradiations”

The 59th annual meeting of Japanese society of microscopy (2003).

I IOM 32016

13C41

O. Shepelyev, N. Sekimura and H. Abe

“Migration of interstitial complexes in irradiated Fe-Cr-Ni alloys”

The 132nd JIM spring meeting (2003).

I IOM 32016

13C42

Y. Yang, H. Abe and N. Sekimura

“Behavior of Dislocation Loops under Stress Environment”

The 132nd JIM spring meeting (2003).

I IOM 32016

13C43

T. Tadokoro, H. Abe and N. Sekimura

“Stability of displacement cascades in gold by in-situ TEM observations”

The 132nd JIM spring meeting (2003).

I IOM 32016

13C44

H. Abe, T. Hirabayashi and N. Sekimura

“Irradiation induced amorphization of fullerene nanowhiskers under irradiations with electrons and ions”

The 132nd JIM spring meeting (2003).

I IOM 32016

13C45

Y. Yang, H. Abe and N. Sekimura

“Behavior of Dislocation Loops under Stress Environment”

The 132nd JIM spring meeting (2003).

I IOM 32016

13C46

S. Yamamoto, Y. Choi, T. Umebayashi and M. Yoshikawa

“Preparation of Highly Oriented TiO_2/ZnO Films by Pulsed Laser Deposition”

The 8th IUMRS International Conference on Advanced Materials October 8-13, 2003 (Yokohama).

S IOM 32018

13C47

Z. Q. Chen, M. Maekawa, T. Sekiguchi, R. Suzuki and A. Kawasuso

“Ion-implantation Induced Defects in ZnO Studied by a Slow Positron Beam”

13th International conference on positron annihilation, Sept. 7-12, 2003.

I MAN 32032

13C48

Z. Q. Chen, M. Maekawa, A. Kawasuso, A. Ichimiya, R. Suzuki and T. Ohdaira,

“Nitrogen-related defects in N-implanted ZnO studied by positron annihilation”

Kyoto University Nuclear Reactor Institute Workshop, Dec. 19-20, 2003, Kyoto.

I MAN 32032

13C49

Z. Q. Chen, M. Maekawa, T. Ishimoto, A. Kawasuso and A. Ichimiya

“Vacancy defects in electron irradiated ZnO studied by positron annihilation”

The 40th Annual Meeting on Radioisotopes and Radiation in the Physical Sciences and Industries, July 2003.

O MAN 32032

13C50

Z. Q. Chen, M. Maekawa, S. Yamamoto, T. Sekiguchi and A. Kawasuso

“Study of ion beam induced defects in ZnO by using slow positron beam”

JAERI-Review, 2003-033, (2003) 209.

I MAN 32032

13C51

J. Vacik, H. Naramoto, S. Yamamoto, K. Narimi and K. Miyashita

“Mesoscopic Patterning Induced by Co-deposition of C_{60} and Ni on the $\text{MgO}(100)$ Single Crystal”

Mat. Res. Soc. Symp. Proc. 648 (2001)
P3.50.1-P3.50.6.
O IOM off line

13C52

S. Sakai, Y. XU, Tri Hardi Priyanto, V. I. Lavrentiev and H. Naramoto
“The Structure Evolution and Corresponding Electrical Properties in Softly Bound Co-C₆₀ Mixture”
Proc. of Materials Research Society (2003, Boston).
O IOM off line

13C53

J. Vacik, H. Naramoto, K. Narumi, S. Yamamoto and H. Abe
“Synthesis and Characterization of the Nickel-Fullerene Nano-structured Materials”
4th Int. Conf. on Materials Structures and Micromechanics of Fracture (MSMF-4, Brno, Czech, June 23-25, 2004).
O IOM off line

13C54

H. Nishikawa, K. Fukagawa, T. Yanagi, Y. Ohki, E. Watanabe, M. Oikawa, T. Kamiya and K. Arakawa
“Effects of Ion Microbeam Irradiation on Silica Glass”
The 8th IUMRS International Conference on Advanced Materials, Symposium A-9, Innovative Nanomaterials Using Ion Technology, A9-09-O09, pp.96, Oct. 8-13, 2003.
T S IOM 32034

13C55

J. Hori, M. Nakao, K. Ochiai, M. Yamauchi, N. S. Ishioka and T. Nishitani
“Measurement of Deuteron-Induced Activation Cross-Sections for Aluminum, Copper and

Tungsten in 22-34 MeV Region”
JAERI-Conf 2004-005.
C NRI 31045

13C56

M. Kasahara, C. -J. Ma, M. Okumura, S. Tohno and T. Sakai
“Micro-PIXE technique for the study of atmospheric science.”
Proc. of 10th International Conference on Particle-induced X-ray Emission and its Analytical Applications, June 2004 (Slovenia) p. 24.
S RCO 32038

13C57

S. Harada, S. Ehara K. Ishii, S. Matsuyama, H. Yamazaki, K. Mizuma, K. Hotta, T. Izukawa, S. Anbe S. Obara, T. Kamiya, T. Sakai, T. Satoh and S. Oikawa
” A new target preparation procedure of the micro PIXE Camera for the floating cells”
10 th International Conference of Particle Induced X-ray Emission 2004. June 2004 (Slovenia) IN PRESS.
S BIT 32046

13C58

S. Harada, S. Ehara K. Ishii, S. Matsuyama, H. Yamazaki, K. Mizuma, K. Hotta, T. Izukawa, S. Anbe S. Obara, T. Kamiya, T. Sakai, T. Satoh and S. Oikawa
” The alteration of the Carboplatin (Platinum analogues for cancer therapy) by the low dose irradiation studied in human leukemia, A preliminary study”
10 th International Conference of Particle Induced X-ray Emission 2004. June 2004 (Slovenia) IN PRESS.
S BIT 32046

13C59

S. Yokoyama, K. Sato, H. Noguchi, Su. Tanaka and Y. Kurosawa

"Characterization of radionuclides formed in the air of the AVF cyclotron room"

Proceeding of the Second Annual Convention of Japan Society of Radiation Safety Management, December 2003 (Tsukuba) p.109.

C RSH 31053

13C60

T. Sato, A. Endo, Y. Yamaguchi, E. Kim and T. Nakamura

"Development of Neutron-monitor Detectors Applicable for Energies up to 100MeV"

Proc. of the Third Workshop on Dosimetry for External Radiations, March 2003 (Tokai) p.78.

C RSH 31055

13C61

Y. Nakamura, T. Nara, T. Agematsu, I. Ishibori, S. Kurashima, M. Fukuda, S. Okumura, N. Miyawaki, K. Yoshida, K. Arakawa, S. Tajima, K. Akaiwa, To. Yoshida, S. Ishiro, A. Matsumura, Y. Arakawa, Tu. Yoshida, S. Kanou, A. Ihara and K. Takano

"Present Status of JAERI AVF Cyclotron System"

Proc. of 14th Symposium on Accelerator Science and Technology, November 2003 (Tsukuba, Japan) pp 678-680

C STA Machine Study

13C62

Y. Nakamura, M. Fukuda, I. Takada, T. Kamiya, K. Arakawa, M. Saidoh and Y. Ohara

"An Outline of JAERI TIARA Facility"

Proc. of 14th Symposium on Accelerator Science and Technology, November 2003 (Tsukuba, Japan) pp 702-704

C (T, S & I) STA Machine Study

Appendix 2. Type of Research Collaboration

Section of this Report	Research Program Number	Type of Research Collaborations*	Section of this Report	Research Program Number	Type of Research Collaborations*
1.1	31003/32003	Joint.Res.			
1.2	31006/32005	Joint.Res.	3.1	31046	Coop.Res.Univ.
1.3	31002	Joint.Res.	3.2	31047	JAERI
1.4	31005/32007	Joint.Res.	3.3	31048	JAERI
1.5	32002	JAERI	3.4	31056	JAERI
1.6	31001	JAERI	3.5	31049	Coop.Res.Univ.
1.7	32001	JAERI	3.6	31050	Coop.Res.Univ.
1.8	31004	Coop.Res.Univ.	3.7	32015	Joint Res. Proj.
1.9	32004	JAERI			
1.10	32006	Coop.Res.Univ.	4.1	31007	Joint Res. Proj.
			4.2	32008	Joint Res. Proj.
2.1	31008	Coop.Res.Univ.	4.3	32009	Joint Res. Proj.
2.2	31009	Joint.Res.	4.4	32010	JAERI
2.3	31010	Joint.Res.	4.5	32011	JAERI
2.4	31011	JAERI	4.6	32012	JAERI
2.5	31012	Joint.Res.	4.7	32013	Joint.Res.
2.6	31013	Joint.Res.	4.8	32037	JAERI
2.7	31014	Joint.Res.	4.9	32016	Coop.Res.Univ.
2.8	31015	Joint.Res.	4.10	32017	Coop.Res.Univ.
2.9	31016	Joint.Res.	4.11	32018	JAERI
2.10	31017	Coop.Res.Univ.	4.12	32023	Joint Res. Proj.
2.11	31018	Coop.Res.Univ.	4.13	32021	Coop.Res.Univ.
2.12	31019	Coop.Res.Univ.	4.14	32031	Coop.Res.Univ.
2.13	31020	Joint.Res.	4.15	32032	JAERI
2.14	31021	Joint.Res.	4.16	off line	JAERI
2.15	31022	Coop.Res.Univ.	4.17	32035	JAERI
2.16	31023	Joint.Res.			
2.17	31024	Coop.Res.Univ.	5.1	32019	Coop.Res.Univ.
2.18	31025	Coop.Res.Univ.	5.2	32020	JAERI
2.19	31026/32014	JAERI	5.3	32024	Joint Res. Proj.
2.20	31027	Coop.Res.Univ.	5.4	32022	JAERI
2.21	31028	Joint.Res.	5.5	32025	Joint Res. Proj.
2.22	31029	Coop.Res.Univ.	5.6	32026	JAERI
2.23	31030	Coop.Res.Univ.	5.7	32027	JAERI
2.24	31031	Joint.Res.	5.8	32028	Coop.Res.Univ.
2.25	31032	Coop.Res.Univ.	5.9	32029	Coop.Res.Univ.
2.26	31033	Coop.Res.Univ.	5.10	32030	Coop.Res.Univ.
2.27	31034	Joint.Res.	5.11	32033	Coop.Res.Univ.
2.28	31035	Joint.Res.	5.12	32034	Coop.Res.Univ.
2.29	31036	Joint Res. Proj.			
2.30	31037	Joint Res. Proj.	6.1	31043	JAERI
2.31	31038	Joint Res. Proj.	6.2	31044	JAERI
2.32	31039	Joint Res. Proj.	6.3	31045	JAERI
2.33	31040	Joint Res. Proj.	6.4	off line	JAERI
2.34	31041	Joint Res. Proj.			
2.35	31042	Joint Res. Proj.	7.1	31051	JAERI
2.36	31057	JAERI	7.2	32038	Coop.Res.Univ.

Section of this Report	Research Program Number	Type of Research Collaborations*
7.3	32039	JAERI
7.4	32040	JAERI
7.5	32041	Joint Res. Proj.
7.6	32042	Joint Res. Proj.
7.7	32043	Joint Res. Proj.
7.8	32044	Joint Res. Proj.
7.9	32045	Joint Res. Proj.
7.10	32046	Joint Res. Proj.
7.11	32047	Joint Res. Proj.
7.12	32048	Joint Res. Proj.
7.13	32049	Coop.Res.Univ.
8.1	31053	Joint Res. Proj.
8.2	31054	Joint Res. Proj.
8.3	31055	Joint Res. Proj.
9.1	31052	JAERI
9.2	32050	Joint Res. Proj.
9.3	32051	Joint Res. Proj.
9.4	32036	JAERI
9.5	Machine Study	JAERI
9.6	Machine Study	JAERI
9.7	Machine Study	JAERI
9.8	Machine Study	JAERI
9.9	Machine Study	JAERI
9.10	Machine Study	JAERI
9.11	Machine Study	JAERI
9.12	Machine Study	JAERI
9.13	Machine Study	JAERI

*Joint Res.: Joint research with private company or governmental institution

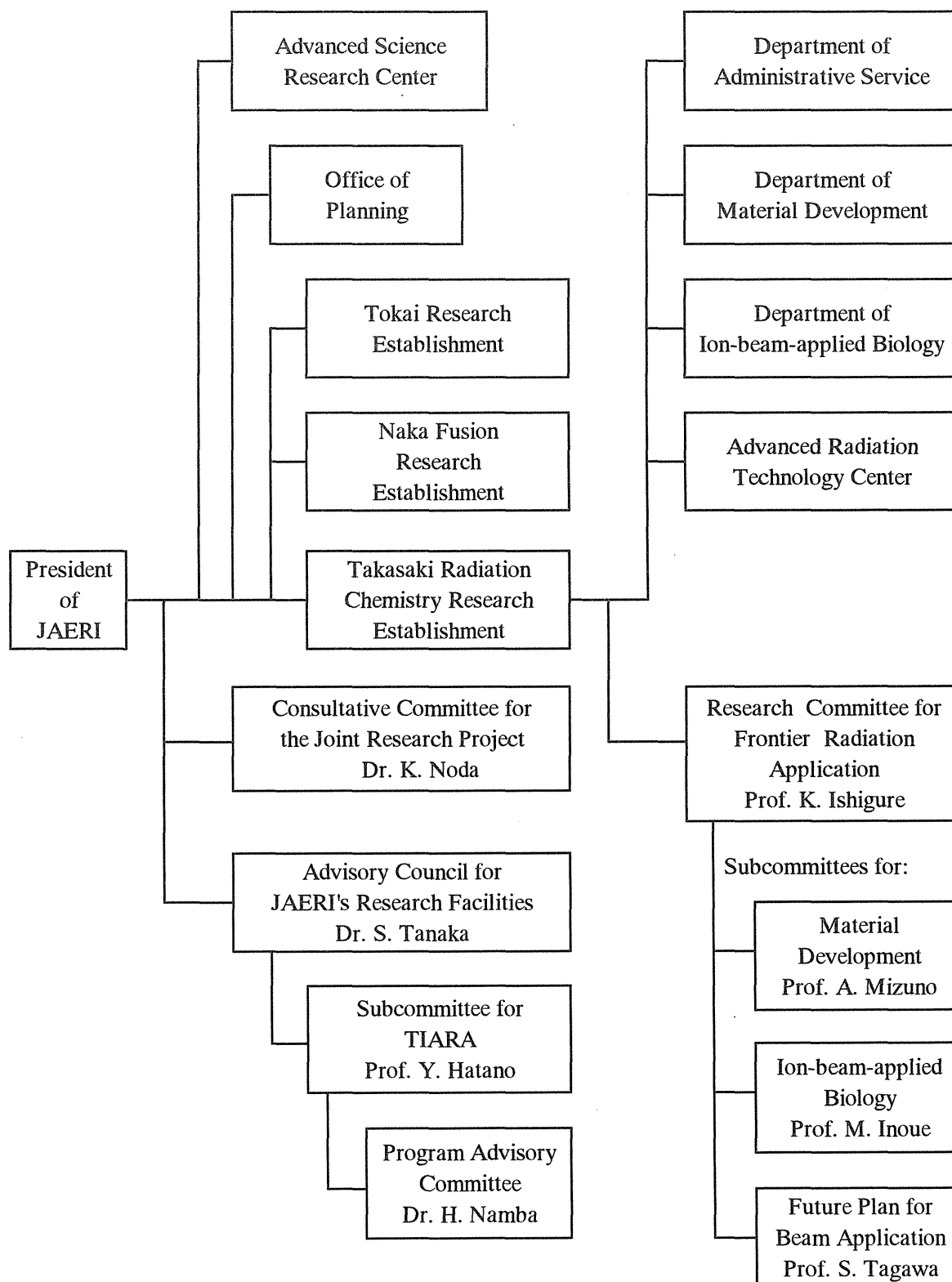
Coop. Res. Univ.: Cooperative research with a university or universities

Joint Res. Proj. : The Joint Research Project #

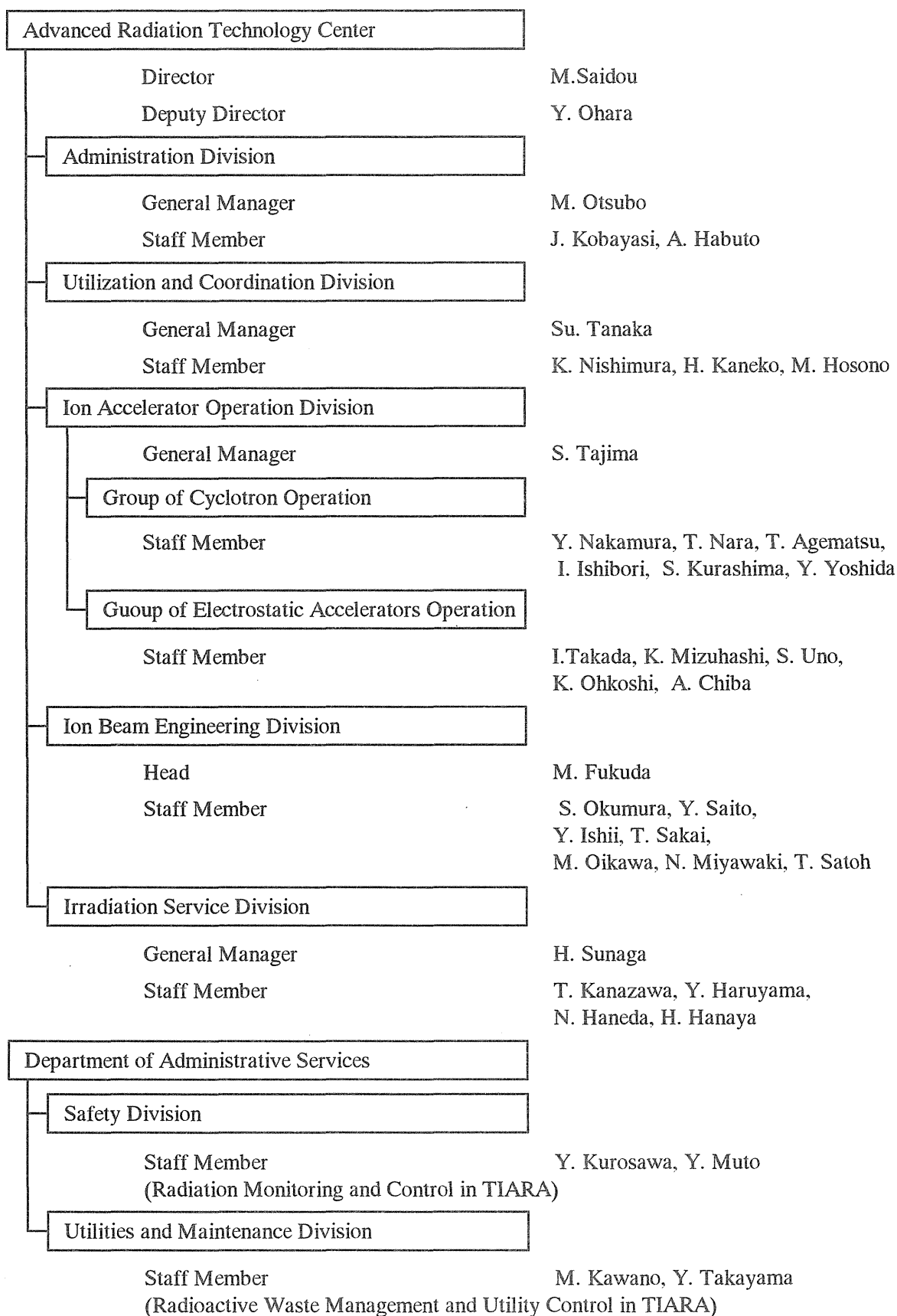
#For administration of these programs, we appreciate the cooperation of Research Center for Nuclear Science and Technology, The University of Tokyo.

Appendix 3. Organization and Personnel of TIARA (FY 2003)

1) Organization for the Research and Development of Advanced Radiation Technology



2) Personnel for the Administration, Operation and Control of TIARA



国際単位系 (SI) と換算表

表 1 SI基本単位および補助単位

量	名 称	記 号
長さ	メートル	m
質量	キログラム	kg
時間	秒	s
電流	アンペア	A
熱力学温度	ケルビン	K
物質質量	モール	mol
光度	カンデラ	cd
平面角	ラジアン	rad
立体角	ステラジアン	sr

表 3 固有の名称をもつSI組立単位

量	名 称	記号	他のSI単位 による表現
周波数	ヘルツ	Hz	s ⁻¹
力	ニュートン	N	m・kg/s ²
圧力, 応力	パスカル	Pa	N/m ²
エネルギー, 仕事, 熱量	ジュール	J	N・m
工率, 放射束	ワット	W	J/s
電気量, 電荷	クーロン	C	A・s
電位, 電圧, 起電力	ボルト	V	W/A
静電容量	ファラド	F	C/V
電気抵抗	オーム	Ω	V/A
コンダクタンス	ジーメンズ	S	A/V
磁束	ウェーバ	Wb	V・s
磁束密度	テスラ	T	Wb/m ²
インダクタンス	ヘンリー	H	Wb/A
セルシウス温度	セルシウス度	℃	
光量度	ルーメン	lm	cd・sr
照射度	ルクス	lx	lm/m ²
放射能	ベクレル	Bq	s ⁻¹
吸収線量	グレイ	Gy	J/kg
線量等量	シーベルト	Sv	J/kg

表 2 SIと併用される単位

名 称	記 号
分, 時, 日	min, h, d
度, 分, 秒	°, ', "
リットル	l, L
トン	t
電子ボルト	eV
原子質量単位	u

$$1 \text{ eV} = 1.60218 \times 10^{-19} \text{ J}$$

$$1 \text{ u} = 1.66054 \times 10^{-27} \text{ kg}$$

表 4 SIと共に暫定的に維持される単位

名 称	記 号
オングストローム	Å
バ ー ン	b
バ ー ル	bar
ガ ル	Gal
キ ュ リ ー	Ci
レ ン ト ゲ ン	R
ラ ド	rad
レ ム	rem

$$1 \text{ Å} = 0.1 \text{ nm} = 10^{-10} \text{ m}$$

$$1 \text{ b} = 100 \text{ fm}^2 = 10^{-28} \text{ m}^2$$

$$1 \text{ bar} = 0.1 \text{ MPa} = 10^5 \text{ Pa}$$

$$1 \text{ Gal} = 1 \text{ cm/s}^2 = 10^{-2} \text{ m/s}^2$$

$$1 \text{ Ci} = 3.7 \times 10^{10} \text{ Bq}$$

$$1 \text{ R} = 2.58 \times 10^{-4} \text{ C/kg}$$

$$1 \text{ rad} = 1 \text{ cGy} = 10^{-2} \text{ Gy}$$

$$1 \text{ rem} = 1 \text{ cSv} = 10^{-2} \text{ Sv}$$

表 5 SI接頭語

倍数	接頭語	記 号
10 ¹⁸	エクサ	E
10 ¹⁵	ペタ	P
10 ¹²	テラ	T
10 ⁹	ギガ	G
10 ⁶	メガ	M
10 ³	キロ	k
10 ²	ヘクト	h
10 ¹	デカ	da
10 ⁻¹	デシ	d
10 ⁻²	センチ	c
10 ⁻³	ミリ	m
10 ⁻⁶	マイクロ	μ
10 ⁻⁹	ナノ	n
10 ⁻¹²	ピコ	p
10 ⁻¹⁵	フェムト	f
10 ⁻¹⁸	アト	a

(注)

- 表 1～5 は「国際単位系」第 5 版, 国際度量衡局 1985 年刊行による。ただし, 1 eV および 1 u の値は CODATA の 1986 年推奨値によった。
- 表 4 には海里, ノット, アール, ヘクトールも含まれているが日常の単位なのでここでは省略した。
- bar は, JIS では流体の圧力を表わす場合に限り表 2 のカテゴリーに分類されている。
- EC 閣僚理事会指令では bar, barn および「血圧の単位」mmHg を表 2 のカテゴリーに入れている。

換 算 表

力	N (=10 ⁵ dyn)	kgf	lbf
	1	0.101972	0.224809
	9.80665	1	2.20462
	4.44822	0.453592	1

粘 度 1 Pa・s (N・s/m²) = 10 P (ポアズ) (g/(cm・s))

動粘度 1 m²/s = 10⁴ St (ストークス) (cm²/s)

圧	MPa (=10 bar)	kgf/cm ²	atm	mmHg (Torr)	lbf/in ² (psi)
	1	10.1972	9.86923	7.50062 × 10 ³	145.038
力	0.0980665	1	0.967841	735.559	14.2233
	0.101325	1.03323	1	760	14.6959
	1.33322 × 10 ⁻⁴	1.35951 × 10 ⁻³	1.31579 × 10 ⁻³	1	1.93368 × 10 ⁻²
	6.89476 × 10 ⁻³	7.03070 × 10 ⁻²	6.80460 × 10 ⁻²	51.7149	1

エネルギー・仕事・熱量	J (=10 ⁷ erg)	kgf・m	kW・h	cal (計量法)	Btu	ft・lbf	eV
	1	0.101972	2.77778 × 10 ⁻⁷	0.238889	9.47813 × 10 ⁻⁴	0.737562	6.24150 × 10 ¹⁸
	9.80665	1	2.72407 × 10 ⁻⁶	2.34270	9.29487 × 10 ⁻³	7.23301	6.12082 × 10 ¹⁹
	3.6 × 10 ⁶	3.67098 × 10 ⁵	1	8.59999 × 10 ⁵	3412.13	2.65522 × 10 ⁶	2.24694 × 10 ²⁵
	4.18605	0.426858	1.16279 × 10 ⁻⁶	1	3.96759 × 10 ⁻³	3.08747	2.61272 × 10 ¹⁹
	1055.06	107.586	2.93072 × 10 ⁻⁴	252.042	1	778.172	6.58515 × 10 ²¹
	1.35582	0.138255	3.76616 × 10 ⁻⁷	0.323890	1.28506 × 10 ⁻³	1	8.46233 × 10 ¹⁸
	1.60218 × 10 ⁻¹⁹	1.63377 × 10 ⁻²⁰	4.45050 × 10 ⁻²⁶	3.82743 × 10 ⁻²⁰	1.51857 × 10 ⁻²²	1.18171 × 10 ⁻¹⁹	1

$$1 \text{ cal} = 4.18605 \text{ J (計量法)}$$

$$= 4.184 \text{ J (熱化学)}$$

$$= 4.1855 \text{ J (15℃)}$$

$$= 4.1868 \text{ J (国際蒸気表)}$$

$$\text{仕事率 } 1 \text{ PS (仏馬力)}$$

$$= 75 \text{ kgf} \cdot \text{m/s}$$

$$= 735.499 \text{ W}$$

放射能	Bq	Ci
	1	2.70270 × 10 ⁻¹¹
	3.7 × 10 ¹⁰	1

吸収線量	Gy	rad
	1	100
	0.01	1

照射線量	C/kg	R
	1	3876
	2.58 × 10 ⁻⁴	1

線量当量	Sv	rem
	1	100
	0.01	1

(86年12月26日現在)

TIARA Annual Report 2003



古紙配合率100%
白色度70%再生紙を使用しています